Understanding the criticality of volumetric defects on the fatigue behavior of additively manufactured aluminum alloys

by

Shaharyar Baig

A dissertation submitted to the Graduate Faculty of
Auburn University
in partial fulfillment of the
requirements for the Degree of
Doctor of Philosophy

Auburn, Alabama
August 9, 2025

Keywords: Additive manufacturing; Aluminum alloys; Defect sensitivity; Failure analysis; Fatigue; Probability of detection

Approved by

Nima Shamsaei, Chair, Philpott-WestPoint Stevens Distinguished Professor, Department of Mechanical Engineering
Shuai Shao, Co-Chair, McWane Associate Professor, Department of Mechanical Engineering
Hareesh Tippur, McWane Chair Professor, Department of Mechanical Engineering
Jia Liu, Associate Professor, Department of Industrial and Systems Engineering
Nikolas Hrabe, National Institute of Standards and Technology
Aleksandr Vinel, Associate Professor, Department of Industrial and Systems Engineering

Abstract

This study investigates the criticality of volumetric defects on the fatigue behavior of additively manufactured (AM) Al alloys. The role of various microstructures in determining sensitivity to defects, in particular their effect on the fatigue crack initiation and growth, is examined. Furthermore, the effectiveness of both destructive and non-destructive evaluation methods in characterizing the critical defect features for fatigue life prediction is assessed. The uniaxial fatigue behavior of two Al alloys, AlSi10Mg and Scalmalloy, each possessing distinct microstructures and thus likely to exhibit varying defect sensitivities, is investigated. It is shown that while applying post-process thermal treatments can enhance the tensile properties of AlSi10Mg by altering the microstructures, the fatigue properties are still largely governed by the presence of volumetric defects. In contrast, Scalmalloy, which possesses a bimodal grain structure, exhibits similar sensitivity to crack-initiating defects. However, microstructural effects become more apparent in the near-threshold regime. Specifically, the location of defects within the microstructure influences fatigue behavior in Scalmalloy, and microstructural features become increasingly influential approaching the crack growth threshold. Nevertheless, it is found that by considering both the short and long crack growth rates, the fatigue behavior can be sufficiently described within scatter bands of ±3 for both alloys. Moreover, non-destructive part qualification methods are explored and the efficacy of x-ray computed tomography (XCT) examination in capturing critical defect features is quantified. The results show that the probability of detection (POD) of defects is a function of the XCT scan parameters, coupon geometry and AM defect types. At a given scan resolution and defect size, lack-of-fusions (LoFs) exhibit a lower POD compared to spherical defects such as keyholes (KHs) and gas-entrapped pores (GEPs). While LoFs are more difficult to capture in lower resolutions, even when detected, the errors in their size measurements are greater compared to spherical defects which can be reliably detected with good accuracy in their sizing. A distance-criterion based correction is proposed, which allows critical information for LoFs to be recovered in low-resolution scans by reconstructing the defect geometry. It is demonstrated that the procedure can significantly reduce the sizing errors, allowing for rapid and accurate defect characterization. To assess the effectiveness of the distance-criterion approach for fatigue life predictions, AlSi10Mg and Scalmalloy fatigue specimens are examined by XCT prior to testing and the representations of the critical defects are identified in the XCT scans. The XCT data is post-processed by applying the distance-criterion based correction and incorporated into crack-growth based fatigue models. While the uncorrected data provides mostly non-conservative predictions due to the underestimation of defect sizes, the corrected data input into the fatigue models can provide accurate, moderately conservative fatigue life predictions within scatter bands of ±3.

Acknowledgements

I would like to express my gratitude to my advisor, Dr. Nima Shamsaei, for his unwavering support, invaluable guidance, and exceptional mentorship throughout my PhD studies. This dissertation would not have been possible without his leadership, insight, and vision. I am also grateful to Dr. Shuai Shao for serving on my committee and for his thoughtful input and timely feedback, which greatly strengthened the quality of my work. My sincere thanks go to Dr. Hareesh Tippur, Dr. Jia Liu, and Dr. Nikolas Hrabe for their service on my committee and to Dr. Aleksandr Vinel for serving as the University Reader. I truly appreciate their time, support, and constructive suggestions. Finally, I would like to thank all my friends and colleagues at the National Center for Additive Manufacturing Excellence (NCAME), who have helped me in my personal and professional development and made my graduate school journey memorable. I would like to dedicate this dissertation to my mother, Asma, and my father, Zahid.

Table of Contents

List of Tables

List of Figures

Abbreviations

AM	Additive manufacturing/Additively manufactured
ANOVA	Analysis of variance
BD	Build direction
BSE	Backscattered electron
BV	Baseline vertical
CG	Coarse grain/grained
EBSD	Electron backscatter diffraction
EDS	Electron x-ray energy dispersive spectroscopy
EVS	Extreme value statistics
FG	Fine grain/grained
GEP	Gas-entrapped pore
HCF	High cycle fatigue
HT	Heat treatment/heat treated
IPF	Inverse pole figure
KH	Keyhole
LCF	Low cycle fatigue
LoF	Lack-of-fusion
L-PBF	Laser powder bed fusion/fused
MCF	Mid cycle fatigue
NDE	Non-destructive examination/evaluation
NHT	Non-heat treated
OV	Overheated vertical
POD	Probability of detection
RO	Ramberg-Osgood equation
SEM	Scanning electron microscope/microscopy
SR	Stress relief/stress relieved
UD	Underheated diagonal
UH	Underheated horizontal
XCT	X-ray computed tomography

Nomenclature

R_a	Arithmetic average roughness
n'	Cyclic strain hardening exponent
K'	Cyclic strength coefficient
σ_{w0}	Defect-free fatigue strength
$\sqrt{area_0}$	El-Haddad parameter
S	Engineering stress
$\frac{\Delta\varepsilon_e}{2}$	Elastic strain amplitude
e	Engineering strain
C	Fatigue ductility exponent
σ_{w0}	Fatigue limit
σ_f'	Fatigue strength coefficient
b	Fatigue strength exponent
σ_{max}	Maximum stress
E	Modulus of elasticity
Y	Murakami location factor
%El	Percent elongation to failure
$\frac{\Delta\varepsilon_p}{2}$	Plastic strain amplitude
$2N_f$	Reversals to failure
ε_a	Strain amplitude
R_ε	Strain ratio
σ_a	Stress amplitude
R_σ	Stress ratio
$\sqrt{area}$	Square root of projected defect area
ΔK_{th}	Threshold stress intensity factor range
ε_a	Total strain amplitude
ε_f	True fracture strain
S_u	Ultimate tensile strength
S_y	Yield strength

1. Introduction

Additive manufacturing (AM) has revolutionized the production of structural parts in industries including aerospace, medical and automotive. Using a computer aided design (CAD) model, AM enables the fabrication of intricate, customized parts and can produce geometries which were previously unattainable through conventional manufacturing processes [1,2]. Over the years, various AM processes have been developed which can be broadly classed based on the feedstock and the energy sources used. Among them, laser powder bed fusion (L-PBF) is perhaps the most popular AM technology for processing metals due to its ability to produce highly complex parts with good dimensional accuracy [3]. In L-PBF, a layer of powder is spread across a build plate and selectively melted by a laser source. After each laser pass, the build platform is lowered, and the subsequent layer is spread and fused on top of the previous. This layer-by-layer process of fabricating from the bottom up is repeated until the desired part is obtained.

Although L-PBF processes can fabricate functional components at high resolutions, the unique thermal history associated with each part can strongly influence the resultant micro-/defect structure. For example, the high cooling rates experienced during solidification in L-PBF can lead to finer microstructures than their wrought counterparts. Such microstructures can provide superior tensile strength due to grain refinement strengthening [4]. However, the repetitive melting-solidification with each layer can promote the formation of process-induced volumetric defects. These defects are stress concentrators under cyclic loading, and detrimental to the fatigue properties of AM parts [5]. In addition, any slight or large variations in the feedstock, process conditions or design parameters can impact the thermal history and the resultant micro-/defect-structure. This can introduce uncertainties in the part performance, even for identical parts in the same build. For instance, any intentional or unintentional deviations in the common process parameters including laser power, scan speed, hatch distance and layer thickness can cause insufficient/excess energy input into the melt pool. This, in turn, can lead to the formation of various types of defects including lack-of-fusions (LoFs), gas-entrapped pores (GEPs) and keyholes (KHs) [6].

LoFs, GEPs and KHs exhibit distinct morphological features where stress concentrations may develop, and fatigue damage occurs under cyclic loading. The sensitivity of a material's fatigue behavior to the presence of these defects is dependent on the microstructural features. Certain fine-grained materials including AlSi10Mg, Ti-6Al-4V and 17-4 PH SS exhibit higher defect-sensitivity compared to others such as the Ni-based alloys, which consist of coarser microstructures. This can be attributed to the defect population within the part and their interactions with the surrounding microstructures. On one hand, when a small defect is located inside a coarse grain, microstructural barriers including grain boundaries, and precipitates can assist in arresting crack propagation and the fracture mechanisms are strongly influenced by the microstructural features. On the other hand, when the defect size exceeds the microstructural length (such as the grain size), the defect features can be more influential in governing the fatigue behavior as compared to the microstructural features [7,8].

Defect sensitive materials encompass fine-grained aluminums (Al), which possess good strength-to-weight ratio, among other desirable properties including ease of machinability and excellent corrosion resistance. These attributes make them prime candidates for use in industries including automotive, biomedical and aerospace [9]. While Al alloys have traditionally been produced using conventional processes such as casting, rolling, forging and extrusion, adopting AM for large-scale production can provide greater design flexibility. Among the various AM alloys, AlSi10Mg is perhaps one of the most popular materials due to its low coefficient of thermal expansion which allows for complex geometries to be fabricated. Furthermore, certain high performance Al alloys such as Scalmalloy have specifically been designed for the AM process and provide exceptional tensile strengths compared to traditional Al alloys [10]. However, the widespread adoption of AM technologies for fabricating Al components in critical applications has been hindered by the uncertainty in their behavior, particularly due to their high sensitivity to manufacturing defects which can severely degrade the fatigue resistance.

The characteristics of volumetric defects including their size, shape and location can determine the fatigue criticality. For example, Nezhadfar et al. investigated the microstructure, porosity, and fatigue behavior of five different L-PBF Al alloys. In all five Al alloys, regardless of the differences in microstructures, crack initiation consistently occurred at process-induced defects when such defects were located near the surface [11]. In another study, the effects of process parameters and part orientation of AlSi10Mg parts were investigated by Ferro et al., who concluded that the part orientation had a minimal influence on the fatigue strengths [12]. Instead, the fatigue strength was found to be highly sensitive to defect types and morphology, with LoFs being the fatigue crack initiators in most cases. Such strong correlations between defects and fatigue behavior for Al alloys necessitates the need for more comprehensive studies examining the criticality of various defect features and exploring their applications in defect-sensitive fatigue models for part qualification.

The micro-/defect structure of AM parts can be characterized through destructive and non-destructive means. The information obtained from such analyses allow for defect-fatigue correlations to be established to provide insights into the structure-property relationships. Current methods include destructive testing of witness coupons to examine the micro-/defect structure and correlating that information to the part performance. While these schemes are effective in establishing design allowables for production components, the stochastic nature of defect formation for AM processes often limits their applicability to a particular process/part with well-defined process controls [13]. Non-destructive examination (NDE) based methods, on the other hand, present a potentially less expensive, time-efficient and versatile alternative as they can be used to examine and rapidly qualify AM components on a part-by-part basis [14,15]. NDE techniques such as x-ray computed tomography (XCT) can unveil the internal defect-structure in 3D for thorough examinations of the defect content within entire components. However, the quality of XCT scans can be significantly dictated by not only the system parameters, but also the material, and the defect characteristics. Thus, the efficacy of XCT-based examinations in characterizing the volumetric defect content and subsequently the fatigue lives of AM parts needs to be understood.

This dissertation aims to advance the understanding of critical defect features influencing the fatigue behavior of defect-sensitive AM Al alloys. Two Al alloys with distinct microstructures—and thus differing sensitivities to defects—will be fabricated, characterized and tested to investigate how microstructure-defect interactions influence their fatigue behavior. Furthermore, the critical defect features will be analyzed via destructive and non-destructive examination and the effectiveness of these techniques for fatigue life predictions of AM parts will be determined.

1.1. Project Goal and Objectives

The overall goal of this research is to understand the criticality of volumetric defects on the fatigue behavior of additively manufactured Al alloys. To achieve this, several objectives have been established. The **first objective (Chapters 2 and 3)** is to identify the critical defect features that influence the fatigue behavior of various AM Al alloys with differing microstructures and sensitivities to defects. As part of this objective, it is hypothesized that the fatigue behavior becomes more sensitive to the presence of defects as the ultimate tensile strength increases (Hypothesis 1a). In addition, finer grains exhibit greater defect sensitivity to defects than coarser grains in Al alloys (Hypothesis 1b). The **second objective (Chapter 4)** is to assess the impact of XCT acquisition parameters on the probability of detection of AM defects. Under this objective, it is hypothesized that the probability of detection is higher for spherical defects of a given size than for irregular shaped defects (Hypothesis 2a). Furthermore, the accuracy in measuring defect features remains consistent across different part sizes when the same voxel size is used (Hypothesis 2b). The **third objective (Chapter 5)** is to evaluate the effectiveness of non-destructive examination in assessing the fatigue lives of AM Al alloys. It is hypothesized that the fatigue criticality of defects cannot be adequately defined for low resolution XCT data due to significant feature errors (Hypothesis 3a). Moreover, fatigue life predictions based on XCT data are non-conservative since fatigue critical defect features are misrepresented (Hypothesis 3b).

1.2. Outline of Dissertation

This dissertation aims to fill in knowledge gaps in the current understanding of the criticality of volumetric defects on the fatigue behavior of additively manufactured Al alloys. While the defect-fatigue properties of Al alloys processed through conventional techniques, such as casting and forging, have been extensively documented [16–18], AM processed Al alloys present additional complexity in predicting the part performance. One of the major challenges in AM is the stochastic nature of process-induced defect formation, which exhibit varying fatigue criticalities depending on the defect features and their distributions. In addition, the sensitivity of various microstructures to defects is not well understood, especially considering the unique thermal histories observed by AM materials. This includes the fine-grained microstructures resulting from the ultra-high cooling rates of the AM process and bimodal microstructures consisting of fine- and coarse-grained regions [4]. Moreover, NDE-based structural integrity assessments have gained widespread attention due to their potential to enable rapid qualification of parts and fully leverage the on-demand production opportunities presented by AM. However, the limitations in the information provided by these techniques and thus, their efficacy in structural integrity-based assessments of AM materials has not been studied in detail.

To address these gaps, the dissertation is organized in the following manner: Chapter 2 investigates the effect of heat treatment on the tensile and fatigue behavior of L-PBF AlSi10Mg. A range of thermal treatments including solutionizing at three temperatures followed by aging are applied to modify the microstructure. Tensile and strain-controlled fatigue tests are conducted to evaluate mechanical performance. The influence of heat treatment on microstructural evolution, defect sensitivity, and resulting fatigue behavior in various regimes is examined to establish structure-property relationships.

In Chapter 3, the fatigue behaviors of L-PBF AlSi10Mg and Scalmalloy, two Al alloys with distinct microstructures, are investigated. The sensitivity of the microstructures to the presence of defects is systematically studied by varying defect types and populations. Common AM defects including LoFs, GEPs and KHs are intentionally induced in different sets of specimens. The critical defect information is extracted from the fracture surfaces and incorporated into damage-tolerant fatigue models. The insights from the fatigue crack initiation and growth behavior are used to establish fatigue-defect correlations.

Chapter 4 assesses the impact of XCT scan parameters on the probability of detection and feature errors with differentiating defects' geometry. The purpose of this chapter is to examine the effectiveness of NDE-based examinations in detecting fatigue critical defects and accurately determining their features. In addition, this chapter explores the correction of low-resolution XCT scans— often used in industrial applications where large format, rapid scans are required—to improve the sizing accuracy of AM defects.

Chapter 5 leverages the fatigue data generated in Chapter 3 and the methods developed in Chapter 4 to evaluate the effectiveness of XCT-based examinations in assessing the fatigue lives of L-PBF Al alloys. Fatigue specimens are examined via XCT to reveal their defect types and populations. The critical defect information from fractography is correlated to their XCT representations to understand the influence of resolution constraints. The methods developed in Chapter 4 are used to correct XCT data in limited resolutions and integrated into crack-growth based models. The fatigue life estimates are compared before and after applying the corrections to highlight the potential of such methods in non-destructive structural integrity-based assessments of AM Al alloys.

Chapter 6 summarizes the objectives and hypotheses defined previously and how the results from the various studies pertain to the specific tasks under each hypothesis. Moreover, the future direction of this research is discussed, and the significance of potential developments are suggested.

1.3. Broader Impact

The results of this dissertation can help accelerate the adoption of AM technologies in various industries by establishing defect-fatigue relationships for Al alloys. The criticality of differing defect features across microstructures with varying defect sensitivities will be investigated, providing guidance to AM users for process optimization, material selection and design based on the end-use applications. In addition, the findings of this dissertation can help improve the current standards in non-destructive and destructive testing of AM materials. Specifically, this work will provide knowledge regarding defect characterization across various

XCT scan resolutions and propose a framework to recover critical defect information from limited-resolution such as the large format scans used in industrial applications. The knowledge generated can be leveraged by AM and NDE communities to establish best practices and guidelines for non-destructive qualification of AM parts in fatigue critical applications. Moreover, the NDE practices outlined in this study will help in reducing costs and efficiency by reducing the need for costly destructive testing campaigns. Lastly, this dissertation will generate materials data, including microstructural, tensile and fatigue properties for AlSi10Mg and Scalmalloy which will be publicly available for use.

2. Tensile and Fatigue Behaviors of Additively Manufactured AlSi10Mg: Effect of Solutionizing and Aging Heat Treatments [19]

2.1. Introduction

Aluminum alloys are commonly used in various industries because of their superior strength/stiffness to weight ratio compared to other alloys [20,21]. Among various Al alloys, AlSi10Mg as a cast alloy [21], has historically been used to fabricate complex/thin-walled geometries. Recently, processing AlSi10Mg through additive manufacturing (AM) has shown to be very promising as intricate, lightweight parts can be manufactured without the need for complex fixtures and tooling. Among the numerous AM techniques, laser beam powder bed fusion (L-PBF) is perhaps the most popular as it can fabricate complex shapes by selectively melting and consolidating powder particles using a high power density laser in a layer-by-layer fashion without the need for much support structures [22].

L-PBF components are often characterized by their unique microstructure and the inherent AM process induced defects, which in turn differentiate their mechanical performance from their conventionally processed counterparts [5,23,24]. Due to the unique micro-/defect-structures of AlSi10Mg processed by L-PBF, typical heat treatments (HT) used for wrought counterparts may not always be effective. For instance, the high cooling rates of the L-PBF process induces cellular networks of Si-rich inter-dendritic regions [25,26] which can give rise to improved tensile properties compared to the artificially aged condition [27–29].

Despite some improvements in tensile properties, the as-solidified fine dendritic microstructure may make the material more sensitive to surface notches and volumetric defects under cyclic loading [11,30]. As such, the fatigue performance of this material is not only often negatively impacted by the AM induced defects, including gas-entrapped pores and lack-of-fusion defects [31,32], but it may also be inferior in the non-heat treated (NHT) and stress relieved (SR) condition compared to the aged condition [25,32–35] . However, discrepancies still exist in literature regarding the beneficial effect of standardized heat treatments, such as T6, on additively manufactured (AM) AlSi10Mg parts. For instance, Zhang et al. [36] performed stress relief (300°C for 2h), solution treatment (530°C for 1h), and artificial aging (170°C for 12h) on L-PBF specimens and concluded that all heat treatments, including T6, diminish fatigue properties when compared with the non-heat treated condition. Notwithstanding the disagreement, further studies comparing the effect of multiple heat treatments, which can result in significant variation in the microstructure, and their effect on the fatigue behavior of AM AlSi10Mg are still needed.

This study further investigates the effects of the microstructure and defects on the tensile and fatigue properties of L-PBF AlSi10Mg. The influence of various heat treatments on the microstructure of the alloy, in conjunction with its tensile properties, are first investigated in detail. The effects of the solution treatment (T4) at three different temperatures of 425, 475 and 525 °C as well as artificial aging (T7) at 165 °C are examined. The knowledge gained together with the information of fatigue critical defects obtained from fracture surfaces are then used to explain the strain-life fatigue behavior.

The study is organized in the following order: Section 2 lists the experimental material and methodologies along with the design of experiments (DoE). Section 3 presents the experimental results including microstructural analysis and the mechanical properties (i.e., tensile and fatigue). Section 4 discusses the resulting tensile and fatigue behavior and Section 5 summarizes the experimental observations and corresponding discussions as conclusions.

2.2. Material and Experiments

2.2.1. Material and Specimens Fabrication

Argon-atomized AlSi10Mg powder supplied by Carpenter Additive was used as the feedstock material [37]. The nominal chemical composition of the powder, as specified by Carpenter Additive was ≥89.50%Al, 9.60%Si, 0.38%Mg and 0.18%Fe in wt.%. Specimens were fabricated on an EOS M290 L-PBF system using manufacturer recommended process parameters as shown in Table 1. The build chamber was kept inert using argon gas throughout fabrication. In addition, extra specimens were also fabricated on a Renishaw AM250 system using the parameters shown in Table 1. After removal from the build plates, each specimen was assigned with a label with the prefix relating to the L-PBF system it was fabricated on (i.e., E=EOS M290, R=Renishaw AM250), followed by the specimen number.

Table 1. L-PBF process parameters used to fabricate AlSi10Mg specimens.

System	Laser power (W)	Scanning speed (mm/s)	Hatch spacing (mm)	Layer thickness (mm)	Rotation angle (°)
EOS M290	370	1300	0.13	0.030	67
Renishaw AM250	200	533	0.13	0.025	67

The build layouts consisted of round bars (10 mm diameter and 90 mm height) that were machined into fatigue specimens, and net shaped tensile specimens with a cylindrical gage section (4 mm diameter and 20 mm length). The build arrangement schematics for EOS M290 and Renishaw AM250 are presented in **Figure 1** (A) and (B), respectively. For reference, the z-direction aligns with the build direction. The final geometry of the tensile test specimens can be seen in **Figure 1** (C), which was based on guidelines following ASTM E8 [38], along with the fatigue specimen geometry in **Figure 1** (D), which was based on guidelines following ASTM E606 [39] and adopted for both EOS and Renishaw specimens.

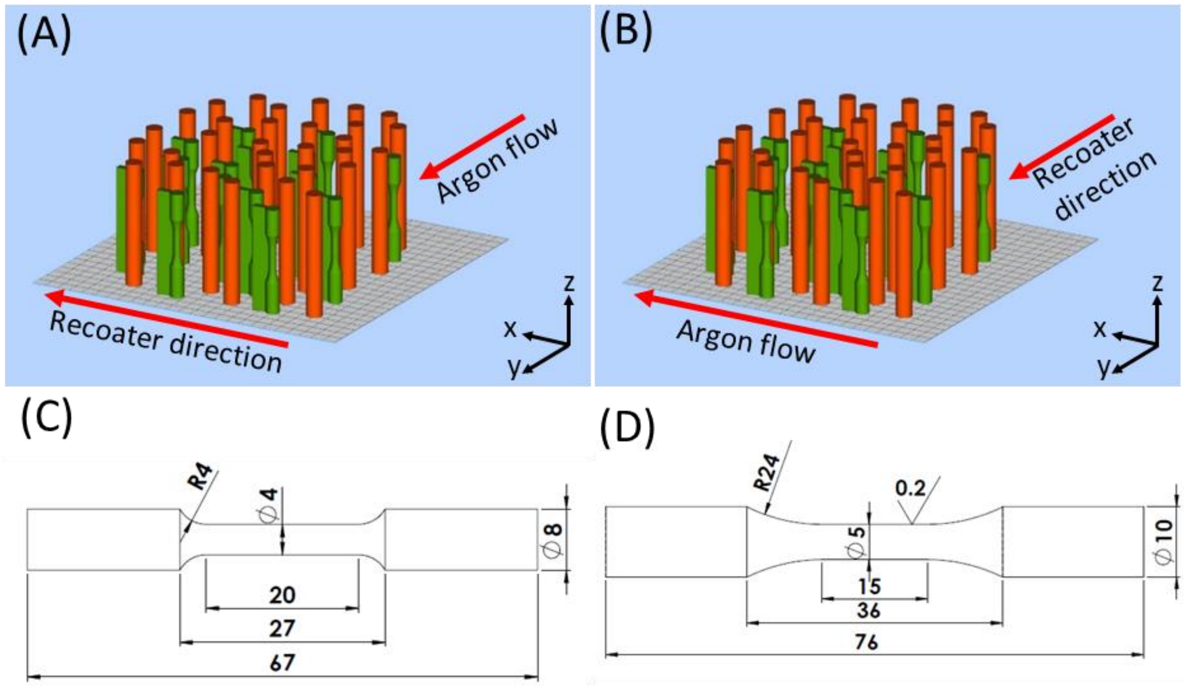

Figure 1. Schematics showing the build layouts for (A) EOS M290, (B) Renishaw AM250, (C) geometry of the net shape tensile specimens, and (D) the final geometry of the fatigue specimens after machining (all dimensions in mm). Note that the cylindrical bars which were later machined into fatigue specimens are shown in red and the net-shape tensile specimens are shown in green in (A) and (B).

2.2.2. Heat Treatment Procedures

All specimens were heat treated (HT) in a Thermo Fisher Scientific electric furnace. The furnace temperature was measured using an external thermocouple attached to the specimens during heat treatment and maintained within ±5 °C from the set temperature of the furnace. The heat treatments consisted of three main stages; first, a solution treatment step was performed for 24 hours at three different temperatures of 425, 475, and 525 °C, followed by water quenching. Then, some of the specimens were allowed to naturally age (NA) at room temperature for at least 96 hours prior to mechanical testing for the T4 condition. The rest of the solutionized specimens were artificially aged, i.e., T7 for 16 hours at 165 °C. The aging times were selected based on a preliminary microstructural/hardness evolution study which determined the peak aged (T6) and over aged (T7) conditions of the material [40]. For comparison, the properties obtained in this study are presented alongside the ones from reference [30] in the experimental results section. The heat treatment in reference [30] consisted of stress relieving at 300ºC for 2 hours and allowing the specimens to naturally age before mechanical testing. Each of the heat treatments were given the following designation: XX-YYY-ZZZ, where XX refers to the heat treatment schedule, i.e., SR, T4, or T7; YYY refers to the stress relief/solutionizing temperature, i.e., 300, 425, 475 or 525°C; ZZZ refers to the aging temperature, i.e., 165°C for artificially aged specimens in the T7 conditions and NA for specimens naturally aged at room temperature in the SR and T4 conditions. For example, the specimens which were solutionized at 425°C and allowed to naturally age in the T4 schedule were given the designation: T4-425-NA. Similarly, specimens which were solutionized at 475°C, followed by aging at 165°C for 16 hours in the T7 schedule were given the designation: T7-475-165. The full list of heat treatment procedures is provided in **Table S1** of the supplementary materials.

2.2.3. Microstructure and Metallography

Microstructural characterization was conducted for all EOS L-PBF AlSi10Mg specimens in the non-heat treated and the heat treated conditions as explained in the "Heat Treatment Procedures" section**,** on the horizontal (x-y) plane, perpendicular to the build direction. The samples were obtained from the gage section of the test specimens and were mounted using epoxy resin, and ground and polished according to ASTM-E3 [41]. For grinding, various grit sizes (from 400 to 1200) of silicon carbide (SiC) papers were used. Lastly, a final polishing step was performed using colloidal silica suspension with a particle size of 0.02 μm.

Microscopy was performed using a Zeiss Crossbeam 550 Scanning Electron Microscope (SEM) equipped with X-ray energy dispersive spectroscopy (EDS) and electron backscatter diffraction (EBSD) detectors. The backscattered secondary electron (BSE) images were obtained using Electron Channeling Contrast Imaging technique [42]. Furthermore, optical microscopy was performed on the cross sectional (x-z) planes (parallel to the build direction) of the tensile fracture surfaces using a Keyence VHX-6000 digital optical microscope.

2.2.4. Mechanical Testing

Tensile specimens, which were fabricated on EOS, were tested in the as-built surface condition using an MTS landmark servo-hydraulic load frame with a load cell capacity of 100 kN. Tensile testing was conducted according to ASTM-E8/E8M-16a [38] with a crosshead displacement rate of 0.013 mm/s (approximate strain rate of 0.0009 mm/mm/s). An extensometer was used to measure strains during the initial stage of each tensile test for calculating the modulus of elasticity and the yield strength. Limited by the travel distance of the extensometer, only the first 0.035 mm/mm strain was measured. It should be noted that tensile properties were generated for the non-heat treated condition and all of the T4/T7 heat treated conditions. For each condition, at least 3 tests were performed to ensure repeatability. The average values along with the standard deviations obtained from these tests are reported in the results section.

Uniaxial, fully-reversed ($R_\varepsilon = \frac{\varepsilon_{min}}{\varepsilon_{max}} = -1$), strain-controlled fatigue testing was performed on the machined EOS fatigue specimens per ASTM E606 [39]. Testing was carried out at room temperature at the strain amplitudes of 0.0015, 0.002, 0.003 and 0.005 mm/mm. Due to some of the EOS fracture surfaces being damaged under fully-reversed, R=-1 loading, additional uniaxial, force-control fatigue testing was carried out on the machined Renishaw specimens according to ASTM E466 [43] at a single stress-level, σ_{max} = 90 MPa and a stress ratio of R=0.1. The fracture surface information from the additional tests were used to correlate the crack initiating defect features with the fatigue lives. Tests were considered concluded upon final fracture, and for any which exceeded 10^7 reversals, the tests were stopped and considered as runouts. Fracture surfaces were examined by a scanning electron microscope to measure the size and determine the type of the crack initiating defects. The size of the defects was evaluated using Murakami's $\sqrt{area}$ parameter, which considers the square root of the defect area projected on to the plane perpendicular to the applied stress. In this approach, the area was considered as a smooth convex contour of the defect, which included the ligament between the defect and surface for near surface volumetric defects. It should be noted that only the following three heat treated conditions were tested for their fatigue properties: T4-425-NA, T7-475-165 and T4-525-NA. These three heat treatments were selected based on their tensile toughness, i.e., a larger area under their tensile curves, which is commonly believed to result in better fatigue performances [8].

2.3. Experimental Results

2.3.1. Microstructure

The BSE micrographs and inverse pole figure (IPF) maps are presented in Figure 2 for the non-heat treated as well as the solution treated EOS samples (examined using the T4 samples) on the x-y plane (i.e., perpendicular to the build direction). In the non-heat treated condition (Figure 2(A)), a dendritic microstructure was observed which resulted from the high cooling rate of the L-PBF process [44] and consisted of a fine network of Si-rich cellular regions between the dendrite arms [45,46]. This microstructure has been reported to increase the tensile strength at the cost of some reduction in ductility [47,48]. Subsequent solution treatments at elevated temperatures of 425, 475, and 525 °C (above the solvus temperature of Mg_2Si of ~400 °C [46]) for 24 hours, completely dissolved the dendritic regions [49,50] and formed two types of precipitates, namely, the Si-particles (bulky shape) and the Fe-bearing (β-AlFeSi) phases [46], see Figure 2 (C), (E), (G). One can observe that the size of these later formed precipitates seems to increase with the solution temperature.

Finally, upon subsequent artificial aging (T7) at 165 °C (below Mg_2Si solvus temperature) for 16 hours, fine Mg_2Si precipitates were believed to have formed, which could strengthen the material [49,51], although they were generally too small to be visible under SEM. In fact, Zhou et al. reported the formation of metastable precipitates of Mg_2Si in L-PBF AlSi10Mg with a size <10 nm after 10 hours of aging, which grew up to 150 nm after 24 hours of aging [49,51]. Our preliminary quantitative image analysis revealed that aging treatments had little effect on the size and morphology of prior Si-particles and β-AlFeSi phases formed during solution heat treatment.

The IPF plots in Figure 2 (B), (D), (F) and (H) show that various solution temperatures appear to result in similar grain sizes. The grain sizes were obtained from EBSD analysis using the Oxford *AZtec* software by calculating these based on ASTM E2627 [52]. The average grain sizes for NHT, T4-425-NA, T4-475-NA, and T4-525-NA samples were 1 μm, 1.9 μm, 4.8 μm, and 5.3 μm, respectively. It can also be seen that there are two distinct regions containing fine and coarse grains in the NHT condition (see Figure 2 (A)). The fine grained regions could be the melt pool boundaries where the initial solidification occurred at a higher rate [46,53–56]. As measured by the EBSD analysis, the subsequent aging step in T7 heat treatment at the lower temperature (165 °C) than that of the prior solution treatments had little effect on the grain size.

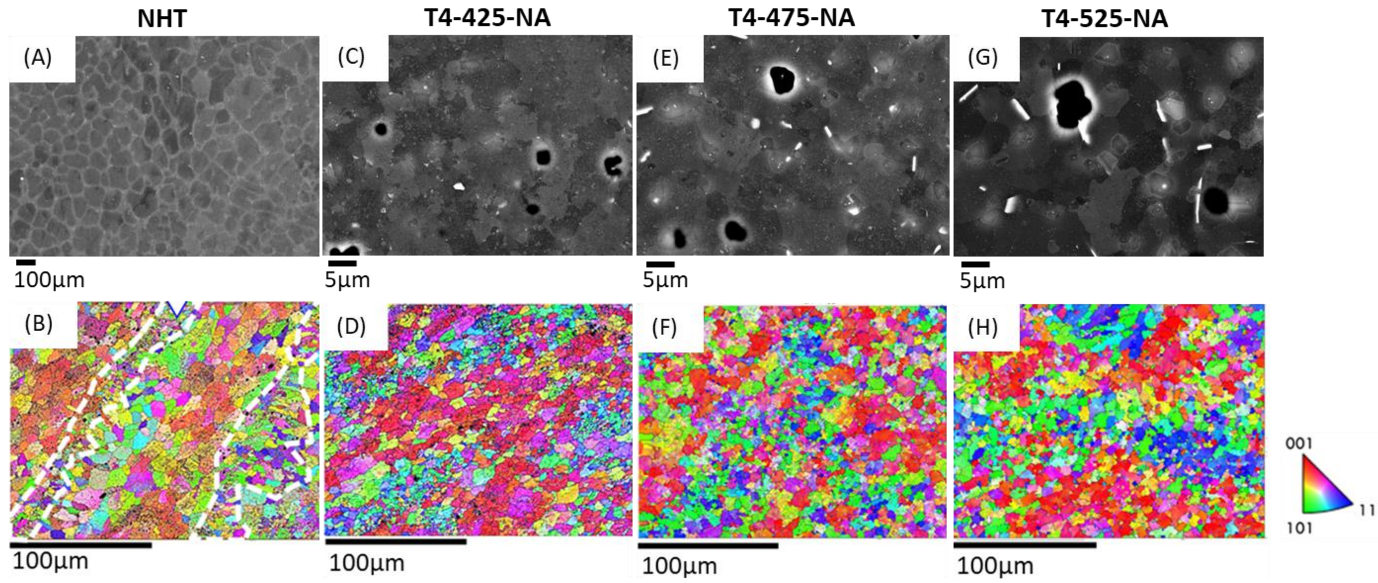

Figure 2. Microstructures of EOS L-PBF AlSi10Mg on x-y plane in the (A)-(B) non-heat treated (NHT) condition and (C)-(H) heat treated conditions. The BSE micrographs are presented at the top and the IPF plots obtained from EBSD analysis at the bottom.

The results of EDS analysis, including the elemental maps, are presented in Figure 3 for the T4-425-NA condition. There were two types of precipitates discernable within the α-Al grain interior in the BSE micrographs which were identified as the Si-particles and the β-AlFeSi phase precipitates. These precipitates had distinct morphologies with the Si-particles appearing in bulky forms and the β-AlFeSi phases having a needle shaped appearance, as also reported in literature for this alloy after solution treatment [46,51,57,58].

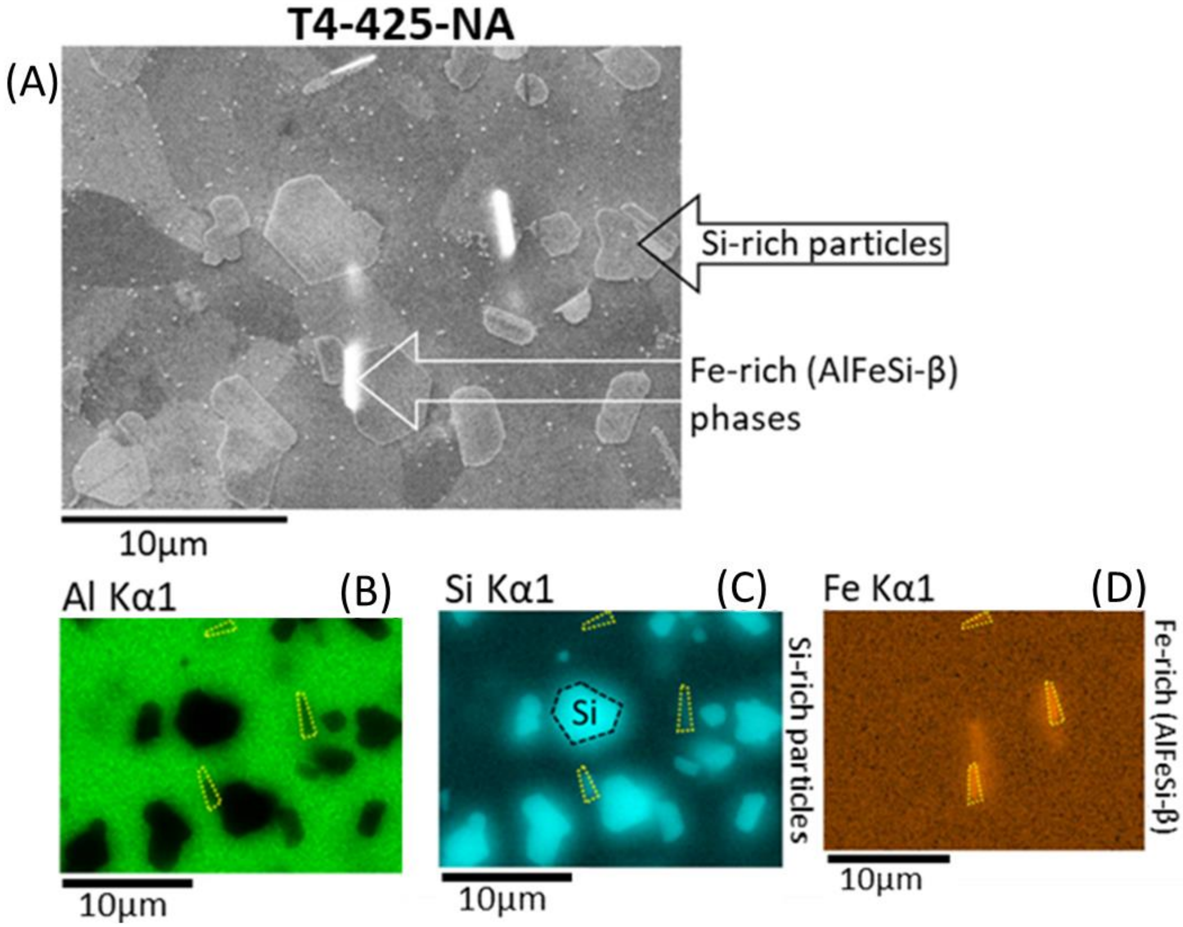

Figure 3. (A) BSE image and (B) – (D) the corresponding elemental maps for EOS L-PBF AlSi10Mg in T4-425-NA condition.

2.3.2. Tensile Properties

Engineering stress-engineering strain and the engineering stress-displacement curves are presented in Figure 4 (A)-(C) for the EOS specimens in various heat treated conditions. In addition, the tensile properties (including yield strength (S_y), ultimate tensile strength (S_u), Young's modulus (E), elongation to failure (%El) and true fracture strain (ε_f)) are reported in Table 2 along with those of similar aluminum alloys from literature, including the A356 cast alloy [54,59] as well as wrought and L-PBF AA6061 alloy [60,61]. The highest strengths were found in the non-heat treated condition with the yield (see Figure 4 (A)) and ultimate tensile (see Figure 4 (A) & (B)) strengths being 241 MPa and 516 MPa, respectively. After the T4 treatments, a significant drop in tensile strength was observed accompanied by an increase in ductility, with the %*El* being measured as 14%, 20%, 25% and 15% for the NHT, T4-425-NA, T4-475-NA and T4-525-NA conditions, respectively. The variation in the tensile strengths, as seen in Figure 4 (B), can be attributed to the varying degrees of solid solution from the different T4 temperatures. Subsequent artificial aging in the T7 specimens was able to induce precipitation hardening [62], which resulted in tensile strengths being partially recovered along with some loss in ductility, as seen in Figure 4 (C).

Tensile properties may provide an indication of fatigue behavior in different fatigue regimes, for example, material's sensitivity to the presence of defects in the high cycle fatigue regime typically increases with strength [8]. Based on this, the authors selected three conditions for fatigue testing, namely, T4-425-NA, T4-525-NA and T7-475-165, that represent a relatively large variation in strength and acceptable ductility (i.e., %*El* ≥ 13% and $\varepsilon_f \geq 25\%$). Among these conditions, T4-425-NA condition has the highest amount of ductility and the lowest strength. T7-475-165 provides the highest strength, while also retaining acceptable ductility as shown in Figure 4 (C). Finally, the strength and ductility of T4-525-NA condition are intermediate of the former two. As indicated by the comparison shown in Table 2, applying aging treatments (T7) to L-PBF AlSi10Mg and L-PBF A356 alloys resulted in similar tensile strengths and ductility. When compared with other conventionally manufactured aluminum alloys, T7-475-165 had higher ductility and tensile strengths than cast-T6-A356, but lower tensile strengths than wrought-T6-AA6061, with the measured elongations being similar.

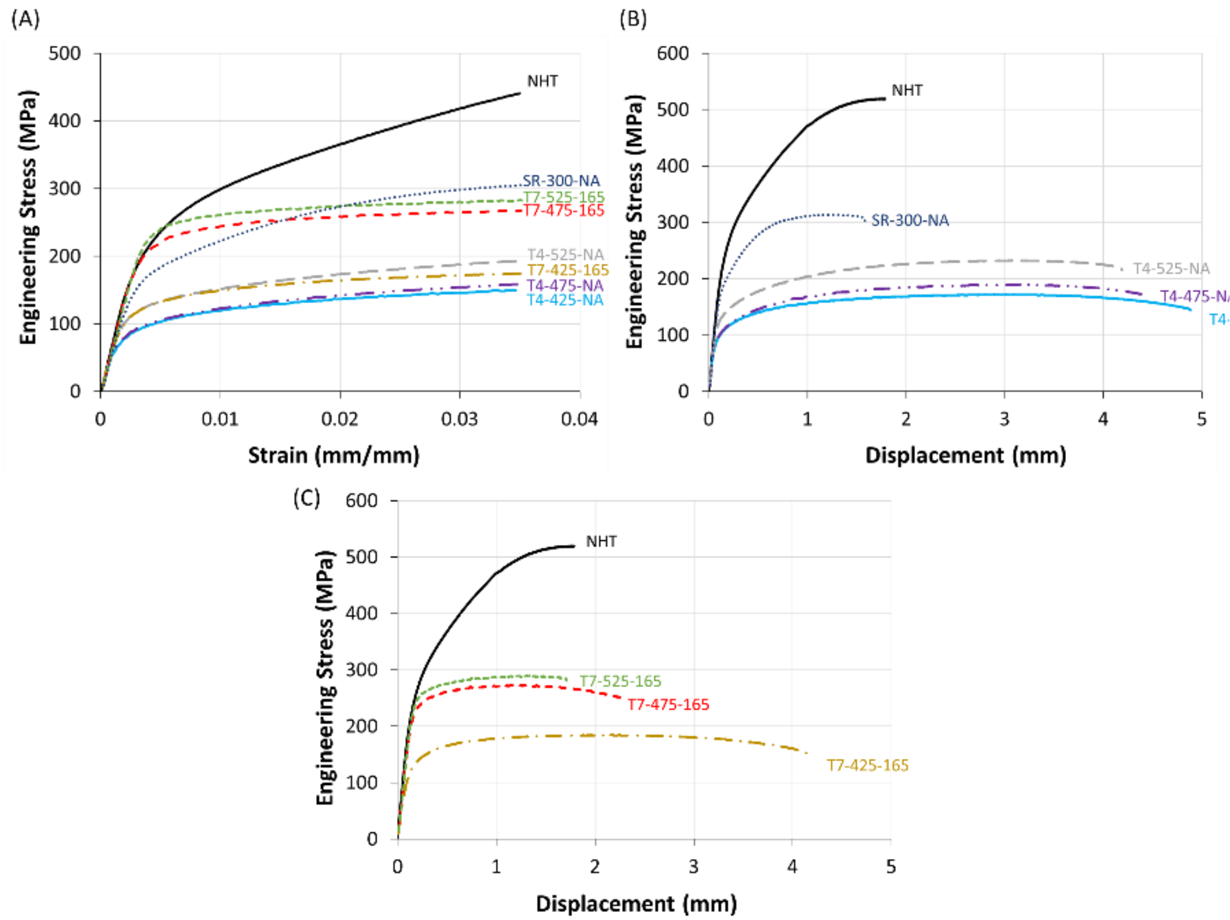

Figure 4. Tensile curves of EOS L-PBF AlSi10Mg in various heat treated conditions: (A) engineering stress-engineering strain curves, and (B) & (C) engineering stress-displacement curves for the solution + naturally aged and solution + artificially aged conditions, respectively. Additionally, for comparison, the tensile results of SR-300-NA [30] is added in (A) and (B).

Table 2. Tensile properties of EOS L-PBF AlSi10Mg under various heat treatments compared with other aluminum alloys from literature [54,59–61]. In addition, the tensile properties of SR-300-NA condition published earlier [30] is also included.

Alloy	Process	Heat treatment	S_y (MPa)	S_u (MPa)	E (GPa)	%El	ε_f (%)	Ref.
AlSi10Mg	L-PBF	NHT	241±1	516±3	73±1	14±1	7±1	This study
		T4-425-NA	88±1	171±2	72±1	22±1	67±1	
		T7-425-165	121±2	186±1	72±1	22±1	53±3	
		T4-475-NA	91±2	191±1	72±1	21±3	51±1	
		T7-475-165	219±6	275±1	75±2	13±2	25±4	

		T4-525-NA	123±1	234±2	72±1	15±3	33±2	
		T7-525-165	238±2	294±3	71±2	9±2	19±2	
		SR-300-NA	189	302	74	19	48	[30]
A356	Cast	T6	195	228	-	2	-	[59]
	L-PBF	NHT	228	384	-	13	-	[54]
		T6	210	270	-	13	-	
AA6061	Wrought	NHT	55	124	-	30	-	[61]
		T6	276	310	-	12	-	
	L-PBF	NHT	71	137	-	13	-	[60]
		T6	286	313	-	4.5	-	

2.3.3. Cyclic Deformation and Fatigue Properties

The steady-state hysteresis loops (obtained at the midlife), for the EOS specimens in the three selected heat treated conditions, i.e., T4-425-NA, T7-475-165, and T4-525-NA, are presented in Figure 5. As seen, the specimens exhibited large cyclic plastic strains at the 0.0050 mm/mm strain amplitude and some degree of cyclic plastic deformation at 0.0030 mm/mm and 0.0020 mm/mm, regardless of their heat treatments. In contrast, at 0.0015 mm/mm, all three heat treatments resulted in purely elastic cyclic responses at their midlife. Among all heat treatments, T4-425-NA showed the largest plastic strain (i.e., the widest hysteresis loop) at almost all strain amplitudes, which was consistent with its more ductile quasi-static tensile behavior, shown in Figure 5 (B)-(D). Furthermore, for all of the heat treatments investigated, pronounced cyclic plasticity started to occur at the strain amplitude of ε_a = 0.0020 mm/mm even though the corresponding stress amplitudes were substantially lower than the S_y for the T7-475-165 and T4-525-NA conditions, while being higher than the S_y for the T4-425-NA condition (Figure 5 and Table 2).

The initial (at 500th cycle) and midlife cyclic stress-strain responses for specimens tested at ε_a = 0.0015 mm/mm are compared in Figure 6 for each of the heat treated conditions. It is apparent in Figure 6 (A)-(B) that a significant amount of cyclic hardening occurred for the T4 conditions between the first few cycles (initial) and the midlife, and the stress-strain response became fully elastic at the midlife. However, for the T7-475-165 condition, the cyclic response was observed to be fully elastic from the very start of the test and neither softening nor hardening was observed after the first few cycles.

The cyclic strength coefficient, *K*', and the cyclic strain hardening exponent, *n*', were calculated by fitting the following power law function to the midlife stress amplitude, σ_a, versus the plastic strain amplitude, $\Delta\varepsilon_p/2$, data for each heat treated condition:

$$\sigma_a = K'\left(\frac{\Delta\varepsilon_p}{2}\right)^{n'} \tag{2.1}$$

The cyclic stress-strain behavior was obtained using the Ramberg-Osgood (RO) relationship which can be expressed as:

$$\varepsilon_a = \frac{\Delta\varepsilon_e}{2} + \frac{\Delta\varepsilon_p}{2} = \frac{\sigma_a}{E} + \left(\frac{\sigma_a}{K'}\right)^{\frac{1}{n'}} \tag{2.2}$$

where $\Delta\varepsilon_e/2$ is the elastic strain amplitude and *E* is the Young's modulus of the material.

The RO fits superimposed on the monotonic stress-strain curves and the cyclic stress-strain data are presented in Figure 7. As seen in Figure 7 (A)-(B), the RO fits for the T4-425-NA and T4-525-NA conditions were above the monotonic curves which indicated a cyclic hardening behavior. For both of these T4 conditions, none of the cyclic data points fell on the monotonic curve, even at the lower strain levels. This was particularly interesting as the midlife hysteresis loops at ε_a = 0.0015 mm/mm for both T4-425-NA and T4-525-NA showed fully elastic behavior. In contrast, for the T7-475-165 condition, the RO fit appeared below the monotonic curve, as seen in Figure 7 (C), indicating a cyclic softening response.

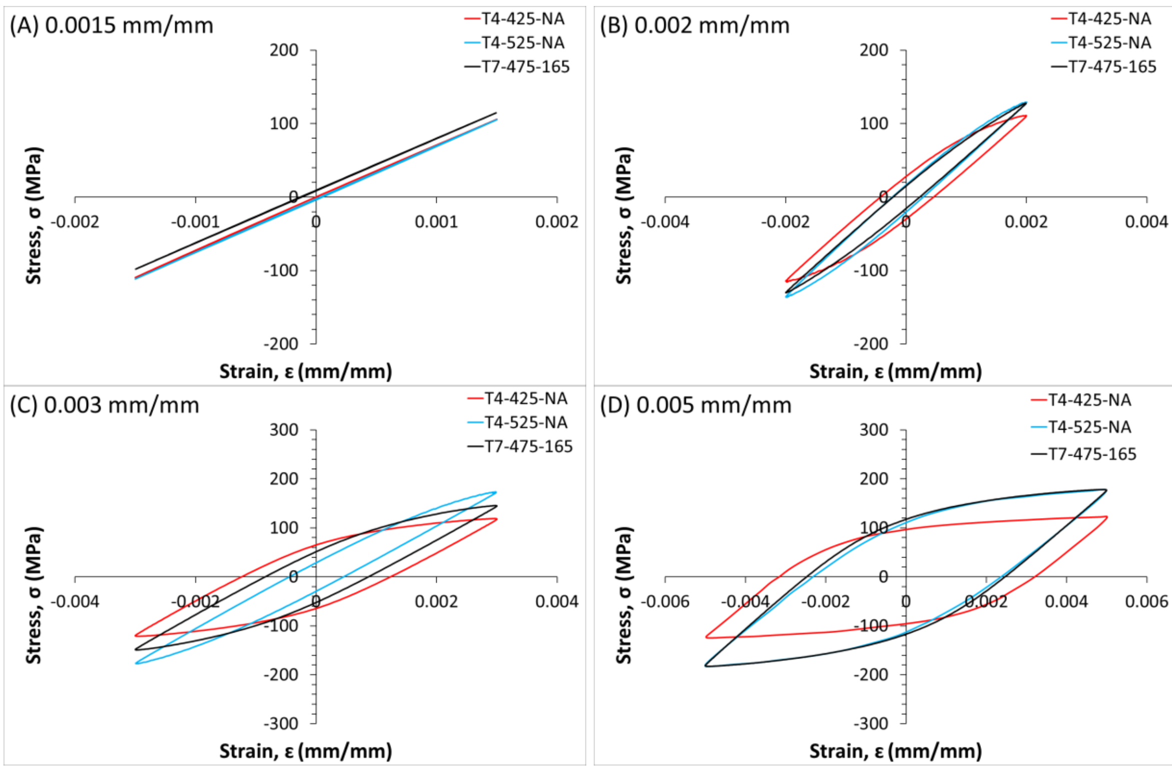

Figure 5. The steady-state cyclic stress-strain responses (hysteresis loops) for EOS L-PBF AlSi10Mg in the three different heat treated conditions tested at strain amplitudes of: (A) 0.0015 mm/mm, (B) 0.002 mm/mm, (C) 0.003 mm/mm, and (D) 0.005 mm/mm.

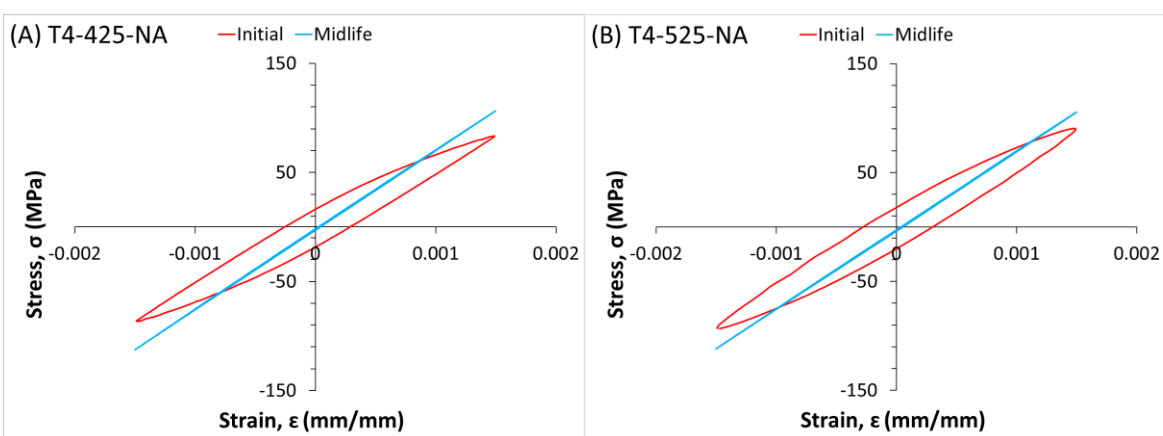

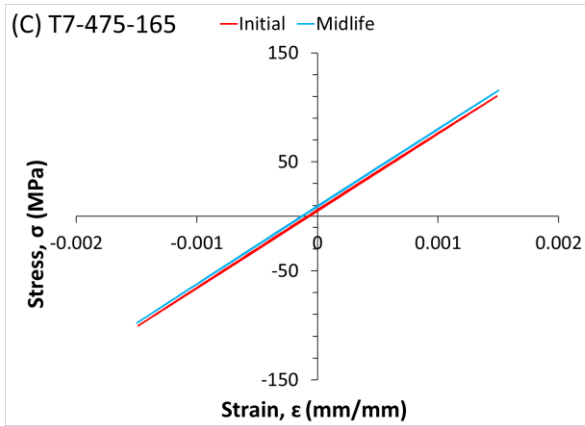

Figure 6. Initial (at the 500th cycle) and midlife cyclic stress-strain behavior of EOS L-PBF AlSi10Mg tested at ε_a=0.0015 mm/mm. The hysteresis loops are for (A) T4-425-NA, (B) T4-525-NA, and (C) T7-475-165 conditions.

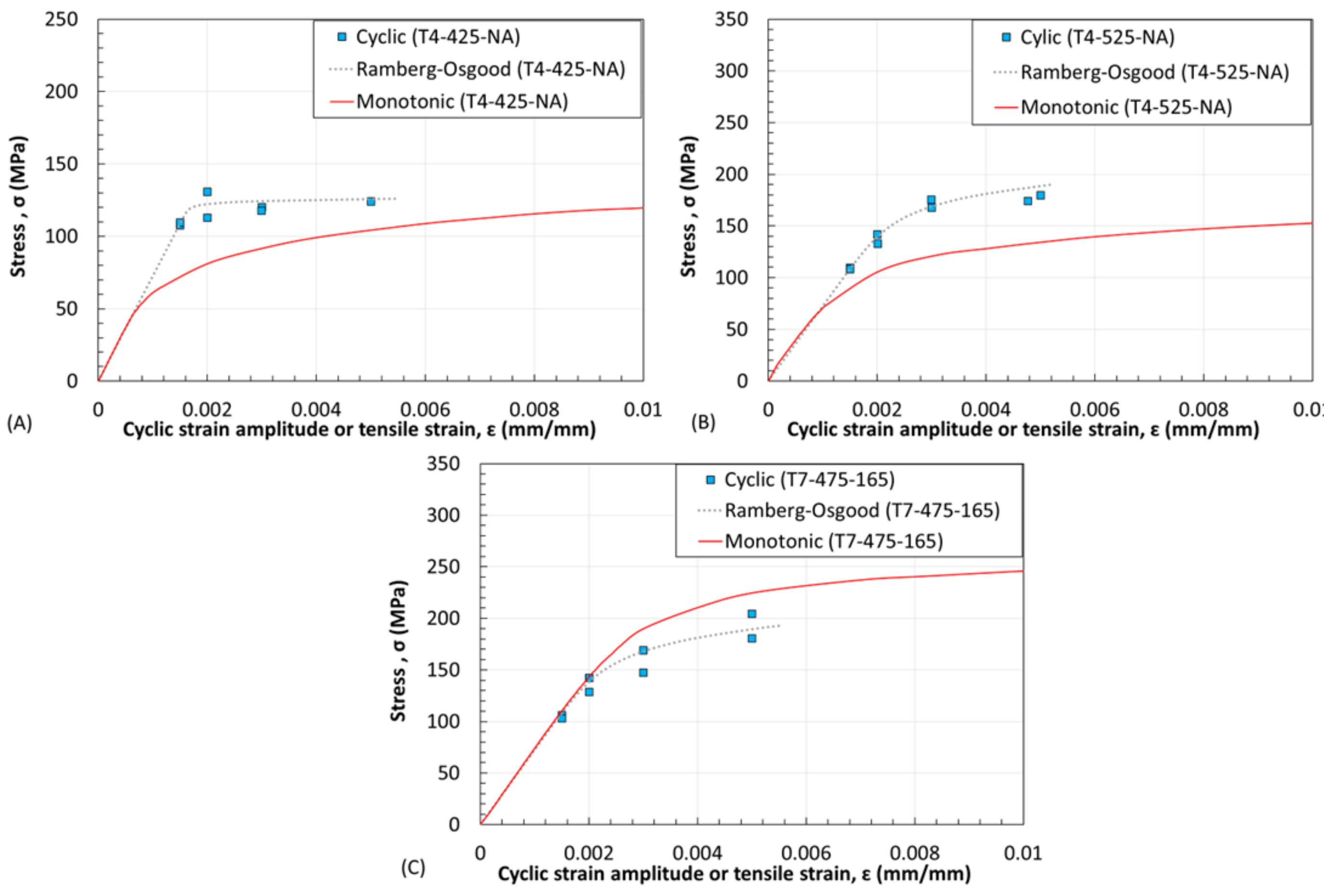

Figure 7. Ramberg-Osgood curves for EOS L-PBF AlSi10Mg plotted against the monotonic stress-strain curves and the cyclic stress-strain responses for (A) T4-425-NA, (B) T4-525-NA, and (C) T7-475-165 conditions.

The fatigue data for the selected heat treatments, i.e., T4-425-NA, T7-475-165, and T4-525-NA, is presented in Table 3. The plastic strain amplitude for each specimen was calculated using:

$$\frac{\Delta\varepsilon_p}{2} = \varepsilon_a - \frac{\Delta\varepsilon_e}{2} \tag{2.3}$$

It should be noted that in Table 3, the mean stress values, σ_m, were no more than 10% of the total stress amplitudes, σ_a; therefore, any mean stress effects can be considered negligible. Furthermore, whenever the fatigue critical defects were clearly visible on the fracture surfaces, Table 3 lists the projected root area ($\sqrt{area}$), calculated using Murakami's approach [63], of the defect on the plane perpendicular to the applied stress and its type (pores or lack of fusion (LoF's) defects). It should be mentioned that not all of the EOS specimens' fatigue fracture surfaces could be preserved for analysis. This was partly because the material showed relatively ductile tensile behavior in all of the heat treated conditions, which in turn lead to some of the fracture surfaces being damaged under compressive loading during fully-reversed cyclic testing (R= -1). As such, additional fatigue tests were conducted on the heat treated Renishaw specimens under tension-tension loading using a stress ratio of R=0.1 in order to preserve the fracture surfaces from any compressive damage during testing. The fracture surface analysis from this set of specimens was used to correlate the crack initiating defect characteristics with the fatigue lives.

The strain-life and the stress-life fatigue behaviors of the tested EOS specimens are presented in Figure 8 (A)-(B), respectively. For comparison, the results of SR-300-NA specimens from previously published work [30] are also included in these figures. As shown in Figure 8 (A), the different heat treatments resulted in similar strain-life fatigue behaviors. A single factor analysis of variance (ANOVA) was performed on the EOS fatigue dataset with a significance level (α) of 0.05. The results from the ANOVA analysis showed p-values >0.05, indicating any differences from heat treatments were not statistically significant. As seen in Figure 8 (B), the cyclic stress responses of almost all the T7-475-165 specimens were below the corresponding yield strength of the alloy. For other conditions, including the SR-300-NA, there were some specimens whose stress responses were higher than or close to the corresponding yield strength. To compare the stress response of the specimens relative to their yield strengths, Figure 8 (C) presents the normalized stress-life data where the stress amplitudes were normalized with respect to their respective yield strengths. As shown, the normalized stress amplitudes of the T7-475-165 specimens were almost entirely below unity, i.e., the stress amplitudes were below the yield strength of the material. This was not the case for other T4 heat treatments with some of the normalized stress amplitudes being above one.

Table 3. Fatigue data for EOS L-PBF AlSi10Mg specimens in various heat treated conditions.

Heat treatment	**ID**	ε_a **(mm/mm)**	$\frac{\Delta\varepsilon_e}{2}$ **(mm/mm)**	$\frac{\Delta\varepsilon_p}{2}$ **(mm/mm)**	σ_a **(MPa)**	σ_m **(MPa)**	$2N_f$ **(Reversals)**	$\sqrt{area}$ **defect (µm)**
T4-425-NA	E44	0.0050	0.0018	0.0032	124	-2	1,384	N/A
	E39	0.0030	0.0018	0.0012	120	-1	9,254	N/A
	E42	0.0030	0.0016	0.0014	118	-2	4,276	N/A
	E38	0.0020	0.0016	0.0004	113	-2	30,828	N/A
	E36	0.0020	0.0019	0.0001	130	-2	120,004	55
	E43	0.0015	0.0015	0.0000	108	-2	594,184	N/A
	E46	0.0015	0.0015	0.0000	109	-3	440,222	N/A
T7-475-165	E6	0.0050	0.0030	0.0020	181	-2	2,658	N/A
	E12	0.0050	0.0033	0.0017	204	-3	1,230	N/A
	E3	0.0030	0.0025	0.0005	147	-2	12,648	75
	E9	0.0030	0.0025	0.0005	169	1	25,296	10
	E7	0.0020	0.0019	0.0001	142	2	309,946	N/A
	E1	0.0020	0.0018	0.0002	129	-1	45,836	101
	E10	0.0020	0.0019	0.0001	142	-2	206,930	43
	E13	0.0015	0.0015	0.0000	103	-1	163,350	149
	E17	0.0015	0.0015	0.0000	106	8	6,697,716	N/A
T4-525-NA	E30	0.0050	0.0028	0.0022	180	-3	1,080	N/A
	E22	0.0047	0.0024	0.0023	174	-3	994	N/A
	E26	0.0030	0.0025	0.0005	168	-2	12,568	63
	E24	0.0030	0.0026	0.0004	176	-2	12,014	66
	E23	0.0020	0.0019	0.0001	133	-3	51,604	N/A
	E19	0.0020	0.0020	0.0000	142	-4	118,728	55

E27	0.0015	0.0015	0.0000	109	-3	213,658	N/A
E34	0.0015	0.0015	0.0000	109	-3	2,136,532	N/A

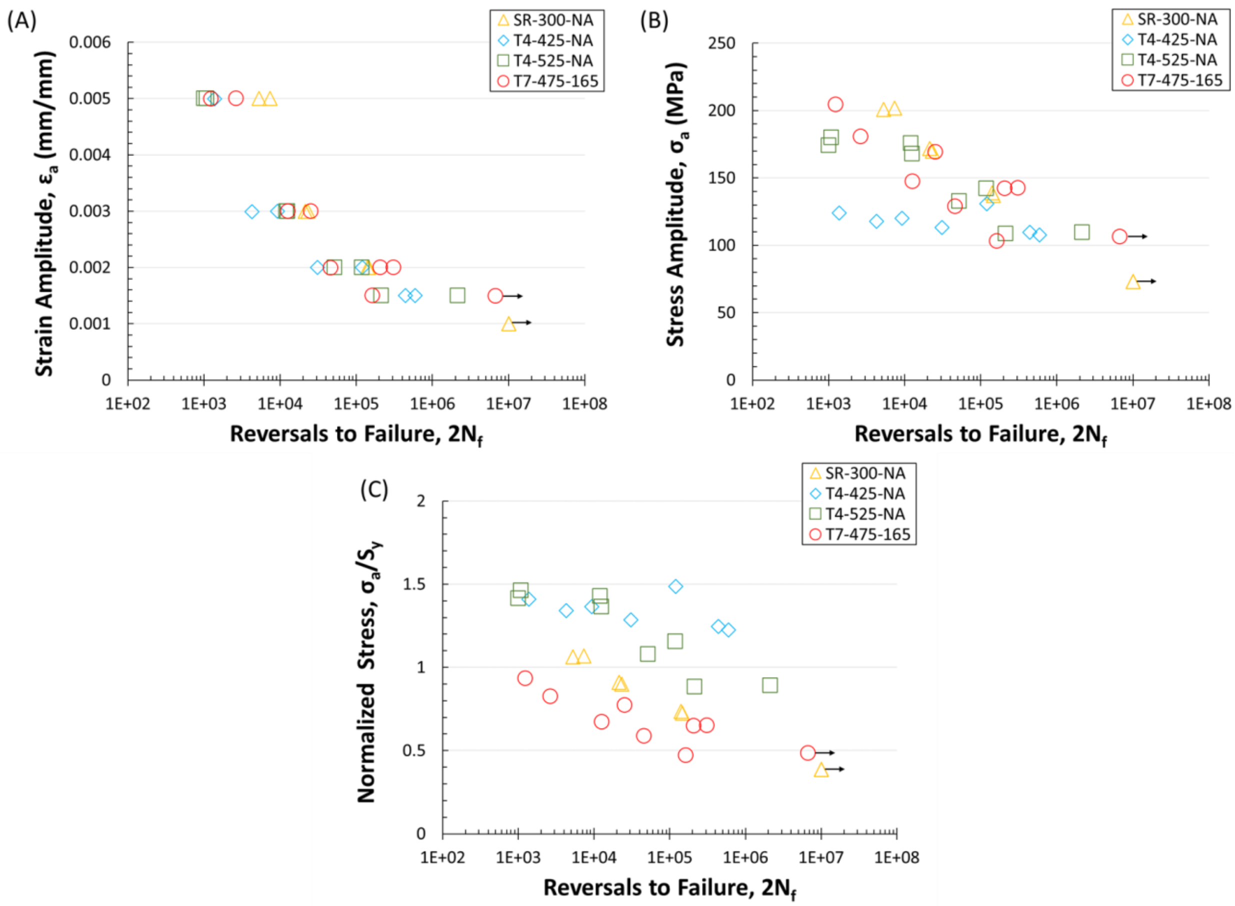

Figure 8. Comparison of uniaxial fatigue behavior of EOS L-PBF AlSi10Mg specimens in machined surface conditions: (A) strain-life fatigue response, (B) stress-life fatigue response, and (C) normalized stress-life fatigue response with stress amplitudes divided by the corresponding yield strengths. Additionally, the results of stress relieved specimens (SR-300-NA) of the same alloy published earlier [30] are included for comparison.

Due to some of the fracture surfaces being damaged during fully-reversed cyclic loading, the additional heat treated and machined Renishaw AlSi10Mg specimens were tested under force-control mode according to ASTM E466 [43] in order to examine the effect of crack initiating defects' characteristics on the fatigue lives. All specimens were tested at a single stress-level of σ_{max} = 90 MPa under tension-tension loading at a stress ratio of R=0.1. The final fatigue properties for these specimens are presented in Table 4 along with the crack initiating defect sizes which were measured using Murakami's $\sqrt{area}$ approach [63]. Similar to the EOS dataset, the single factor

ANOVA results for the Renishaw fatigue dataset showed p-values >0.05 (with α=0.05), suggesting the differences in fatigue performance between the three heat treatments were not statistically significant.

Table 4. Fatigue data for additional L-PBF specimens fabricated on Renishaw AM250, tested under force control-mode at σ_{max}=90 MPa and R = 0.1.

Heat Treatment	ID	σ_{max} (MPa)	$2N_f$ (Reversals)	$\sqrt{area}$ of defect (µm)
T4-425-NA	R06	90	5,212,454	515
	R05	90	1,697,768	672
	R08	90	1,295,732	612
	R10	90	806,546	699
T7-475-165	R22	90	5,023,474	458
	R17	90	2,615,080	484
	R20	90	1,763,490	708
	R15	90	1,760,504	614
T4-525-NA	R29	90	6,339,302	602
	R32	90	3,643,534	513
	R33	90	2,582,058	664
	R26	90	2,274,160	673

2.4. Discussions

2.4.1. Tensile Behavior

As shown in Figure 4, L-PBF AlSi10Mg has the highest tensile strength in the non-heat treated condition. This could be attributed to the dendritic microstructure that was formed during the deposition process of the alloy [64,65] where the inter-dendritic regions (as shown in Figure 2 (A)-(B)) were effective barriers to dislocation's motion. Upon low temperature stress relieving at 300 °C for 2 h (i.e., SR-300-NA specimens [30]), the dendritic microstructure was partially removed, resulting in slightly improved ductility at the cost of some reduction in strength which was still higher than the strength of the solution treated and artificially aged specimens.

Furthermore, upon solution treatment as shown in Figure 4, the alloy exhibited a significant drop in tensile strength, while the ductility largely improved, which could be explained partly by the complete dissolution of the inter-dendritic regions (see Figure 2 (A) and (C)). However, it can be seen in Figure 4 that increasing the temperature of solution treatments resulted in higher strength. This can be ascribed to the higher degree of supersaturated solid solution in the α-Al matrix [50]. The increase in solution temperature, although increases the solubility of Si in Al, can significantly coarsen the Si-rich precipitates (Figure 2 (C, E, G)). These coarse precipitates can induce more severe dislocation pile-ups and are more effective as void nucleation sites under tensile loading, as was observed in the EDS micrographs of the tensile fracture surfaces (**Figure 9**). This explains why the ductility decreased with an increase in solution temperature, where the larger sized Si precipitates left large voids in the matrix under tensile loading and led to early fracture. Moreover, upon subsequent artificial aging at 165 °C for 16 h (T7), the tensile strength was partially recovered. The high tensile strength in the T7 condition could be partly derived from Si-rich precipitates and the Fe-rich phases, as seen in Figure 3, however, their contribution was believed to be minimal due to the large size, low quantity and non-uniform distribution throughout the specimens. The main strengthening mechanism was believed to be due to the formation of nano-sized Mg_2Si precipitates which was expected upon further T7 heat treatment. Limited by the resolution of the SEM, the authors were not able to detect these small precipitates in their analysis, nevertheless, these precipitates have been well reported in literature for the solution + artificially aged conditions in both, wrought and AM forms [66–68] Among the three heat treatments that were studied for further fatigue testing; i.e., T4-425-NA, T4-525-NA and T7-475-165, the T7 condition showed the highest tensile strength (i.e., S_y=~219 MPa and S_u=~275 MPa), while exhibiting the lowest ductility (%El=~13%), as seen in Figure 4 (C).

The scanning electron micrographs of tensile fracture surfaces in low and high magnifications as well EDS elemental maps of dimples for the selected heat treatments are presented in Figure 9. Relatively large particulates (a few microns in size) were found within the dimples which indicated the possible involvement of the large precipitates in the void nucleation mechanism. Indeed, as seen in the elemental maps, the fracture surfaces for all heat treatments contained particles inside dimples (shown by green arrows) that were rich in Si, and depleted in Al, Mg, Fe. These dimples could be the result of voids nucleated from the decohesion of Si-particles from the α-Al matrix and/or the particle fracture under load. The fact that other types of precipitates were not identified on the fracture surfaces may indicate weak Al matrix-Si particle bonding as well as the brittleness of the Si-particles. This is particularly interesting because typically in other aluminum alloys [69], the Fe-bearing intermetallic phases act as void nucleation sites under uniaxial tensile loads which is mainly because of their detrimental needle-shape morphologies with high stress concentration levels, such as the Fe-bearing Cu_2FeAl_7 intermetallic phases in Al-7000 alloys [70].

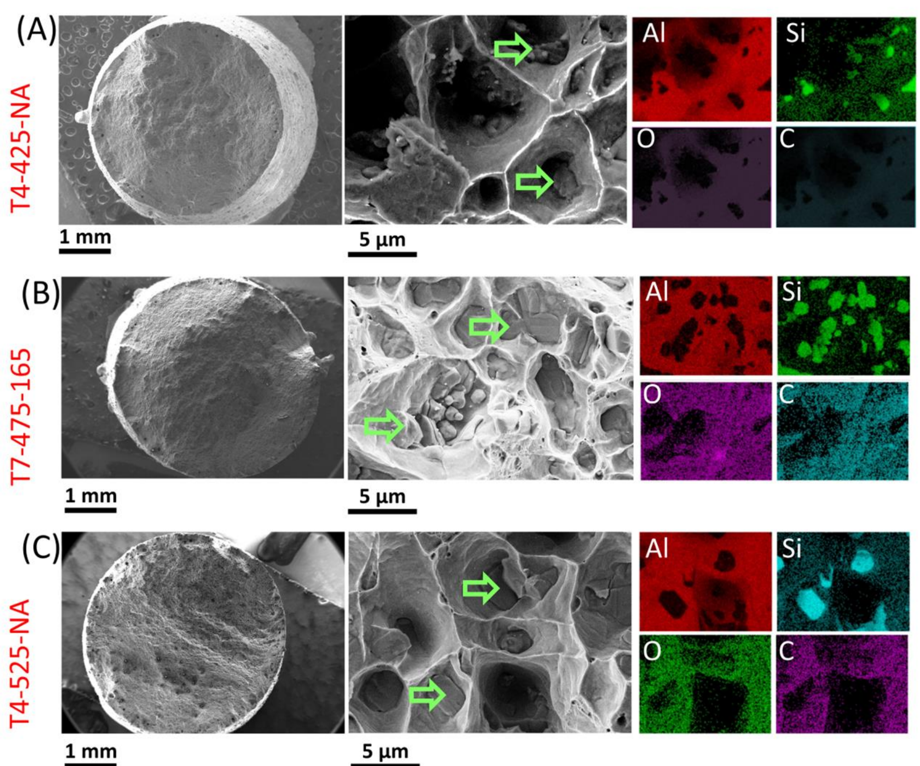

Figure 9. Tensile fracture surfaces of the EOS L-PBF AlSi10Mg alloy in various heat treatments: (A) T4-425-NA, (B) T7-475-165, and (C) T4-525-NA. Note that the green arrows point at the Si-particles as void nucleation sites.

2.4.2. Fatigue Behavior

As shown in Figure 8 (A), the various heat treatments investigated appear to have little effect on the fatigue lives of EOS L-PBF specimens. There is a large amount of scatter present at the lower strain levels of 0.0015 mm/mm. In this fatigue regime, crack initiation dominated most of the life with the near surface pores and LoF's, which were present in all of the conditions, acting as stress concentration sites. These defects had varying characteristics (i.e., size, shape, distance to the surface, etc.) [6,71] from specimen to specimen, and thus, could lead to varying degrees of stress concentrations. In comparison, at the higher strain level of 0.005 mm/mm, the fatigue scatter was observed to be lower. In this regime, crack propagation dominated the fatigue lives which was influenced by the microstructural features. This would explain why slightly better fatigue performance was observed for the SR-300 condition where its dendritic cellular structure could help control the rate of short crack propagation as compared to the T4/T7 conditions where this cellular structure dissolved into the α-Al matrix due to the high solution temperatures. In all cases, despite the different microstructures obtained from the heat treatments, fatigue cracks always initiated due to the stress concentrations caused by the volumetric defects, where cyclic damage is localized and accumulates. The localized damage accumulation seen in fatigue loading is quite different from the damage mechanisms governing the tensile response, which is highly sensitive to the microstructures. In tensile loading, the whole microstructure participates in deformation, and the damage distribution is relatively more uniform.

Cyclic hardening/softening behavior can be observed in Figure 7, with both of the T4-425-NA and T4-525-NA conditions displaying cyclic hardening and T7-475-165 showing cyclic softening. The T4 conditions tested at 0.0015 mm/mm were of particular interest as they display plastic deformation in their hysteresis loops for the first few hundred cycles after which their stress-strain response became fully elastic. The low volume fraction of Mg_2Si precipitates in the T4 conditions, as has been reported in literature [72], allowed rapid dislocation multiplication under cyclic loading leading to a cyclic hardening response [73,74]. In the T7-475-165 condition, the subsequent aging step below the Mg_2Si solvus allowed the growth and formation of additional precipitates [73]. These precipitates, although were effective dislocation barriers under monotonic loading, could be sheared by the repetitive motion of dislocations in persistent slip bands leading to mechanical dissolution of precipitates over time under cyclic loading, which would possibly explain the softening response observed in the T7 condition [75].

The results of quantitative image analyses for defect sizes, measured using Murakami's $\sqrt{area}$ parameter [63], on the fatigue fracture surfaces are presented in Table 3 for the T4-425-NA, T7-475-165 and T4-525-NA EOS specimens. It was noteworthy that the average $\sqrt{area}$ of the initiating defects for the artificially aged specimens (T7-475-165) tested at 0.0020 mm/mm strain amplitude were calculated to be 101 μm (with 45,836 reversals to failure) which was about two times larger than the other two solution treated specimens, i.e., T4-425-NA , T4-525-NA , whose average $\sqrt{area}$ values were 55 μm (with respective 120,004 and 118,728 reversals to failure). This was important because it could imply that the fatigue lives had a much stronger correlation with the defect sizes rather than any microstructural features. however, most of the fracture surfaces were damaged under the compressive stresses of fully-reversed loading, so a conclusion could not be made based on the EOS specimens. Some of the fracture surfaces for the specimens from the three different heat treated conditions are presented in Figure 10, showing the volumetric defects responsible for initiating fatigue cracks. All non-damaged fracture surfaces showed fatigue cracks initiated from volumetric defects in the machined condition. If the specimens were in the unmachined surface condition, fatigue cracks would be expected to initiate prematurely from the surface notches with high stress concentrations, leading to reduced fatigue life [30,76,77].

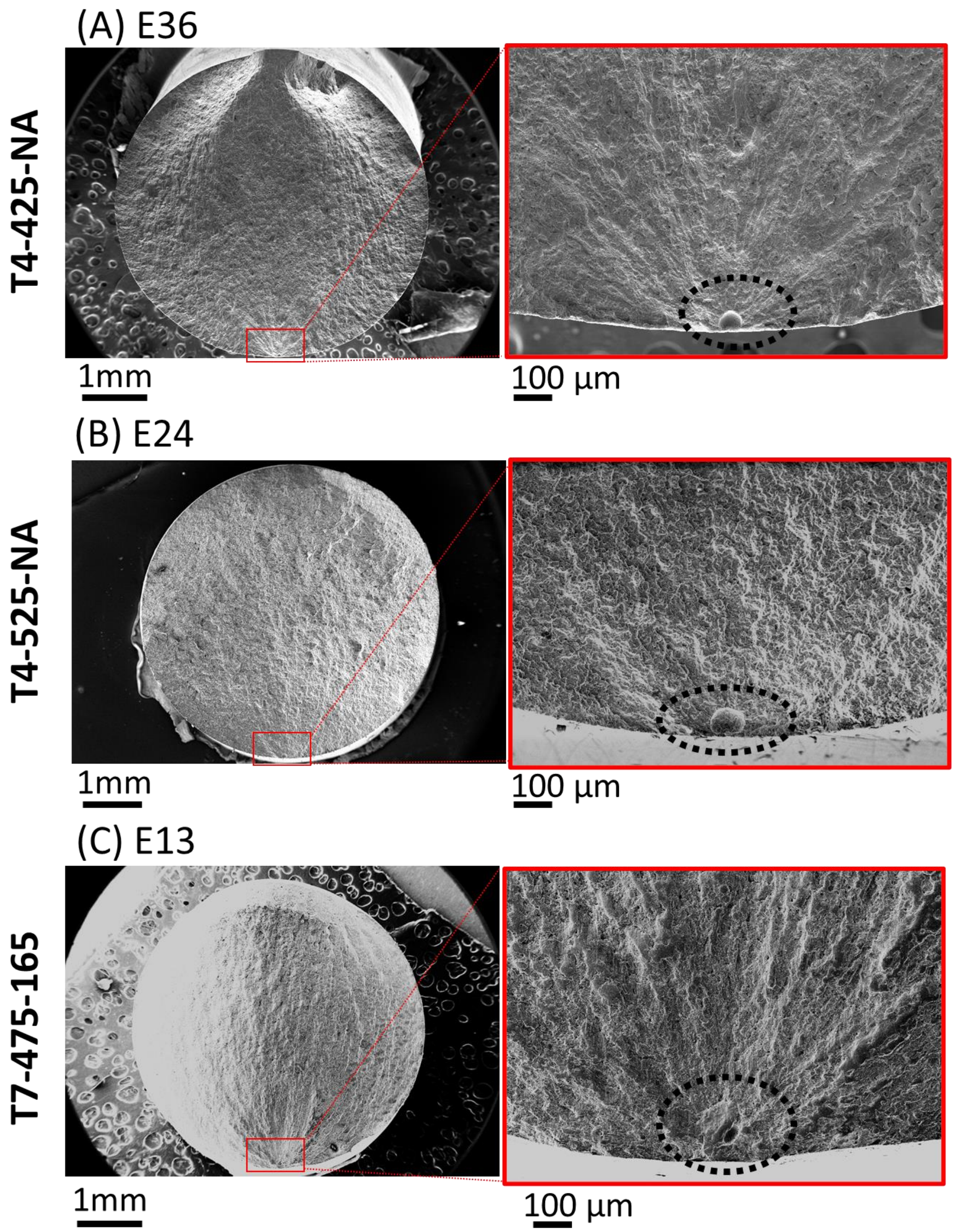

Figure 10. Fatigue fracture surfaces of EOS L-PBF AlSi10Mg specimens tested in the machined surface condition: (A) T4-425-NA, (B) T4-525-NA, (C) T7-475-165.

In order to further examine the role of defects in the fatigue lives of L-PBF AlSi10Mg as compared to any microstructural differences, the measured crack initiating defect $\sqrt{area}$'s were plotted against the reversals to failure in Figure 11 for the additional Renishaw specimens, which were tested under tension-tension loading to preserve the fracture surfaces. These tests were performed in the high cycle fatigue regime, where crack initiation (from the volumetric defects) dominated a large portion of the fatigue lives. As seen, regardless of the heat treatment, the presence of smaller defects resulted in improved fatigue lives and vice versa. Despite the three batches of specimens having undergone different heat treatments, thus having different microstructures, there was no clear trend discernable for any particular heat treatment resulting in better fatigue performance, as also seen in Table 4. Although T4-525-NA specimens showed slightly better fatigue performance, the effect of defect size appeared to be much more significant. Furthermore, the size of defects for Renishaw specimens was found to be much larger compared to the EOS specimens (see Table 3). This was most likely due to the process parameters for Renishaw AM250 having lower energy density values than EOS, which resulted in large LoF's present in all of the specimens. However, there could be other defect characteristics that influenced the results [71,78] which would explain why some specimens had different fatigue lives despite their $\sqrt{area}$'s being similar.

Scanning electron micrographs for some of the fracture surfaces of the Renishaw specimens are presented in Figure 12. The shortest fatigue life was observed for specimen R10 (806,546 reversals), shown in Figure 12 (A). For this specimen, despite the measured $\sqrt{area}$ being comparable with R05, R26, and R20 (Table 4), the existence of multiple, large, open to the surface LoF's adjacent to each other, led to early fatigue failure. In specimens R32 and R22 (Figure 12

(B) and (C)), the $\sqrt{area}$ was measured to be the smallest between their respective heat treatments, however, these were not the best performing specimens in the Renishaw dataset. This could be due to the existence of large LoF's present internally in the specimens, along the path of crack propagation as indicated by the yellow arrows, resulting in shorter fatigue lives. Since all of the defect areas were calculated using Murakami's projected $\sqrt{area}$ approach, some small variations were to be expected between each measurement. This was because the envelope considered for each measurement could be interpreted slightly differently. While the fatigue lives from the two load ratios (R=-1 and R=0.1) were not directly comparable with one another, they provided us with similar conclusions regarding the size/shape of the defects having a much greater impact on the fatigue lives of L-PBF AlSi10Mg, compared to any other microstructural differences.

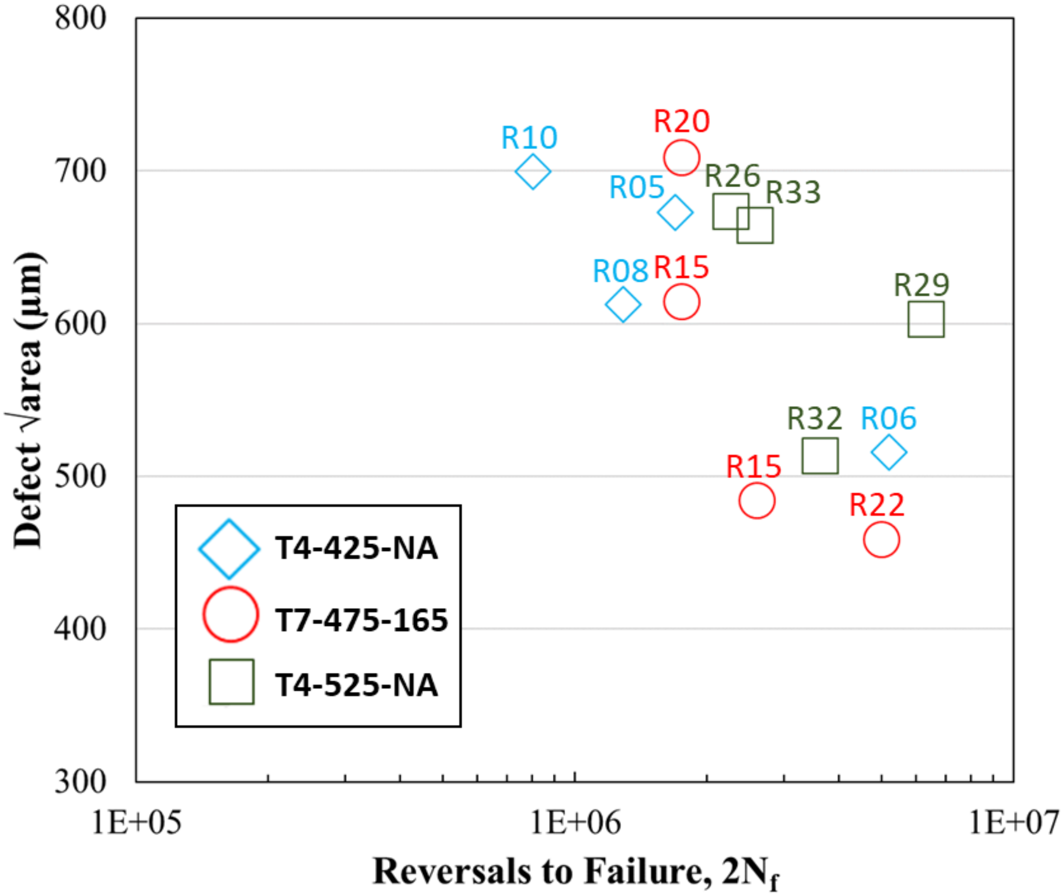

Figure 11. The measured defect $\sqrt{area}$ vs. reversals to failure for heat treated specimens fabricated on Renishaw AM250.

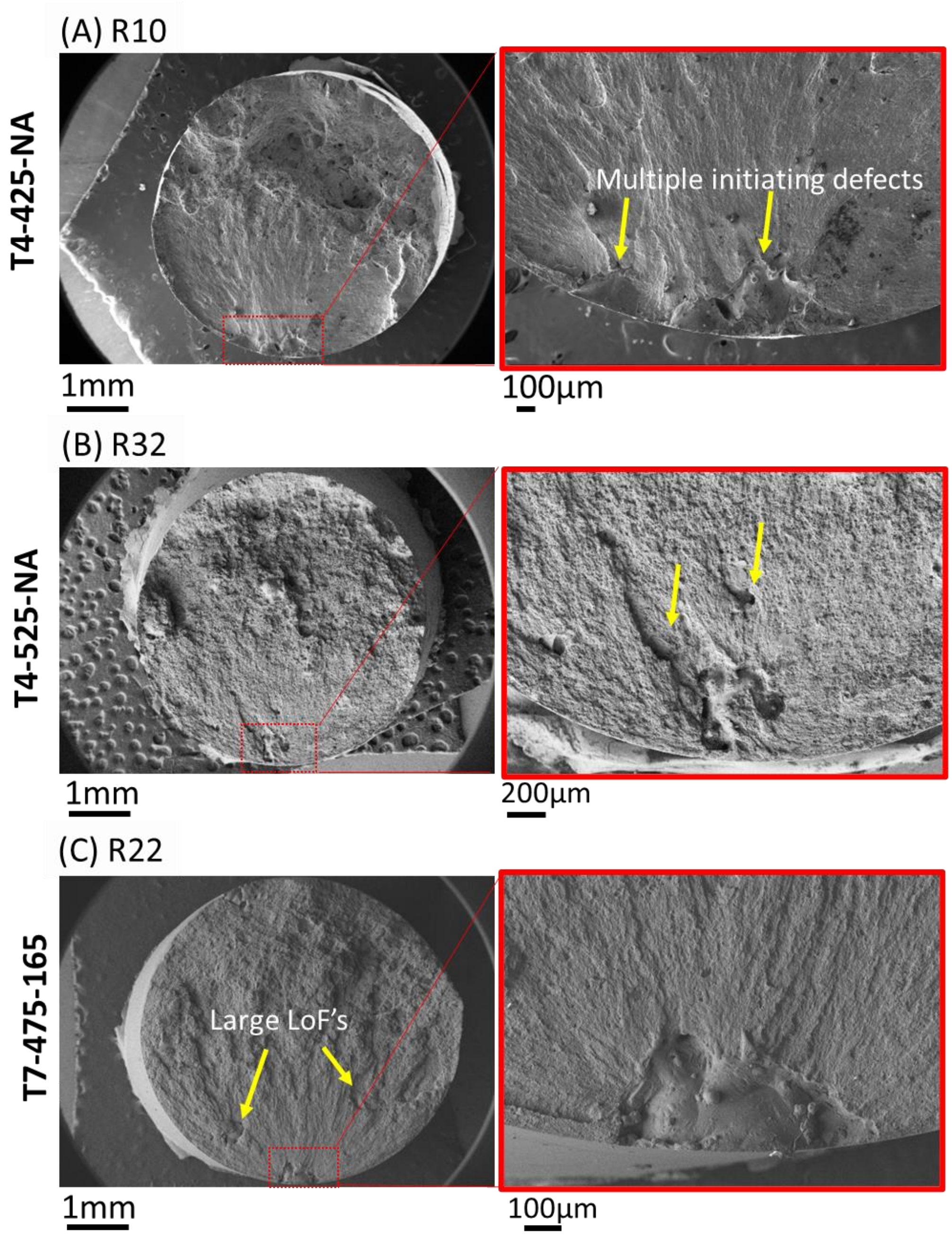

Figure 12. Fatigue fracture surfaces for L-PBF specimens fabricated on Renishaw AM 250 and tested at σ_{max}=90 MPa and R=0.1 for: (A) T4-425-NA, (B) T4-525-NA, and (C) T7-475-165 conditions.

2.5. Conclusions

The effect of heat treatment on microstructure, tensile, and fatigue behavior of L-PBF AlSi10Mg was investigated in this study. The experimental observations revealed that the tensile behavior of the alloy showed significant dependency on the AM induced microstructural features such as the grain structure, the Si-, β-AlFeSi, and Mg_2Si phases while the fatigue performance of the material had strong dependency on the AM induced defects, i.e., pores and lack of fusions. The following conclusions were drawn:

1. Due to the AM induced fine dendritic microstructure, the non-heat treated specimens showed higher tensile strengths and lower ductility compared to the other heat treated conditions investigated in this study.
2. Upon solution treatment, the prior micro segregation was almost entirely dissolved into the α-Al matrix and two types of precipitates were formed, i.e., the Si-particles and β-AlFeSi at the grain boundaries and grain interiors.
3. The specimens with T4 treatments showed more ductile tensile behaviors with higher elongations to failure and lower strengths, whereas the specimen with T7 treatments had lower elongation to failure with higher strengths attributed to the formation of Mg_2Si precipitates.
4. Brittle and bulky shape Si-particles were found to be the primary void nucleation sites on the tensile fracture surfaces of all heat treated conditions, while the needle shape β-AlFeSi phases remained uncracked under tensile loading.
5. All specimens, regardless of the applied heat treatment, exhibited comparable fatigue lives. Cyclic softening was observed in the specimens in T7 conditions and cyclic hardening for the specimens in T4 conditions.
6. The fatigue fracture surfaces revealed that the near surface AM induced defects such as pores and LoF's served as the crack initiation sites for the surface machined fatigue specimens. Further analysis of the crack initiating defects revealed, while fatigue lives for

L-PBF AlSi10Mg were mostly governed by the characteristics of AM induced defects, regardless of the microstructural differences.

3. Fatigue-defect criticality in laser powder bed fused aluminum alloys

3.1. Introduction

Aluminum (Al) alloys are valued for their decent strength-to-weight ratio, machinability, excellent corrosion resistance, and high thermal conductivity. Such properties make them ideal for fabricating lightweight components used in a range of industries including automotive, medical, and aerospace [9,79]. In recent years, additive manufacturing (AM) technologies have become a popular choice to fabricate complex Al parts, offering greater design flexibility than conventional processes [10]. AM techniques such as laser powder bed fusion (L-PBF) are well-suited for processing Al alloys with proper weldability, enabling fabrication of near-net shape geometries with acceptable precision, topology optimized parts for further lightweighting, and rapid prototyping [80]. Among these alloys, AlSi10Mg has been studied extensively in literature and is one of the most promising laser powder bed fused (L-PBF) alloys due to its low coefficient of thermal expansion which can allow complex geometries to be fabricated with adequate dimensional accuracy [81–83]. Other more recently developed high performance Al alloys include Scalmalloy, which has been specifically designed for the AM process and exhibits excellent weldability and exceptional tensile strength, outperforming other traditional Al alloys [40,84].

While the monotonic mechanical properties (e.g., tensile/compressive strength and ductility) of L-PBF Al alloys are comparable, and in many cases superior to their wrought counterparts, their fatigue behavior is often inferior —even in machined surface condition— due to the presence of process-induced volumetric defects [34,85,86]. The repetitive, rapid melting-solidifying of the material with each layer gives rise to these inherent defects which act as stress concentrators and under cyclic loading can lead to crack initiation and premature failure. Numerous studies have reported the detrimental effects of volumetric defects on the fatigue behavior of L-PBF Al alloys [11,87,88]. For example, Ngnekou investigated the impact of T6 heat treatment on the fatigue behavior of L-PBF AlSi10Mg and found that large defects have the dominant influence on the fatigue limit independent of the microstructure [89]. Similarly, Baig et al. also reached comparable conclusions for AlSi10Mg subjected to various heat treatments, noting that the defect size strongly correlated with the fatigue lives in all heat treated conditions [19].

The presence of volumetric defects can also alter how the microstructure influences the fatigue behavior [90,91]. In wrought alloys, where the population of volumetric defects is very low, finer microstructures are typically understood to be more resistant to crack initiation and better suited for applications in the high cycles fatigue regime where most of the fatigue life is spent in crack initiation [92]. Conversely, coarser microstructures are better suited in low cycle fatigue applications where crack propagation dominates fatigue life [93]. However, for AM materials, fine grain (FG) microstructures are typically more defect sensitive compared to coarse grain ones and can lead to deteriorated fatigue resistance [94–96]. In contrast, when a defect is located in a coarse grain (CG) region with grain sizes larger than the defect size, microstructurally mediated crack initiation mechanisms such as persistent slip bands can govern fatigue failure. As such, the size of the microstructure relative to the defect size is a key factor in determining the defect sensitivity of Al alloys.

Therefore, it is important to understand how defect features affect the fatigue behavior of L-PBF Al alloys in the context of varying microstructures and defect populations. Specifically, existing literature lacks an understanding of the defect-fatigue relationships in Al alloys, considering the influence of different types of defects with varying features and their interaction with the surrounding microstructures under cyclic loading. While some knowledge exists regarding the correlation between defect features and fatigue behavior of specific Al alloys, how this transfers to others with different defect sensitivities remains elusive [6,78,97–99]. Moreover, there is a lack of information on how defect features correlate with fatigue behavior in materials that exhibit bimodal microstructures such as Scalmalloy, which contains both extremely fine and moderately coarse grained regions.

This study investigates the influence of defect-structure on the fatigue behavior of two Al alloys with distinct microstructures; AlSi10Mg and Scalmalloy. Specimens have been fabricated for both alloys in three different orientations by varying the process parameters to induce common types of volumetric defects; lack-of-fusions (LoFs), gas-entrapped pores (GEPs), and keyholes (KHs). All specimens have been stress relieved (SR) and surface machined to alleviate thermal residual stresses and mitigate the effects of surface notches. Fatigue testing is performed under tension-tension loading and the fracture surfaces have been examined under a scanning electron microscope (SEM) to quantify the critical crack initiating defect features. The defect feature information has been correlated to the fatigue properties to gain an understanding of the micro-/defect structure-fatigue relationships for Al alloys.

3.2. Methodology

Cylindrical AlSi10Mg and Scalmalloy bars, 7 mm in diameter and 75 mm in length, were fabricated on a Renishaw RenAM500Q quad laser L-PBF system. Different sets of bars were fabricated by varying the process parameters from the manufacturer recommended/baseline parameters to induce commonly found defects in AM, i.e., LoFs, GEPs, and KHs. The quad laser strategy was implemented which yielded lower porosity than single laser consolidation, according to the authors' preliminary analysis. For AlSi10Mg, the Renishaw recommended process parameters were used as the baseline and the scan speed and laser power adjusted to vary the volumetric energy. Since manufacturer recommended process parameters were not available for Scalmalloy, the baseline process parameters were adopted from literature and the laser power and scan speed again varied to induce various types of defects in the different specimen sets [30].

The specimens produced with energy inputs lower than the baseline process parameters were intended to induce LoFs resulting from insufficient penetration of the melt pools into the previous layers. On the other hand, specimens produced using energy inputs greater than the baseline process parameters were intended to induce KHs which form due to vapor recoiling effects [100,101]. The process parameters used for each specimen set are reported in **Table 5**, where the first letter of the designation is for the volumetric energy input relative to the baseline parameter sets (B for baseline, U for underheated and O for overheated) and the second letter is for the part orientation during fabrication, relative to the build direction (V for vertical, D for diagonal and H for horizontal). The numerical suffix (e.g., OV1, OV2) distinguishes specimens fabricated using different overheated parameter sets.

Table 5. Process parameters for various sets of L-PBF AlSi10Mg and Scalmalloy specimens (baseline (B), underheated (U) and overheated (O)) fabricated in the vertical (V), diagonal (D) and horizontal (H) orientations.

Material	Process parameter set	Laser power (W)	Scan speed (mm/s)	Layer thickness (μm)	Hatch distance (μm)
AlSi10Mg	Baseline Vertical (BV)	350	1800	30	90
	Underheated Vertical (UV)	350	1980	30	90
	Underheated Diagonal (UD)	350	1980	30	90
	Underheated Horizontal (UH)	350	1980	30	90
	Overheated1 Vertical (OV1)	385	1800	30	90
	Overheated2 Vertical (OV2)	420	1440	30	90
Scalmalloy	Baseline Vertical (BV)	350	1100	30	90
	Underheated Vertical (UV)	370	1200	30	90
	Underheated Diagonal (UD)	370	1200	30	90

Underheated Horizontal (UH)	370	1200	30	90
Overheated Vertical (OV)	370	1000	30	90

Three different build layouts were employed (**Figure 13**(a)-(c)) with each one consisting of specimens fabricated in a different orientation; i.e., vertical (90°), diagonal (45°), and horizontal (0°). The vertical build consisted of bars fabricated using all process parameter sets, i.e., baseline, underheated, and overheated parameters as listed in **Table 5**. To fabricate the diagonally and horizontally oriented specimens, only the underheated process parameters were utilized. The LoFs, which tend to form in underheated conditions, are known to be larger in the plane perpendicular to the build direction and should exhibit different fatigue criticality depending on their orientation in relation to the specimen's major axis (i.e., loading direction). This work quantified defects' criticality using Murakami's $\sqrt{area}$ parameter, i.e., their square root of projected area on the loading plane, which is a commonly employed approach [91].

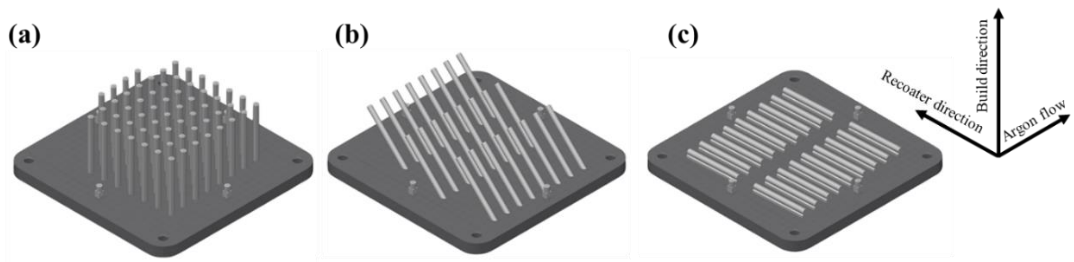

Figure 13. Build layouts for the (a) vertically (V), (b) diagonally (D), and (c) horizontally (H) fabricated AlSi10Mg and Scalmalloy round bars on the RenAM500Q L-PBF system.

Post-fabrication, the bars were removed from the build plate and post-processed. The AlSi10Mg bars underwent stress-relief heat treatment at 285°C for 2h followed by air cooling according to ASTM F3301 [102]. The Scalmalloy bars were stress-relieved at 325°C for 4h followed by air cooling [30,40]. The heat treated rods of both alloys were then machined to the fatigue specimen geometry with a gage diameter of 3 mm, gage length of 3 mm, and a blended fillet radius of 30 mm, as presented in **Figure 14**. This smaller gage diameter and shorter gage length were chosen to enable high resolution x-ray computed tomography (XCT) scanning of the specimens, allowing for a thorough examination of the entire gage section's internal porosity. All machined specimens were further longitudinally polished using reducing grits of sandpapers to achieve a surface roughness, R_a, of 0.2 µm or less prior to fatigue testing.

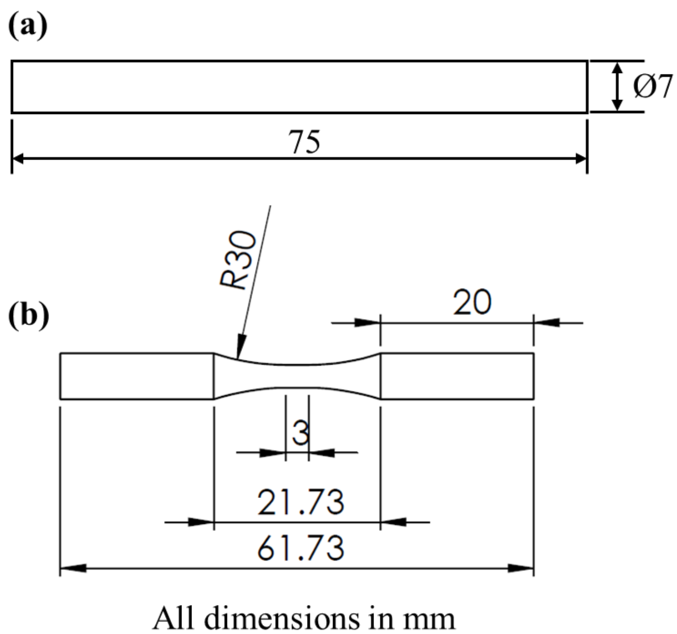

Figure 14. (a) As fabricated round bar and (b) post-machining fatigue specimen geometries.

Uniaxial force-controlled fatigue tests were performed following guidelines from ASTM E466 at a stress ratio of $R_\sigma = (\frac{\sigma_{min}}{\sigma_{max}}) = 0.1$ [40]. It should be noted that although the specimen geometry did not follow standard guidelines since they were designed to enable high resolution XCT scanning, the testing protocols were in accordance with ASTM E466. The maximum stresses were varied from 100 to 160 MPa for the AlSi10Mg tests and from 200 to 300 MPa for the Scalmalloy tests. A sinusoidal waveform was applied at a frequency of 10 Hz, and at least 3 tests were performed per stress level, except when the fatigue limit was reached for a particular specimen condition, in which case at least two tests were performed up to runout designated cycle.

The tests were concluded either upon fracture or if they met the runout criterion which was set at 5,000,000 cycles in this study. In the case of runout tests, step-tests were performed after reaching runout at higher stress levels to fracture the specimens which allowed the $\sqrt{area}$ of the critical defects to be measured.

The fracture surfaces for all specimens were examined using a Zeiss CrossBeam 550 SEM to characterize the critical defects at the fatigue fracture origins. In addition, the microstructures for the different sets of specimens were analyzed through electron backscatter diffraction (EBSD). The microstructural samples were excised from the SR bars and sectioned along the longitudinal plane (i.e., plane parallel to the specimen major axis). The samples were mounted in epoxy resin and prepared following ASTM E3 [41], which includes grinding and polishing the sample surface to a mirror finish. The porosity content in the specimens was assessed using a Zeiss Xradia Versa 620 XCT system. A voxel size of 5.4 μm was used to image the reduced gage section of the fatigue specimens.

3.3. Results

3.3.1. Microstructure

The inverse pole figure (IPF) maps obtained from EBSD analysis of both L-PBF AlSi10Mg and Scalmalloy in various conditions are presented in **Figure 15**. The EBSD analysis was performed on the longitudinal cross section of the specimens (i.e., on the plane parallel to the specimens' major axis and loading direction). The step sizes were set as 0.45 μm for AlSi10Mg and 0.23 μm for Scalmalloy. The mean grain sizes were also reported for each of the conditions measured as the equivalent circle diameters. The average grain size was measured as 2.9, 3.8, 3.9, 3.2 and 3.5 μm for the OV, BV, UV, UD and UH AlSi10Mg specimens, respectively (**Figure 15**(a)-(e)). This indicated there were no significant differences in the grain sizes despite the different energy inputs used during fabrication of the specimens.

The average grain sizes for Scalmalloy were measured as 1.6, 1.5, 1.4, 1.3 and 1.3 μm for the OV, BV, UV, UD and UH Scalmalloy specimens (**Figure 15**(f)-(j)). Although the average grain sizes were comparable, a characteristic bimodal structure was observed in all conditions consisting of FG and CG regions [103]. The FG regions were primarily located along the melt pool boundaries, while the CG regions were found in the interiors. It is important to acknowledge that the actual average grain size of Scalmalloy would be smaller than what is reported in this analysis since there are nano-sized grains in the melt pool regions which could not be indexed (see the black regions in between melt pools in **Figure 15**(f)-(j)) [104]. In the vertical specimens, the columnar grains appeared to be along the specimens' major axis whereas in the diagonal and horizontal specimens, their orientation was ~45° and ~90° with respect to the specimens' major axes (i.e., loading direction).

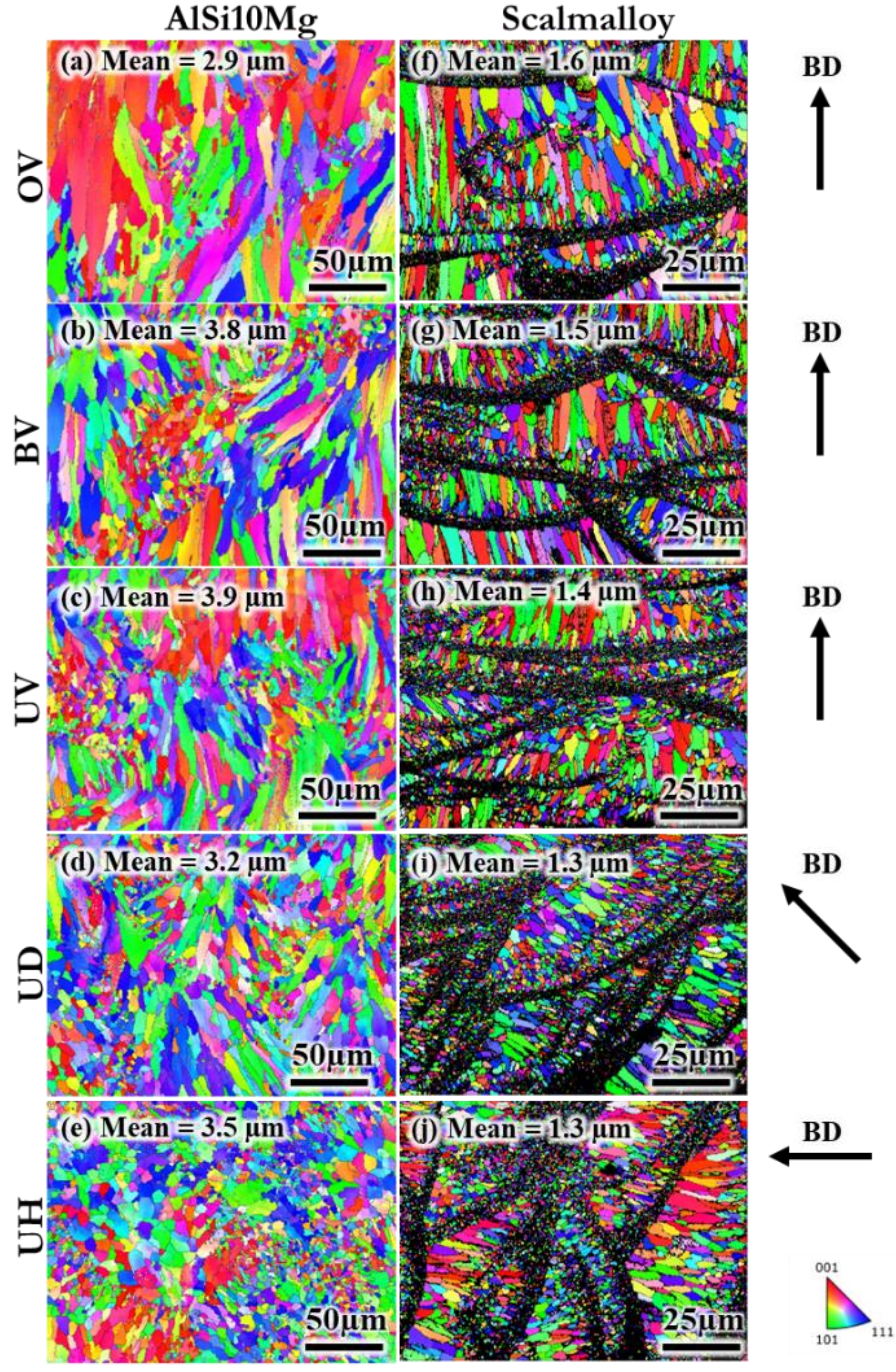

Figure 15. IPF maps of (a)-(e) AlSi10Mg and (f)-(j) Scalmalloy microstructural samples in various conditions. The build direction (BD) relative to the part orientation is also indicated for each condition.

3.3.2. Porosity analysis

The defect content obtained via XCT analysis of the AlSi10Mg and Scalmalloy specimens in various conditions is presented in **Figure 16**. All defect size measurements were performed using Murakami's $\sqrt{area}$ parameter which considered the projection of the defect on the plane perpendicular to the specimens' loading axis/major axis. The OV condition showed the highest relative density of 99.98% for AlSi10Mg compared to all other conditions. With a decrease in energy input, the relative density was observed to worsen. The BV condition (fabricated with manufacturer recommended process parameters) had a comparable relative density of 99.93% to the UV, UD, and UH (underheated) conditions which had relative densities of 99.94, 99.93, and 99.95%, respectively. It should be noted that while the BV condition had slightly lower relative density than the UV condition in the representative specimen presented in **Figure 16**, the relative densities were comparable on average. Furthermore, the defect size distributions showed that the 90th percentile $\sqrt{area}$, measured as 28 μm, was smaller for the OV specimens compared to all other conditions. The BV and UV conditions both contained larger defects and had their 90th percentile $\sqrt{area}$ measured as 40 and 42 μm, respectively. The part orientation also appeared to have influenced the projected $\sqrt{area}$ measurements, with UH specimens showing the smallest projected $\sqrt{area}$ compared to the diagonal and vertical underheated specimens.

The Scalmalloy specimens exhibited similar relative densities of ~99.97% for all conditions, as seen in **Figure 16**(b). However, the defect size distributions were vastly different for the various conditions. The 90th percentile $\sqrt{area}$ was measured to be the largest in the OV specimens compared to all other conditions. Interestingly, decreasing energy input resulted in the opposite trend as compared to AlSi10Mg, and the 90th percentile $\sqrt{area}$ was observed to decrease in the BV, UV, UD and UH condition for Scalmalloy. It should be noted that the BV (baseline) parameters used in this study for fabrication were adopted from literature, since manufacturer recommended baseline parameters were not available for Scalmalloy. In addition, smaller adjustments were made in laser power and scan speed for the underheated and overheated conditions for Scalmalloy due to its narrower processing window for achieving near fully dense parts [103,105]. Nevertheless, the chosen parameters appeared to have induced the desired defect types in each condition. The OV specimens contained large, near-spherical KHs throughout the bulk of the specimen as can be observed in **Figure 16**(b). The BV and UV specimens contained large LoFs with their major axis being perpendicular to the specimens' major axis. The UD and UH specimens also had large LoFs, with planarity along the layer directions which were oriented at ~45° and 0° relative to the specimens' axis.

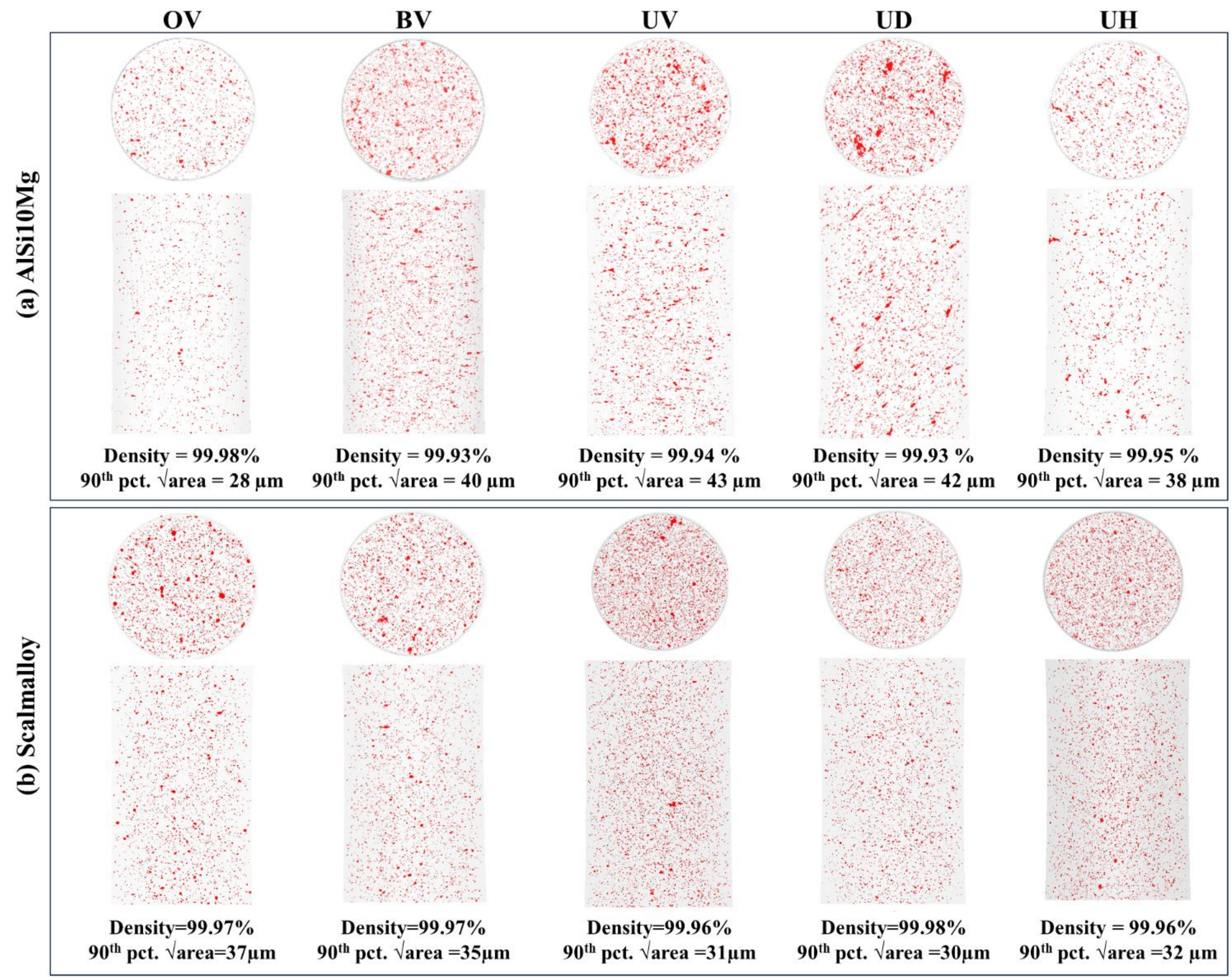

Figure 16. Visualization of defect structures in representative specimens at the gage sections obtained from XCT. The relative density and 90th percentile $\sqrt{area}$ are also reported for each condition.

3.3.3. Fatigue behavior

A summary of the stress-life fatigue results for the various conditions of AlSi10Mg and Scalmalloy is provided in **Table 6,** along with the corresponding crack initiating defect $\sqrt{area}$, type and location. In addition, the stress-life fatigue plots for L-PBF AlSi10Mg and Scalmalloy are presented in **Figure 17**(a) and (b), respectively, with the runout tests indicated with arrows. As seen in **Figure 17** (a), there is a large amount of scatter in the stress-life data for all AlSi10Mg conditions at all stress levels. The UV and BV specimens exhibited the most inferior fatigue performance, with consistently shorter lives at all stress levels compared to the other conditions. The OV, UD and UH specimens appeared to exhibit slightly longer fatigue lives compared to the UV and BV conditions, with the OV2 specimens reaching their runout level at 150 MPa.

Scalmalloy exhibits pronounced scatter in the stress-life data among various conditions, as seen in **Figure 17** (b), especially at stress levels of 200, 225 and 250 MPa. In addition, some runouts were recorded for all conditions at stress levels of 200 and 225 MPa, with the UV condition reaching its fatigue limit at 200 MPa. Due to the notable overlap in the datapoints among various sets of specimens, no clear trend was observed for any one condition outperforming the others.

Table 6. Force-control fatigue data for L-PBF AlSi10Mg and Scalmalloy specimens tested under uniaxial tension-tension loading at R_σ = 0.1 along with the information of the crack-initiating defects.

Material	**Condition**	**Spec. ID**	σ_{max} **(MPa)**	$2N_f$	$\sqrt{area}$ **(µm)**	**Location/type**
AlSi10Mg	UV	V11L	160	144,172	303	Surface/LoF
		V10L	160	199,546	182	Surface/LoF
		V09L	160	246,066	115	Surface/LoF
		V06L	150	257,650	208	Surface/LoF
		V01L	150	270,756	194	Surface/LoF
		V08L	150	308,130	192	Surface /LoF
		V02L	125	546,850	165	Surface /LoF
		V13L	125	650,144	191	Surface /LoF
		V03L	125	795,334	139	Surface /LoF
		V12L	100	1,770,358	197	Surface/LoF
		V05L	100	5,486,382	149	Surface /LoF
		V15L	100	5,553,716	214	Surface /LoF
	UD	D13	160	272,190	143	Surface/LoF
		D05	160	637,830	110	Surface/LoF
		D14	160	658,144	101	Surface/LoF
		D11	150	342,256	181	Surface/LoF
		D17	150	520,584	86	Surface/LoF
		D15	150	540,384	140	Surface/LoF
		D12	125	1,486,532	99	Surface/LoF
		D10	125	2,918,794	96	Surface/LoF
		D02	125	6,988,200	74	Surface/LoF
	UH	H10	160	681,564	118	Surface/LoF
		H06	160	1,113,170	75	Surface/LoF
		H08	160	4,167,756	92	Near surface/LoF
		H18	150	5,144,876	41	Near surface/LoF

		H07	150	10,000,000	-	-
		H09	150	10,000,000	32	-
		H17	125	10,000,000	31	-
	BV	V28G	160	238,574	148	Surface/LoF
		V19G	160	260,522	192	Surface/LoF
		V23G	160	309,332	98	Surface/LoF
		V21G	150	267,202	175	Surface /LoF
		V22G	150	444,348	107	Near surface/LoF
		V26G	150	455,898	119	Surface/LoF
		V20G	125	635,008	136	Surface/LoF
		V30G	125	656,276	144	Surface/LoF
		V25G	125	677,152	147	Surface/LoF
		V29G	100	2,097,348	160	Surface/LoF
		V17G	100	5,531,760	134	Surface/LoF
		V24G	100	10,000,000	-	-
	OV1	V33E	160	611,768	79	Near surface/LoF
		V42E	160	1,001,376	49	Surface/LoF
		V41E	150	405,196	128	Surface/LoF
		V37E	150	423,102	116	Near surface/LoF
		V32E	125	3,972,230	77	Surface/LoF
		V40E	125	10,000,000	-	
	OV2	V47K	160	474,606	44	Surface/LoF
		V53K	160	2,564,296	121	Surface/KH
		V56K	160	10,000,000	-	-
		V48K	150	10,000,000	-	-
		V51K	150	10,000,000	-	-
		V55K	150	10,000,000	-	-
		V58K	150	10,000,000	-	-
		V46K	125	10,000,000	-	-
Scalmalloy	UV	LV04	300	41,250	63	Surface/LoF
		LV02	300	55,912	54	Surface/LoF
		LV06	300	82,114	30	Surface/microstructural
		LV12	250	80,946	63	Surface/LoF
		LV13	250	153,220	27	Surface/LoF
		LV11	250	157,610	48	Surface/LoF
		LV05	225	120,254	40	Surface/pore
		LV01	225	176,162	60	Surface/LoF
		LV09	225	226,664	40	Surface/LoF
		LV10	200	184,698	47	Surface/LoF
		LV08	200	499,180	42	Surface/microstructural
		LV07	200	10,000,000	42	-
	UD	D05	300	53,966	74	Surface/LoF
		D06	300	63,088	44	Surface/LoF
		D13	300	70,526	71	Surface/LoF
		D01	250	149,144	33	Surface/microstructural
		D07	250	1,066,396	31	Surface/microstructural
		D04	250	1,315,078	30	Surface/microstructural
		D09	225	156,760	56	Surface/LoF
		D02	225	193,650	52	Surface/LoF

		D11	225	10,000,000	31	-
		D03	200	418,932	55	Surface/LoF
		D08	200	10,000,000	38	-
		D12	200	10,000,000	54	-
	UH	H04	300	46,004	40	Surface/microstructural
		H06	300	65,466	46	Near surface/GEP
		H12	300	121,926	28	Surface/LoF
		H09	250	98,858	46	Near surface/LoF
		H05	250	115,608	56	Surface/LoF
		H11	250	635,428	27	Near surface/GEP
		H01	225	228,484	42	Near surface/LoF
		H13	225	10,000,000	39	-
		H02	200	10,000,000	63	-
		H10	200	10,000,000	45	-
	BV	GV03	300	46,352	62	Surface/LoF
		GV06	300	52,076	51	Surface/LoF
		GV02	300	53,012	47	Surface/LoF
		GV09	250	67,746	68	Surface/LoF
		GV08	250	75,786	70	Surface/LoF
		GV13	250	88,334	84	Surface/LoF
		GV05	225	112,250	54	Surface/LoF
		GV11	225	148,476	48	Surface/LoF
		GV04	225	4,440,848	37	Surface/LoF*
		GV10	200	178,934	54	Surface/LoF
		GV12	200	238,012	62	Surface/LoF
		GV07	200	10,000,000	50	-
	OV	KV13	300	61,810	60	Surface/KH
		KV03	300	74,180	56	Surface/LoF
		KV08	300	106,608	37	Surface/microstructural
		KV07	250	139,890	70	Surface/LoF
		KV01	250	156,824	37	Surface/microstructural
		KV05	250	249,808	36	Surface/KH
		KV09	225	102,156	90	Surface/LoF
		KV12	225	662,138	44	Surface/LoF
		KV10	225	10,000,000	64	-
		KV02	200	361,898	82	Surface/LoF
		KV06	200	597,940	92	Surface/KH
		KV11	200	10,000,000	51	-

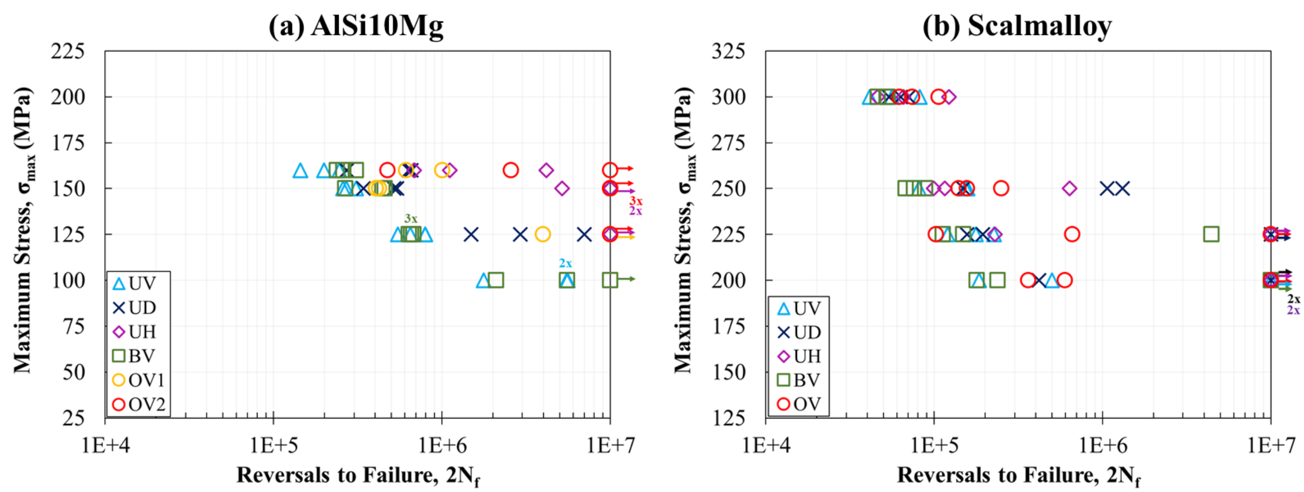

Figure 17. The stress-life fatigue plots for (a) AlSi10Mg and (b) Scalmalloy specimens tested under uniaxial tension-tension loading at R_σ = 0.1.

3.3.4. Fatigue fractography

A selection of fatigue fracture surfaces for AlSi10Mg specimens in various conditions, tested at a stress level of σ_{max} = 160 MPa, are presented in **Figure 18** as examples of the different crack initiating defect types. It should be noted that the fracture surfaces were analyzed for all specimens and the critical defect $\sqrt{area}$, type, and location for each specimen is listed in **Table 6**. The critical defect sizes were measured from the fracture surfaces using Murakami's $\sqrt{area}$ parameter [91]. Near surface/surface exposed defect sizes were measured by constructing the convex hull of the defects and connecting to the surface if their $\sqrt{area}$ was larger than the distance to the surface. Additionally, if the distances between two adjacent defects were smaller than the $\sqrt{area}$ of the smaller defect, the square root of the convex hull enveloping both defects was considered as the effective $\sqrt{area}$.

In all AlSi10Mg specimens, fatigue cracks were observed to initiate at surface exposed/near surface volumetric defects as shown in the magnified images of the initiation zone. For conditions UV, BV, UD and UH, fatigue cracks always initiated from large surface exposed/near surface LoFs, as seen in **Figure 18**(a)-(d). For OV1 and OV2 specimens, while some specimens had crack initiations from KHs (**Figure 18**(f)), the majority of specimens had large fatigue critical LoFs close to the surface at the fracture origin. This was interesting because the preliminary XCT analysis revealed that the overheated conditions were able to induce near-spherical KHs throughout the bulk of the specimens and, despite their presence, in certain specimens (**Figure 18**(e)) surface exposed LoFs were more critical and the preferential sites for fatigue damage.

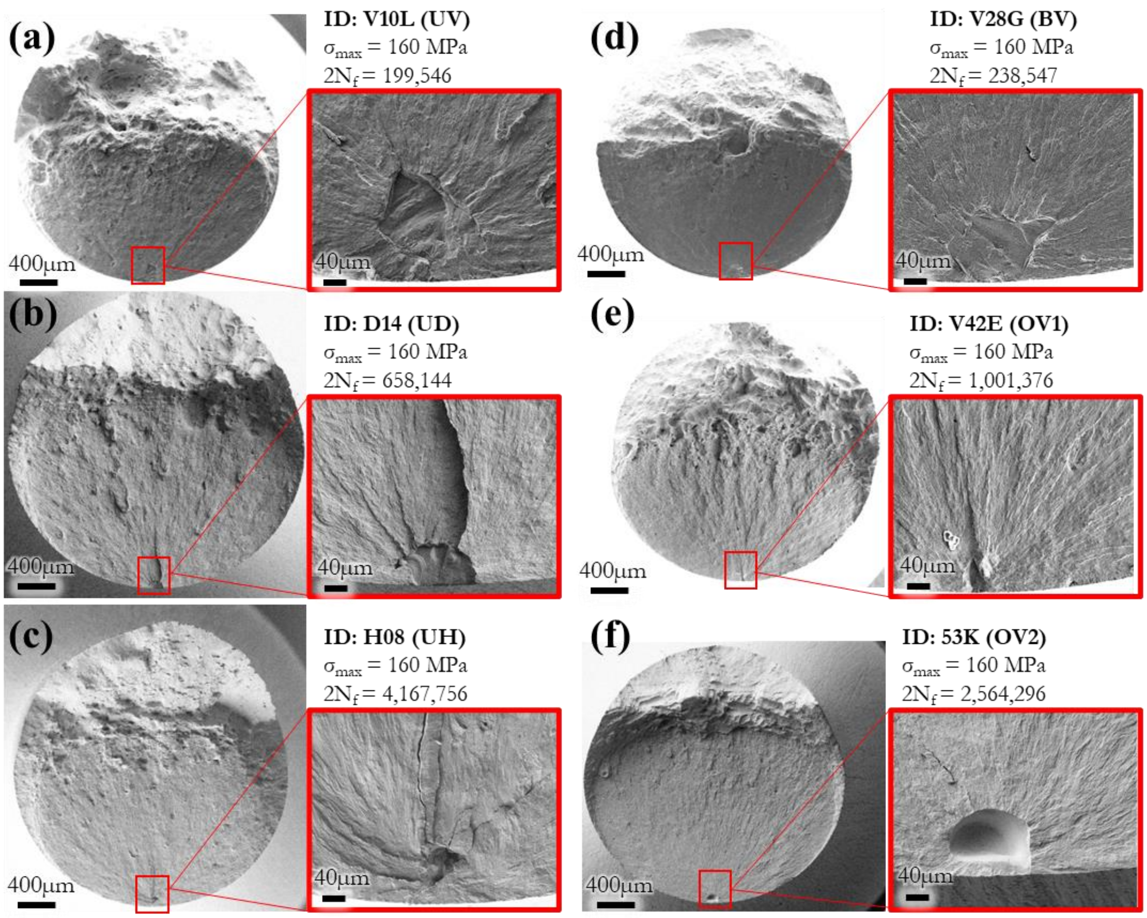

Figure 18. Examples of fatigue fracture surfaces for L-PBF AlSi10Mg specimens tested at σ_{max} = 160 MPa.

A selection of fatigue fracture surfaces for L-PBF Scalmalloy specimens tested at σ_{max} = 250 MPa are presented in **Figure 19** as examples of different crack initiating features present. In all Scalmalloy specimens, fatigue cracks always initiated from either surface exposed/near surface defects or from near surface fine grained regions. The initiating features included defects such as LoFs (**Figure 19**(a), (d)), microstructural inhomogeneities/oxide particles (**Figure 19**(b)), GEPs/KHs (**Figure 19**(c), (e)), or fine grained regions (**Figure 19**(f)). While altering the processing parameters and energy input was able to induce large LoFs in the underheated conditions and KHs in the overheated conditions (**Figure 16**(b)), the critical features were not always the most common defect types present in those specimens. Thus, the criticality of the crack initiating features appeared to depend on their type, size, morphology, surrounding microstructure and proximity to the surface rather than on the most abundant defect type. More of this is discussed in the Discussion section.

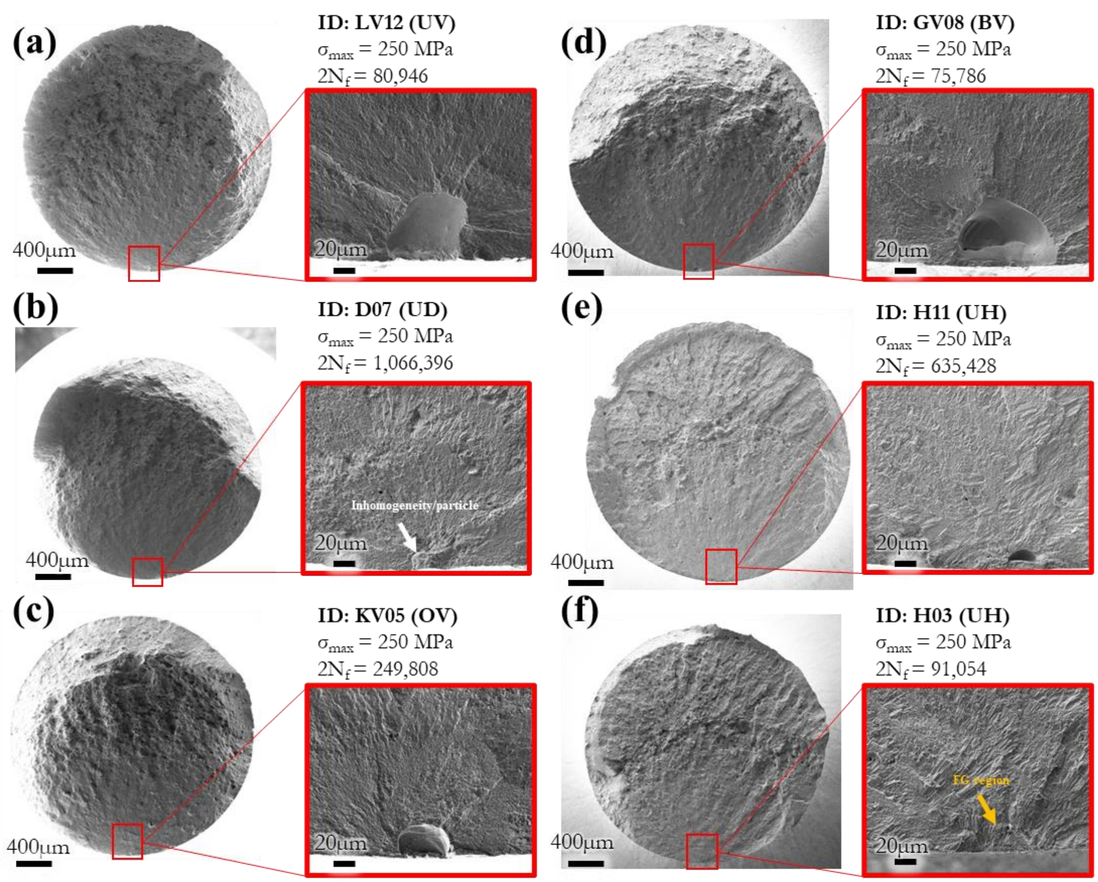

Figure 19. Examples of fatigue fracture surfaces for L-PBF Scalmalloy tested at σ_{max} = 250 MPa.

Statistical analysis was performed to obtain the critical defect size distributions for AlSi10Mg and Scalmalloy in various conditions [106,107]. The analysis was performed using the critical feature sizes for the fractured specimens and the runout specimens which were step tested at a higher stress level to reveal the critical features. Following Gumbel extreme value statistical approach, the reduced variate, Y_i, has been calculated using the non-parametric moments method as:

$$F_i = \frac{i}{n+1}, \qquad (3.1)$$

$$Y_i = -\ln\left(-\ln(F)\right), \quad (3.2)$$

where F_i is the cumulative probability of the i^{th} defect ranked in ascending order and n is the total number of fatigue critical defects identified per condition. The crack initiating feature size distributions are presented in **Figure 20**(a) and (b) for AlSi10Mg and Scalmalloy, respectively.

As seen in **Figure 20**(a), the UV, BV, and to some extent, UD specimens had the largest crack initiating features in the AlSi10Mg dataset. These specimens also had the shortest fatigue lives with the critical defects situated near/at the surface of the specimens. In contrast, the distributions for the OV1, OV2 and UH were left-shifted and these conditions had slightly longer fatigue lives at all stress levels. The crack initiating feature size distributions for Scalmalloy in **Figure 20**(b) did not show such marked differences between the different conditions. This was also reflected in the stress-life data presented earlier, where no clear distinction could be made between the underheated condition, including the different orientations, baseline and overheated conditions. Instead, the strong correlation between crack initiating feature size distribution and fatigue lives appeared to exist in the high cycle fatigue regime of the L-PBF aluminum alloys investigated in this study.

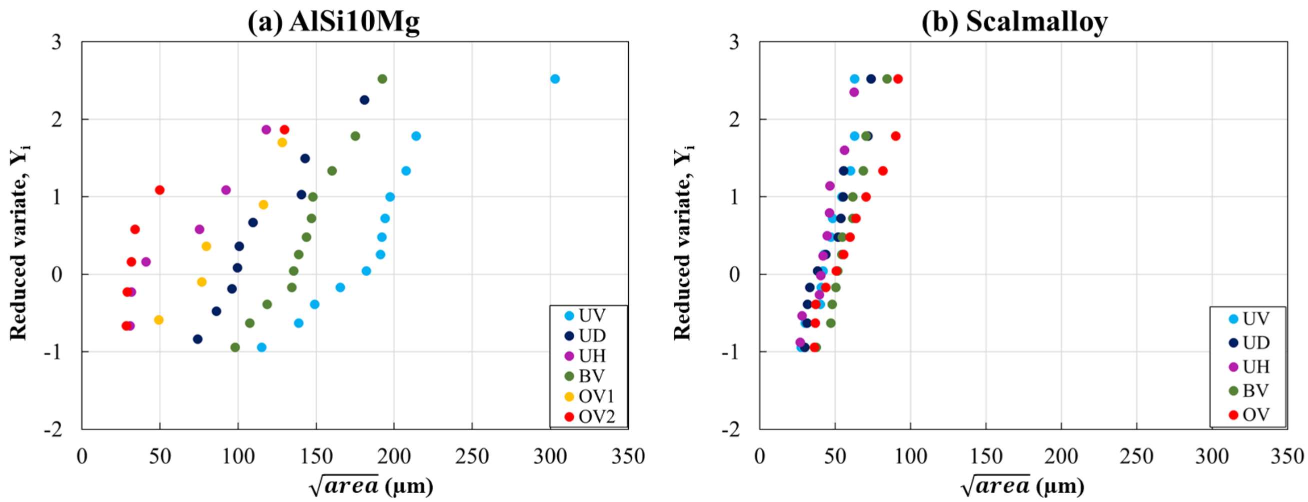

Figure 20. Gumbel reduced variate versus critical crack initiating feature $\sqrt{area}$ for (a) AlSi10Mg and (b) Scalmalloy specimens.

3.4. Discussion

3.4.1. Examining the correlation between crack initiating features and fatigue life

To further understand the effects of volumetric defects on the fatigue behavior, particularly considering the large scatter observed in the stress-life data for both AlSi10Mg and Scalmalloy, the defect features (such as size and, to some extent, location) are incorporated into the stress-life plots using the normalized stress which is plotted against the cycles to failure in **Figure 21**(a) and (b), following Murakami et al [91]. The ordinate in these plots is the stress range divided by the fatigue limit, where the $\frac{\Delta\sigma}{\Delta\sigma_w}$ parameter represents the crack driving force, i.e., the threshold stress for non-propagating cracks to grow [108]. The fatigue limit, $\Delta\sigma_w$, can be obtained using the El-Haddad equation as:

$$\Delta\sigma_w = \Delta\sigma_{w0} \cdot \sqrt{\frac{\sqrt{area_0}}{\sqrt{area_0}+\sqrt{area}}}, \quad (3.3)$$

where $\Delta\sigma_{w0}$ is the fatigue limit for a defect-free material; and $\sqrt{area_0}$ is calculated as:

$$\sqrt{area_0} = \frac{1}{\pi} \cdot \left(\frac{\Delta K_{th}}{Y \cdot \Delta\sigma_{w0}}\right)^2, \quad (3.4)$$

where ΔK_{th} is the threshold stress intensity factor (SIF) range at a given stress ratio and Y is the Murakami location factor, taken as 0.65 for surface defects and 0.5 for internal defects. The threshold SIF was obtained from the works of Beretta et.al. and Pergham et.al as $\Delta K_{th,R=0.1}$ = 1.3 MPa/√m for AlSi10Mg and $\Delta K_{th,R=0.1}$ = 1.5 MPa/√m for Scalmalloy [109,110]. The defect-free fatigue strength for AlSi10Mg was obtained from the works of Wu et.al which was $\Delta\sigma_{w0}$ = 188 MPa [99]. For Scalmalloy, and the defect-free fatigue strength was obtained from Schimback et al. and was set as $\Delta\sigma_{w0}$ = 360 MPa [105,111].

The normalized stress-life data for AlSi10Mg in **Figure 21**(a) showed a significant reduction in scatter compared to what was seen in the stress-life behavior reported earlier in **Figure 17**. The specimen with the shortest fatigue life was a UV specimen tested at a nominal normalized stress range which was ~2.3 times larger than its calculated fatigue limit stress range, based on the critical defect size present in the specimen. On the other hand, as the normalized stress values approached 1, the curve flattened asymptotically, indicating that the specimens' fatigue limit was being approached, which varied on a specimen-by-specimen basis depending on the defect content.

The normalized stress-life data for Scalmalloy is presented in **Figure 21**(b). Overall, the normalized stress-life data followed a similar trend to AlSi10Mg, with $\frac{\Delta\sigma}{\Delta\sigma_w}$ values decreasing for specimens with longer lives and the curve flattening asymptotically when approaching 1. However, despite an appreciable improvement in the normalized stress-life behavior compared to the stress-life data in **Figure 17** (b), there was still some scatter noticed. This indicated that although the fatigue lives were generally correlated with the fatigue limit-which accounts for the defect size and location, additional factors, such as microstructural effects, could have contributed to the scatter in Scalmalloy. Nonetheless, the correlation between the normalized stress and the fatigue lives for both AlSi10Mg and Scalmalloy, albeit slightly scattered, reinforced that the fatigue behavior of Al alloys may be best described using defect-sensitive approaches [5,112].

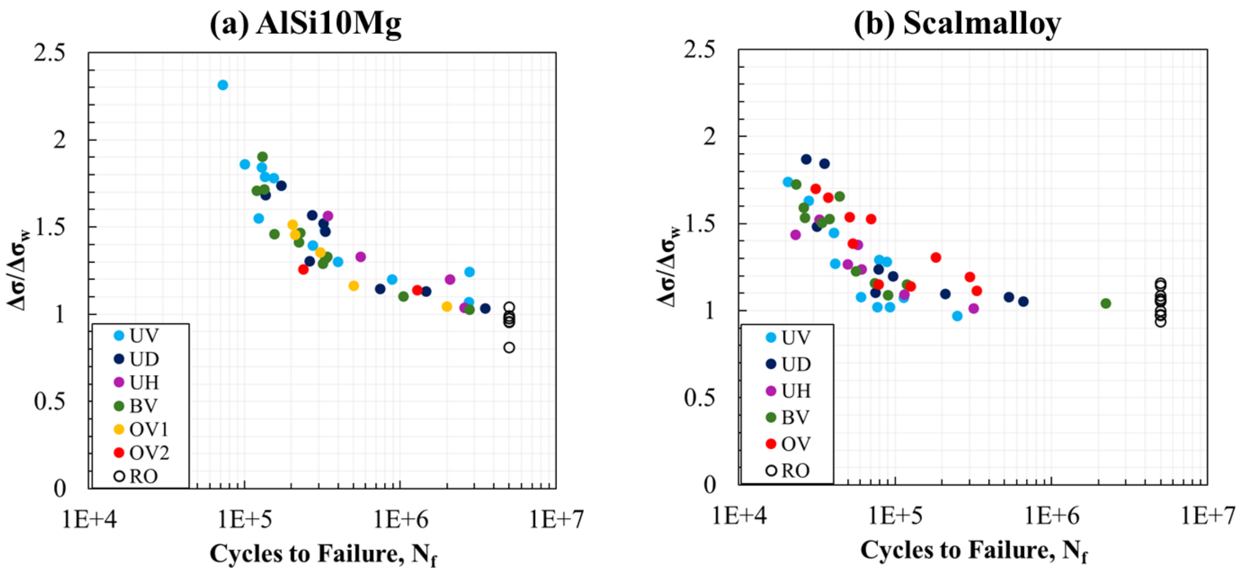

Figure 21. Normalized stress-life diagrams for (a) AlSi10Mg and (b) Scalmalloy. The step-tested runout (RO) specimens are indicated with hollow black markers.

3.4.2. Life estimation using fatigue notch factor approach

By treating volumetric defects as notches, the fatigue notch factor is often employed to estimate the fatigue lives of AM parts. In the approach, the three regimes of the stress life behavior are considered i.e., Regime I-III as shown in **Figure 22** [113,114]. The intersection between regimes I and II can be assumed to be at $2N_t = 2\times10^3$ as reported in various literature [115–117]. Regime II, which can be significantly influenced by stress concentrations, is described using Basquin's power law:

$$\sigma_a = \sigma_f' \cdot (2N_f)^b, \qquad (3.5)$$

where σ_f' and b are the fatigue strength coefficient and the fatigue strength exponent, respectively, and $2N_f$ is the reversals to failure.

The fatigue limit in Regime III can be calculated using damage tolerant models such as El-Haddad. To estimate the Regime II stress-life behavior containing volumetric defects, the stress-life curve for each specimen can be approximated by the power law function (Equation (3.5)) defined by two points: the regime I/II intersection, and the calculated fatigue limit based on the defect features [115]. An illustration of the idealized stress-life curves of defect free (green) and defective (red and purple) materials is presented in **Figure 22**.

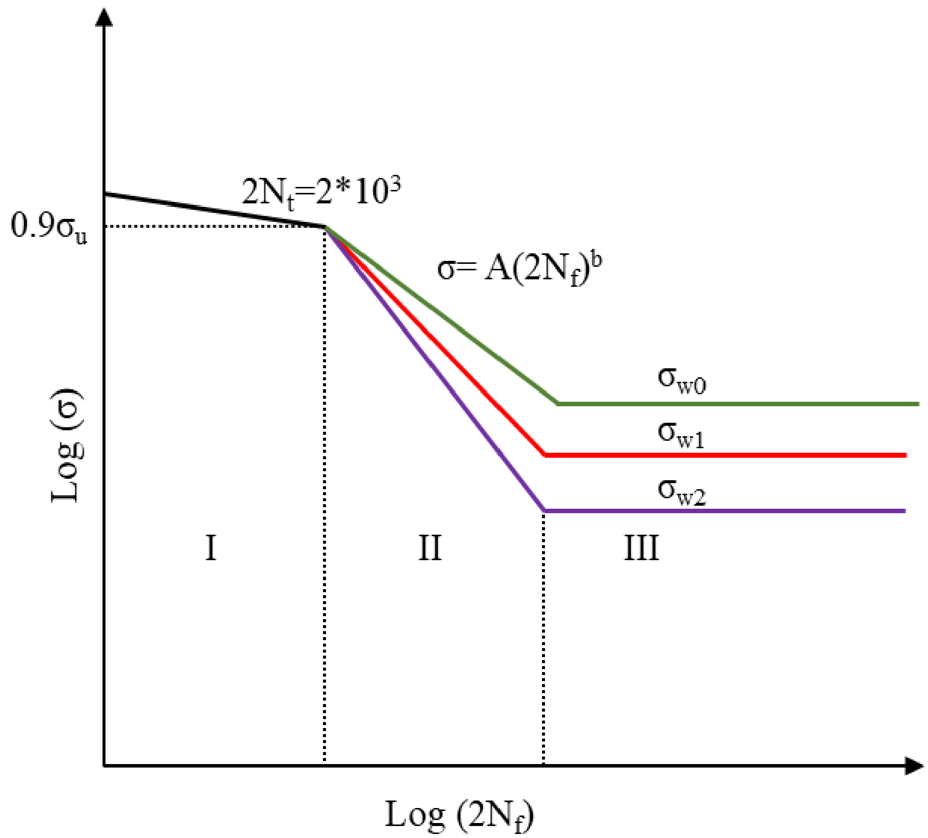

Figure 22. Idealized stress-life curves for defect free specimens and specimens containing defects of various sizes.

Considering the effect of defects, the fatigue limit of the defect-prone specimens can be determined via various damage-tolerant models. In this study, the normalized stress-life data for both AlSi10Mg and Scalmalloy (**Figure 21**), showed a reasonable correlation when using the El-Haddad model. This prompted a more detailed investigation into the suitability of the El-Haddad model in describing the fatigue limit by taking the defect size, location, and ΔK_{th} (Equation (3.4)) into consideration. The stress amplitudes are plotted against the critical defect sizes for all specimens in **Figure 23** in a Kitagawa-Takahashi diagram. Here, volumetric defects can be considered as preexisting short cracks with size equivalent to their projected $\sqrt{area}$ on the plane perpendicular to the loading axis [99]. In addition, the dashed curves in **Figure 23**(a) and (b) are the El-Haddad fatigue limit and demarcate the boundary between non-propagating crack sizes and propagating crack sizes which will grow to failure [118].

It can be observed in **Figure 23**(a) that the El-Haddad curve was able to sufficiently separate the runouts from the fractured specimens for AlSi10Mg. All fractured specimens in various conditions were accurately predicted to fail by the El-Haddad model by treating volumetric defects as short cracks to predict the stress range for non-propagating cracks to become propagating. In addition, the El-Haddad model was able to reasonably predict the runout specimens [118,119]. For Scalmalloy, while most of the specimens were accurately characterized by the El-Haddad curve, there were some runout specimens which were predicted to fracture. Conversely, some of the fractured specimens, with smaller $\sqrt{area}$, were mischaracterized at the lower stress levels. The considerable overlap between the runout and fractured datapoints at the lower stress levels prevented the El-Haddad model from being able to effectively distinguish between the two groups [119–121].

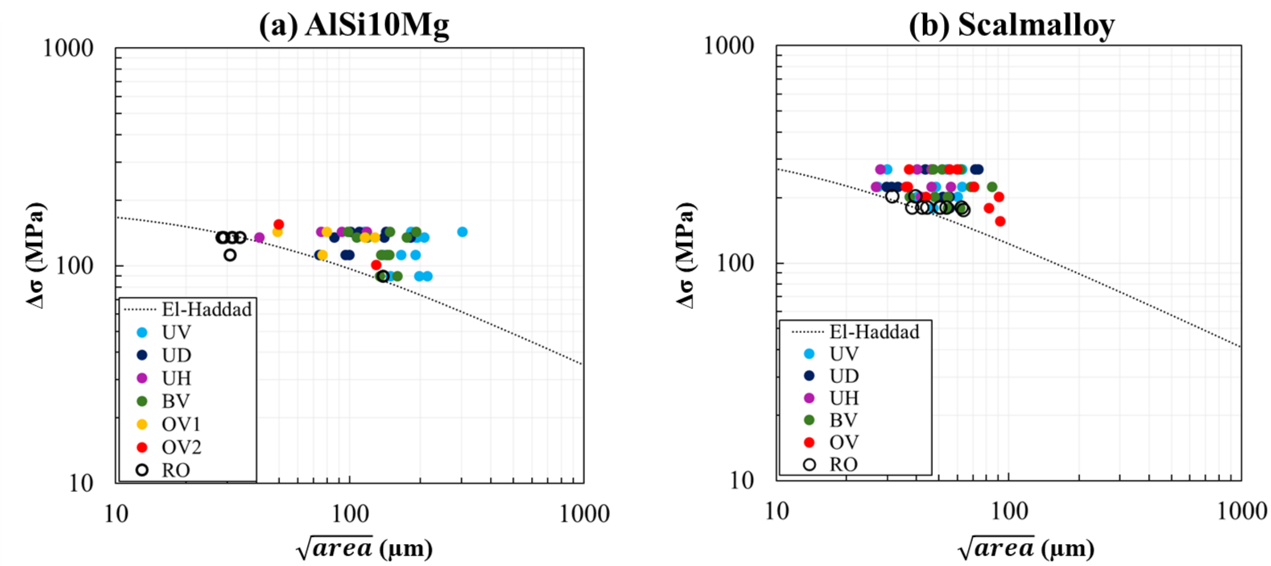

Figure 23. Stress range-$\sqrt{area}$ data plotted on a Kitagawa-Takahashi diagram for (a) AlSi10Mg and (b) Scalmalloy. The dashed curve represents the El-Haddad model for determination of the fatigue limit. The step-tested run-out (RO) specimens are indicated with hollow black markers.

Using the fatigue limit from El-Haddad equation in the fatigue notch-factor based approach, the predicted reversals to failure are plotted against the experimental reversals to failure in **Figure 24**(a) and (b) for AlSi10Mg and Scalmalloy, respectively. The predicted reversals to failure were in good agreement with the experimental reversals for AlSi10Mg (**Figure 24**(a)). Most of the data fell within a scatter band of ±3, with only a few datapoints being outside the prediction bands. In addition, the prediction were conservative, and therefore, desirable. In contrast, a significant portion of the predictions for Scalmalloy specimens fell outside of scatter bands of ±3, with most of the specimens having non-conservative predictions, as seen in **Figure 24**(b). This indicated that the fatigue lives of Scalmalloy specimens were not purely dependent on the defect characteristics according to Equations 3.3 and 3.4 with the chosen material parameters [122,123]. In fact, the experimental data suggested that the actual fatigue limit should perhaps be significantly lower for specimens with non-conservative predictions than what was calculated using the measured defect $\sqrt{area}$ from the fracture surfaces.

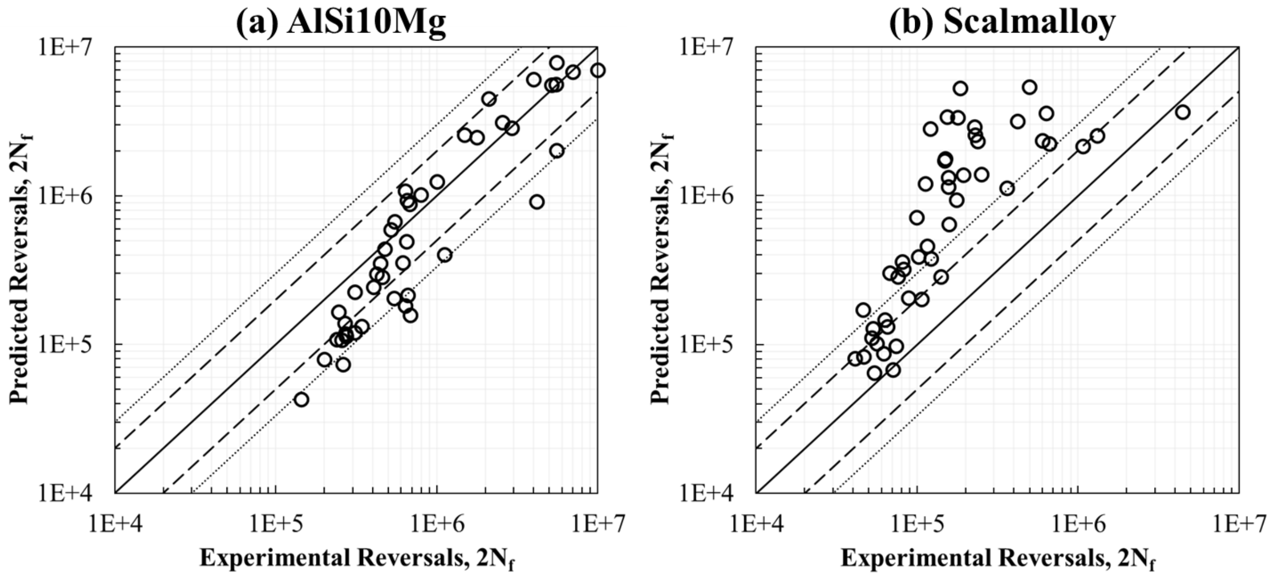

Figure 24. Fatigue life predictions based on fatigue notch factor approach for (a) AlSi10Mg and (b) Scalmalloy.

The fracture surfaces for both AlSi10Mg and Scalmalloy were examined further to understand the discrepancies in fatigue life predictions for AlSi10Mg and Scalmalloy (**Figure 24**) using the fatigue notch factor. These differences were consistent with the scatter observed in the normalized fatigue strengths for Scalmalloy (**Figure 21**(b)) which could have been stemmed from the overlap in the critical defect sizes of runout and fracture data (**Figure 23**(b)). The AlSi10Mg specimens had large near surface/surface-exposed critical defects for which the contours could be clearly recognized and allowed for consistent size measurements using Murakami's approach (**Figure 25**(a)-(c)). Furthermore, the clear visibility of river marks tracing to the defects allowed for the projected area of the defect to be traced and the initial defect size to be determined [124].

For Scalmalloy, while some of the specimens failed from volumetric defects with well-defined features, the crack initiating defects were not always clear on the fracture surfaces, as shown in **Figure 25**(d)-(f). In particular, there was ambiguity for specimens with crack initiations from small defects, microstructural inhomogeneities/oxide particles and fine grained regions. In addition, the location of the critical defects relative to the bimodal microstructure appeared to have some influence on crack initiation and propagation behavior as seen in **Figure 25**(d)-(f), where the CG and FG melt pool boundary regions can be observed in the vicinity of the volumetric defects/microstructural inhomogeneities. The fatigue limit calculation, which used experimental ΔK_{th}, assumed a homogenous microstructure which may not be valid for bimodal microstructures. In FG regions, roughness-induced crack closure was minimal [125], resulting in little crack deflection and crack path tortuosity [127]. The converse was true for the CG regions. This suggested that the actual ΔK_{th} value might have been much lower than the one determined from the fatigue crack growth tests, especially when defects were located in the FG regions.

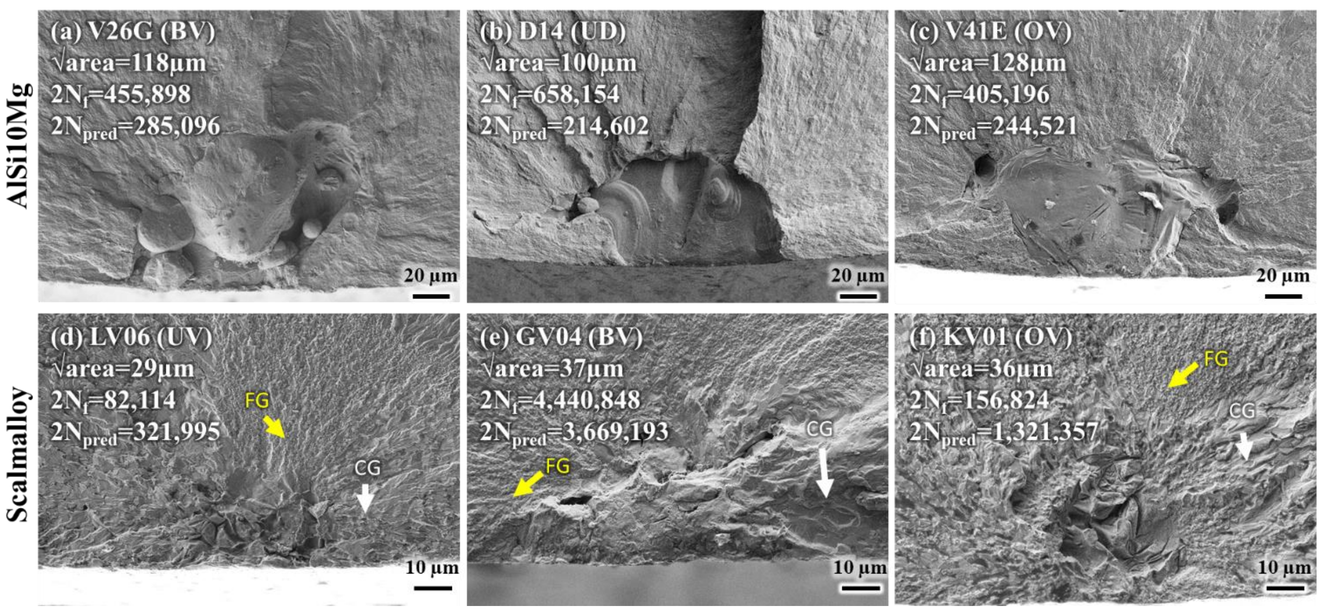

Figure 25. Fracture surfaces showing the crack initiating defects for (a)-(c) AlSi10Mg and (d)-(f) Scalmalloy.

3.4.3. Life estimation using crack growth based approach

The fatigue notch factor approach proved ineffective for fatigue life estimations of Scalmalloy due to the uncertainty in the calculation of the fatigue limit for specimens with crack initiation in fine-grained regions or from small defects. This led to exploring approaches which focus solely on crack growth behavior. The Shiozawa model, a crack growth-based approach, was therefore used to analyze the fatigue data of both L-PBF Al alloys containing volumetric defects. According to Shiozawa et al. [128,129], by integrating the Paris law, the fatigue life can be described in terms of the stress range and defect size/location by the following equation:

$$N_f = \sqrt{area} \cdot \left(\frac{\Delta\sigma \cdot Y \cdot \sqrt{\pi \cdot \sqrt{area}}}{K_f'}\right)^{-\frac{1}{d'}}, \qquad (3.6)$$

where K_f' and d' are the Shiozawa fitting parameters. For the fatigue life predictions, power curves were fit to the BV specimens for AlSi10Mg and the BV specimens for Scalmalloy (which were the recommended/baseline specimens) only to obtain the fitting parameters. It should be noted that since Shiozawa only considers the crack growth life and is not suitable in the threshold regime where some of the life may be spent in crack incubation, any datapoints exceeding $\frac{N_f}{\sqrt{area}}$ of 10^{10} cycles/m were excluded from the fitting procedures [130,131].

The Shiozawa plots in **Figure 26**(a) and (c) are generated by plotting the stress intensity factor range, ΔK, against the normalized fatigue life, $\frac{N_f}{\sqrt{area}}$, in log-log scale [132]. Interestingly, the data was observed to collapse onto the same trendline for both AlSi10Mg (**Figure 26**(a)) and Scalmalloy (**Figure 26**(c)), which had a significant amount of scatter in their stress-life behavior, as seen in **Figure 17** (a) and (b) in the earlier sections. Moreover, a plateau was observed for both materials at higher values of the normalized fatigue life, close to the fatigue limit of the materials. Such plateauing behavior clearly deviated from what could be captured by Equation 3.6 (see the dotted lines in **Figure 26**(a) and (c)), which suggested the governance of fatigue life by factors other than stable crack growth, i.e., the near threshold crack growth or crack incubation. The comparison of Shiozawa curves for the two alloys in **Figure 26**(e) revealed that despite the significantly different microstructures of AlSi10Mg and Scalmalloy, their stable crack growth behavior appeared to be similar.

The predicted fatigue lives obtained using the Shiozawa model are plotted against the experimentally measured lives in **Figure 26**(b) and (d) for AlSi10Mg and Scalmalloy, respectively. In addition, the predicted lives for both alloys are presented together for comparison in **Figure 14**(f). It can be observed that the predictions were in good agreement with the experimental lives for both alloys, with most datapoints falling within scatter bands of 3, and a significant portion being within scatter bands of 2. This can be attributed to the robustness of the model and the higher tolerance for error since the crack growth behavior is validated using experimental data. Moreover, due to the presence of large surface and near surface defects, and the defect sensitivity of the alloys, most of the fatigue lives fell in the mid cycle fatigue regime. Here, a significant portion of life was spent in crack growth that was captured by the Shiozawa model considering the stress intensity range and initial defect size. However, some of the specimens tested at the lower stress levels with longer lives had predictions falling outside scatter bands of 3. This can be ascribed to some fraction of the fatigue lives being spent in crack incubation, which was not accounted for using Shiozawa since it is assumed that fatigue lives are purely crack growth driven. However, these datapoints had conservative predictions as compared to the predictions made using the fatigue notch factor approach, where overestimation of the fatigue life could result in severe consequences in structural integrity-based assessments and design.

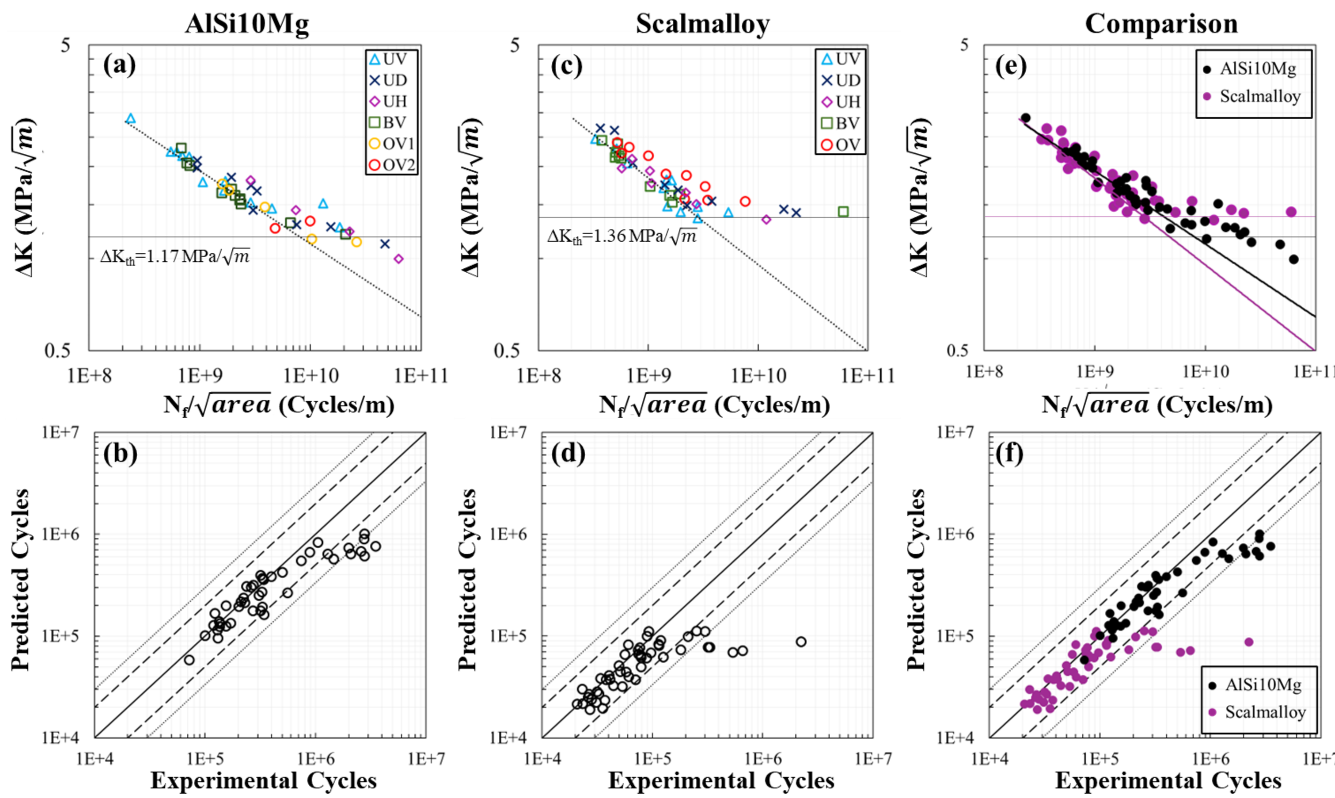

Figure 26. Shiozawa plots and fatigue life predictions for (a)-(b) AlSi10Mg, (c)-(d) Scalmalloy and (e)-(f) comparison of the two materials.

The upper and lower bound stress-life curves, obtained using the maximum and minimum defect sizes from each dataset and by assuming the cracks to be on the surface, are predicted using the Shiozawa model in **Figure 27**(a) and (b) for AlSi10Mg and Scalmalloy, respectively. In addition, the fatigue limits from the El-Haddad model are shown for the maximum and minimum defect sizes as suggested by Minerva et.al, which were adequately captured by the El-Haddad model [133]. Most of the experimental datapoints fell between the prediction bounds for both alloys, with some of the conservative data lying beyond the upper bound curve, as seen at the stress level of 160 MPa for AlSi10Mg and stress levels of 250 and 300 MPa for Scalmalloy. It should be noted that the conservativeness might have been due to the upper and lower bound curves assuming surface cracks, which tended to be more detrimental, while not all specimens had initiations from surface exposed defects. Nonetheless, the unified approach combining fatigue life predictions from crack growth and fatigue limit-based approaches using the critical defect characteristics appeared to be an effective way of describing the stress-life behavior of L-PBF aluminum alloys.

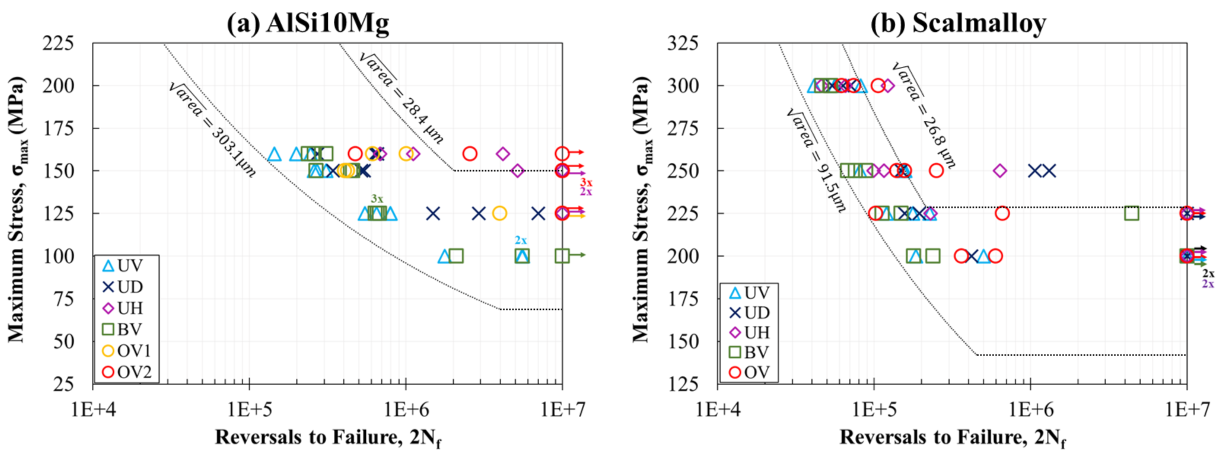

Figure 27. Stress-life fatigue plots with the predicted upper and lower bound stress-life curves from Shiozawa, and the fatigue limit from the El-Haddad model for (a) AlSi10Mg and (b) Scalmalloy.

3.5. Conclusions

In this study, the effects of volumetric defects on the fatigue properties of L-PBF AlSi10Mg and Scalmalloy were examined. Specimens were fabricated in the recommended, underheated and overheated conditions, by varying the process parameters to induce various types of volumetric defects commonly observed in L-PBF Al alloys. To further introduce variability in defect features (such as the projected size of LoFs on the loading plane), specimens were fabricated in the vertical, diagonal and horizontal orientations. Fatigue testing was performed and the fracture surfaces analyzed to examine the critical crack initiating defect features. The following conclusions can be drawn from the results:

1. The stress-life behavior of both L-PBF AlSi10Mg and Scalmalloy exhibited significant scatter due to the presence of porosity. The shortest fatigue lives for AlSi10Mg specimens were for vertically fabricated specimens using recommended and underheated process parameters, which also had the highest porosity in the XCT analysis. The fatigue lives for

Scalmalloy were comparable for all conditions with significant overlap and scatter which was correlated to their similar defect content.

2. Fractography revealed near surface/surface features to always be responsible for crack initiation in AlSi10Mg and Scalmalloy specimens. Large LoFs, and occasionally GEPs and KHs, were observed at the fracture origins for AlSi10Mg. For Scalmalloy specimens, in addition to volumetric defects, microstructural inhomogeneities/oxide particles and occasionally fine-grained regions were sites of crack initiation.
3. The normalized stress-life behavior for AlSi10Mg showed a significant reduction in scatter, when the defect features were incorporated in the fatigue limit calculation. While an improvement was noted in the normalized stress-life behavior for Scalmalloy, some pronounced scatter was still observed. This was due to the overlap in the measured defect sizes for the fractured and runout specimens, which could not be adequately accounted for by the El-Haddad model.
4. Consequently, predictions of the stress-life behavior using the fatigue notch factor-based approach were effective for AlSi10Mg but not for Scalmalloy. This was attributed to the uncertainty in the measurement of crack initiation regions and the location of the defects relative to the coarse- and fine-grained regions, where different near-threshold crack growth behaviors could be observed due to crack closure effects.
5. The use of Shiozawa model, which applies only to the stable crack growth phase, yielded acceptable fatigue life predictions for both materials. This was ascribed to both materials exhibiting similar crack growth behavior and the model being more robust since a significant portion of the datapoints of both materials fell in the mid cycle fatigue regime, where fatigue life is considerably spent in crack propagation. The predicted fatigue lives

using the Shiozawa approach was either within a scatter band of 3 or on the conservative side.

6. Fatigue design curves combining fatigue life predictions using Shiozawa with fatigue limit from El-Haddad model were able to sufficiently describe the stress-life behavior of both L-PBF AlSi10Mg and Scalmalloy, demonstrating the efficacy of unified approaches in fatigue assessments of AM Al alloys.

4. Non-destructive detection of critical defects in additive manufacturing [134]

4.1. Introduction

Volumetric defects, such as lack-of-fusions (LoFs), gas entrapped pores (GEPs), and keyholes (KHs), are well known be detrimental to the fatigue resistance of certain additively manufactured (AM) alloys, such as AlSi10Mg, Ti-6Al-4V, and 17-4 PH stainless steel, etc. [24,88,135–137]. These defects are sites of stress concentration and, under cyclic loading, can result in accelerated fatigue crack initiation [138]. Accordingly, any variations in their characteristics that affect the stress concentration, such as size, shape, and location, can impact the extent of such acceleration and introduce significant uncertainty in the fatigue behavior of AM parts [23,109]. Therefore, non-destructive examination (NDE) techniques that can accurately reveal the internal defect structure within the parts can provide valuable information regarding their quality and are highly desirable [100,139,140]. With accurate defect-sensitive fatigue models, such defect information can be used to indicate the life of AM parts under service loads and accelerate their qualification by reducing the need for extensive campaigns of destructive testing at both coupon and part scales [5,141].

Among various NDE techniques, X-ray computed tomography (XCT) stands out due to its unique ability to detect volumetric defect features at micrometer and sub-micrometer levels of physical resolution [142,143]. Nevertheless, XCT is relatively time consuming and, due to constrains imposed by the X-ray attenuation within materials and the pixel count of the optical sensors, is well known to suffer from the tradeoff between resolution and the scanned volume [144]. Generally, fine physical features are more challenging to be resolved in a larger part, because each voxel must register larger spatial volume for larger format scans and the X-ray attenuation is more severe in thicker materials, deteriorating the signal-to-noise ratio [142,145,146]. While employing higher voltage sources can increase X-ray transmittance, it does not necessarily improve resolution, since the X-ray beam spot size typically increases with increasing voltage which adversely affects imaging quality [145]. Accordingly, in an industrial setting, where large quantities of AM parts (likely large in size) need to be scanned in limited time, the resolution achieved by the XCT scans is often not ideal.

At a reduced scan resolution, the imaging contrast of fine geometrical features whose size approaches or falls below the size of a voxel may become indistinguishable from that of the noise, leading to detection failures [147]. These geometries can be the entirety of small GEP (see **Figure 28(a)**) or parts of a larger defect, such as the thin webbings in a LoF (see **Figure 28(b)**). This implies that the probability of detection (POD) of defects, especially small ones, therefore markedly declines with the decreasing resolution. Large defects, although their POD may be less sensitive to resolution, can be significantly misrepresented by XCT scans at low resolutions, depending on their shape [101]. However, KHs are near spherical, generally lack features that extend far from their bulks [148], and can be captured by the low-resolution scans with good reliability if they are several times larger than a voxel (see **Figure 28(c)**). On the other hand, LoFs are irregularly shaped and typically comprise thicker, bulkier regions and thin webbings (see **Figure 28(b)**). At reduced resolutions, while the bulkier regions can still be captured by the scans, the thin webbings tend to be missed. As a result, a large LoF defect may appear as one or a few smaller defects and, accordingly, its size can be severely underestimated. In some extreme cases, LoFs appear as only a few disconnected, globular features and are missed by the scans altogether (see **Figure 28(d)**).

As such, the efficacy of an XCT system in detecting volumetric defects, i.e., *the POD*, and in determining their sizes and other geometrical features, i.e., *feature errors*, can be significantly dictated by the shapes of defects within their population. This study aims to evaluate the quality of XCT scans by quantifying the POD and the feature errors with differentiating defects' geometry. Moreover, it devises a methodology to improve the accuracy of lower-quality scans in estimating the size of volumetric defects, especially larger LoFs. The focus of this study is on the characterization of process-induced volumetric defects which are inherently challenging to avoid due to the nature of the AM process, even in machined parts free of any surface anomalies. Different levels of scan quality are achieved by XCT scanning an identical, laser powder bed fused (L-PBF) AlSi10Mg material volume multiple times at different coupon diameters (10, 6, and 3 mm) and voxel sizes (10.8, 6.4 and 3.4 µm) in a factorial experiment. The AlSi10Mg coupon is fabricated with a set of process parameters to induce all three types of volumetric defects, i.e., LoFs, GEPs, and KHs. The examination of the identical material volume permits the true one-to-one comparison of the same volumetric defects across different acquisition conditions. It is shown that both POD and feature errors are indeed significantly influenced by the types of defects within the material volume. Although the finer features of a LoF, i.e., webbings, tend to be lost as the scan quality reduces, certain critical information, such as its size, can be partially recovered as long as a few of its bulkier regions can be captured and identified by applying a distance-based criterion, established in this research.

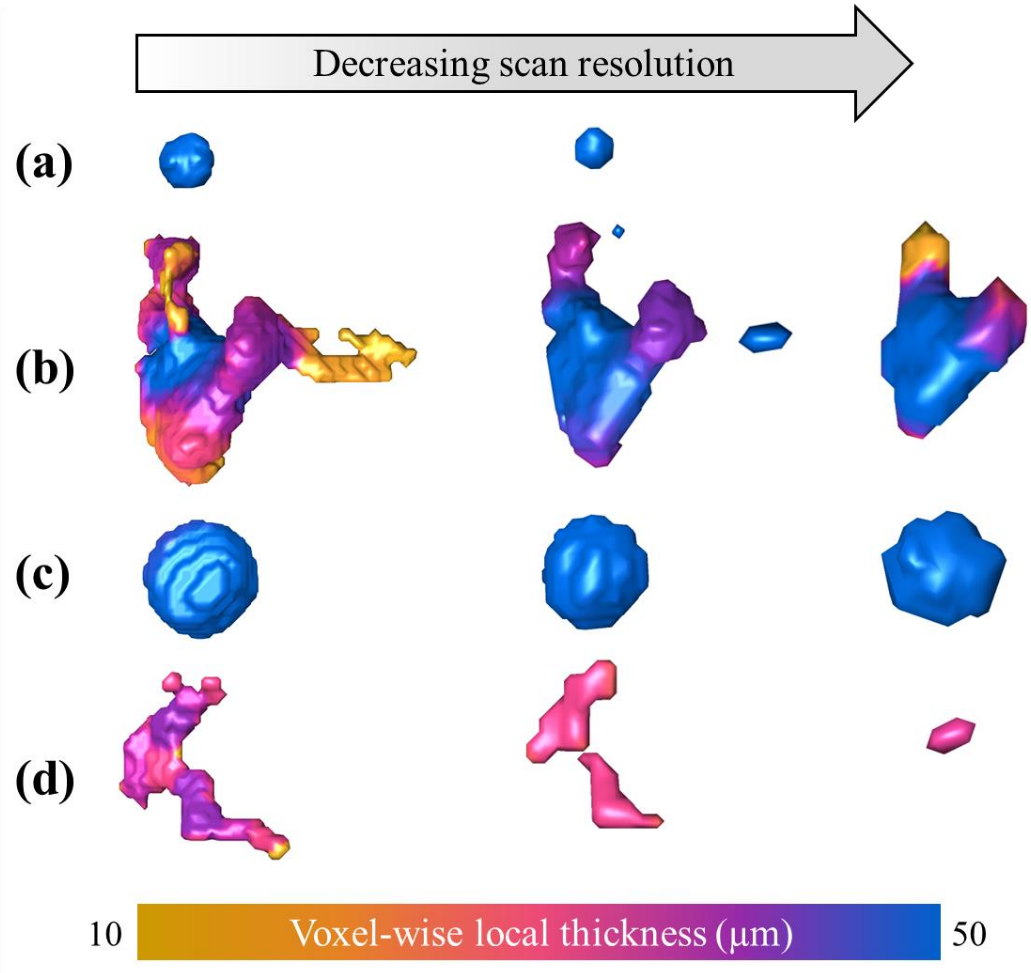

Figure 28. The influence of XCT scanning resolution on the detected morphology of various types of defects. The defect types shown are: (a) GEP, (b) LoF consisting of thin webbings extending out of a single bulky region, (c) KH, and (d) LoF with less bulky features.

4.2. Methods

4.2.1. Fabrication and XCT scanning procedures

A cylindrical AlSi10Mg coupon (11mm in diameter and ~45mm in length) was fabricated on Renishaw RenAM500Q laser powder bed fusion system. Argon-atomized AlSi10Mg powder supplied by Renishaw was used as the feedstock and the quad-laser strategy working in a stripe pattern was adopted for fabrication. The recommended process parameters were employed which were able to induce LoFs, GEPs and KHs throughout the volume of the coupon. Post fabrication, the coupon was machined to a 10 mm diameter to remove any surface anomalies and to examine the internal porosity. The 10 mm coupon was XCT scanned at three different voxel sizes following the procedures described below. Afterwards, the coupon was further machined to diameters of 6 and 3 mm, and the scanning procedures were repeated according to the methodology described below at each step of the machining.

The XCT scans were performed using a Zeiss Xradia 620 Versa system. A total of 9 scans were conducted for various combinations of voxel/coupon sizes as presented in **Figure 29**. Three different voxel sizes of 3.4, 6.3 and 10.8 μm were used to scan the coupon after each step of machining. These voxel and coupon size selections were made to ensure high quality imaging of the defect features found in L-PBF AlSi10Mg, while also considering certain constraints presented by scanning large AM components where the voxel size-part size tradeoff can make it necessary to scan AM parts at less than ideal resolutions in industrial settings. The voxel size was adjusted between the 6.3 and 10.8 μm by changing the source-to-sample-to-detector distances while keeping the objective lens of 0.4X identical. A lens of higher optical magnification of 4X was used for the 3.4 μm voxel size. For all the scans, a total number of 1600 projections were taken to maximize the likelihood of achieving the highest contrast view of the defects within a reasonable scan time. The transmittance for all scans was kept >15%, while also considering the scan quality and the time to obtain high quality XCT images. The voxel size used in the "*voxel size-coupon size*" naming convention for the acquisition parameters was simplified by truncating the digits after the dot. For example, *6 μm-10 mm* denoted the scan with the 6.3 μm actual voxel size, etc.

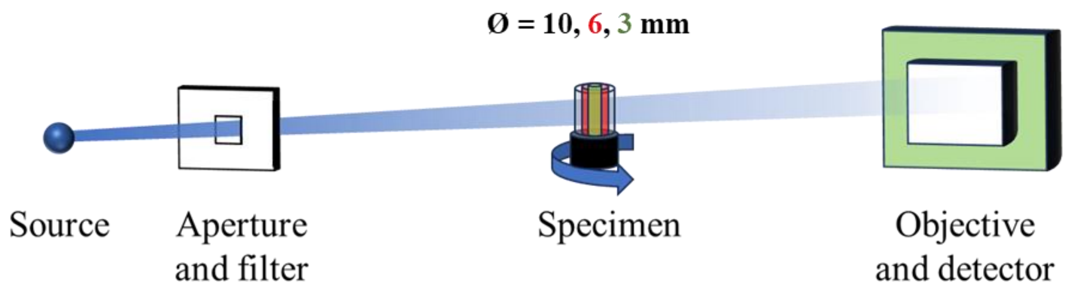

Specimen size	Voxel size=10.8 µm	Voxel size=6.3 µm	Voxel size=3.4 µm
10 mm	Voltage=70 kV Power=8.5 W Time=**2h** Obj=0.4x Transmit=22 %	Voltage=80 kV Power=10 W Time=**3h** Obj=0.4x Transmit=26 %	Voltage=100 kV Power=14 W Time=**9h** Obj=4x Transmit= 29%
6 mm	Voltage=60 kV Power=6.5 W Time=**2.5h** Obj=0.4x Transmit=28 %	Voltage=70 kV Power=8.5 W Time=**3h** Obj=0.4x Transmit=33 %	Voltage=100 kV Power=14 W Time=**9h** Obj=4x Transmit=39 %
3 mm	Voltage=60 kV Power=6.5 W Time=**2h** Obj=0.4x Transmit=45 %	Voltage=60 kV Power=6.5 W Time=**3h** Obj=0.4x Transmit=46 %	Voltage=100 kV Power=14 W Time=**7h** Obj=4x Transmit=52 %

Figure 29. Schematic of the XCT set-up and the acquisition parameters for the various scans conducted in this study. The 3 mm coupon size scanned at a voxel size of 3.4 µm was considered as the 'ground truth'.

4.2.2. XCT post-processing, POD, and feature error analysis

The XCT projections were reconstructed in the Zeiss Reconstructor software. Following reconstruction, the images were segmented using Otsu thresholding to extract the defect features from the background material. All thresholded images were manually inspected to ensure the defect features were sufficiently captured. The binarized images were further processed in ORS Dragonfly software by despeckling and ensuring any CT image artifacts were removed for the porosity analysis. The 3D defects were labeled and several defect features including the volume, projected area, surface area, bounding box coordinates and centroid coordinates were obtained. A summary of the workflow is presented in **Figure 30** showing the methodology followed in this study for the POD and feature error analysis.

The various scans were aligned with the 'ground truth' dataset by translating, tilting, rotating and overlaying them on to the 'ground truth' scan so they occupied the same reference coordinate system. Defect centroids in the lower-resolution scans were then identified within the bounding box volume of the corresponding 'ground truth' defects. The hit/miss POD analysis followed guidelines from ASTM E2862 and MIL-HDBK-1823A [149,150]. Since the objectives of this study pertained to the identification of defect features critical to fatigue loading scenarios, the projected $\sqrt{area}$ was selected as the size parameter for further analysis. In this work, the plane perpendicular to the build direction was selected as the projection plane. To quantify the POD, a defect was classified as a hit if it was detected within the bounding box of the 'ground truth' defect and, as a miss if no detection occurred within that bounding box. The hit/miss responses were plotted against the 'ground truth' defect sizes, with the miss data being assigned a POD of 0 and the hit data being assigned a POD of 1. The probit link function was used to generate the sigmoid POD curve and to obtain the probabilities from the binary outcomes, which is defined as follows:

$$\mathrm{Probit}\left(\mathrm{POD(a)}\right) = \Phi^{-1}\left(\mathrm{POD(a)}\right) \tag{4.1}$$

where Φ is the cumulative standard normal distribution and POD(a) is the probability of detection function with respect to size, a, of the defect.

The feature errors were analyzed by comparing various size features such as the volume, surface area and $\sqrt{area}$s between the low-resolution defect and the corresponding 'ground truth' defect. This allowed the measured $\sqrt{area}$ vs. true $\sqrt{area}$ plots to be constructed [151]. In addition, it was observed that some of the lack of fusion defects appeared as a cluster of entities in the corresponding lower-resolution scans. This was a consequence of spatial resolution limitations, where the thin sections of the defects could not be resolved in the XCT images leading to multiple entities being detected, that belonged to the same defect as informed by the 'ground truth' scan. To address this and recover some of the lost information, a polygonization approach was proposed to estimate the area in between the cluster of defects that belonged to the same defect. The procedure involved calculating the distances between the pairwise entities in the low resolution scans and establishing a distance criterion to identify which entities were part of the same defect. The criterion for each resolution, was used to construct a convex hull using the bounding box coordinates of the clustered entities, allowing for the calculation of the projected areas as illustrated in **Figure 30**.

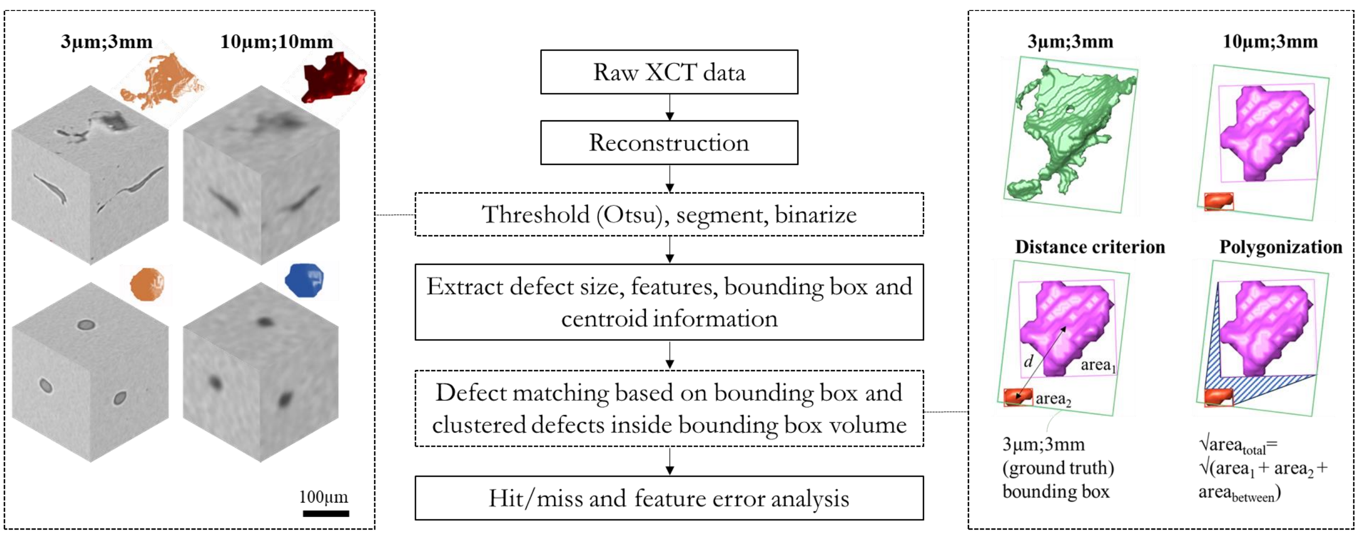

Figure 30. Flowchart showing the procedure for XCT image processing, defect feature extraction and matching with the "ground truth" dataset for the POD and feature error analysis.

4.3. Results

4.3.1. Assessing the quality of XCT scans – probability of detection (POD)

Conventionally, the quality of an XCT scan is quantified by the POD of a defect as a function of some measure of the defect's size, regardless of its shape [149]. The POD is obtained from the hit/miss defect analysis performed on a sample whose ground truth information about its defect population is known and is typically presented as a sigmoid POD curve [152,153]. The hit/miss analysis was performed using a defect detection algorithm that enabled one-to-one matching of defects between the low-resolution scans and the ground truth. A defect was flagged as a hit if it was detected within the bounding box volume of the ground truth defect; otherwise, it was flagged as a miss if no detection occurred. The POD curves for all defects, regardless of their geometry, along with their 95% confidence intervals are shown in **Figure 31** in black lines and gray shades for the XCT scans performed on the AlSi10Mg coupon at different permutations of voxel sizes and coupon diameters. The permutations are designated by the convention "*voxel size-coupon size*", e.g., *3 μm-6 mm* represents a 3 μm-voxel scan on a 6 mm-diameter coupon. The $\sqrt{area}$ parameter was selected to represent defects' size since it has been shown to correlate well with fatigue criticality [92,154]. In this work, the projection plane for the size measurements was selected to be the one perpendicular to the build direction. To avoid false detection of volumetric defects from noise, the decision threshold was set to a $\sqrt{area} \geq 2$ voxels, i.e., any defects that appeared smaller than this size are flagged "missed" (see **Figure S3** in Supplemental Materials showing the effect of noise threshold on POD). In the case of multiple small features of a large LoF being detected, a positive detection was registered if at least one feature exceeded the decision threshold size. Additionally, the sizes of all the missed and detected defects are shown in this figure as markers on the lines of POD = 0 and POD = 1, respectively. It should be noted that, with the *3 μm-3 mm* scan as the ground truth, all of the defects were detected in the *3 μm-6 mm* and *3 μm-10 mm* scans; in these cases, the POD curves appear as vertical lines at $\sqrt{area}$ = 6 μm and are therefore not presented here.

The figure shows that and the POD curve clearly shifted towards larger $\sqrt{area}$ with increasing voxel size (compare the black curves in **Figure 31(a)-(c)** with the ones in **Figure 31(d)-**

(f)). Moreover, the coupon size also have influenced the POD, with larger coupons having right-shifted POD curves [145]. In addition to the POD itself, the uncertainty of the POD (represented by the width of the confidence bands shown by the shaded regions) also increased with voxel size and coupon diameter. The ground truth of the largest missed and smallest detected defects for each voxel/coupon size combination is also visualized in each panel, with arrows pointing the corresponding datapoints to the defect's visual representation, and their reported $\sqrt{\text{area}}$s. Evidently, the largest undetected defect was always a LoF and the smallest detected one was always spherical (could be a KH or GEP) in all scans, and the former were always significantly larger than the latter. For instance, the largest undetected defect in the *10 μm-10 mm* scan was a LoF and had a $\sqrt{area}$ = 95 μm; the smallest detected one in the same scan was near-spherical and had a $\sqrt{area}$ = 38 μm. The stark contrast between the size of the largest undetected/smallest detected defects suggested that the POD depends on the shape of the defects and should be quantified separately for each defect type [155].

To further elucidate how the defects' shape may affect POD, the defects were divided into two categories according to their type, i.e., near-spherical (comprising KHs and GEPs with sphericity values>0.7) and irregular (comprising LoFs only with sphericity values≤0.7) [156]. The classification of defects into KHs, GEPs, and LoFs was achieved following the automatic approach set forth by the authors' prior work and was verified by manually inspecting the classified defects to ensure they were appropriately assigned to their respective classes [71]. The two additional POD curves of near-spherical and irregular defects for each set of acquisition parameters are presented in **Figure 31** in green and blue with shades of the corresponding colors. For defects of size up to ~10 voxels, it appeared that the POD for irregular defects (blue curves) was lower than those for near-spherical ones (green curves) and when considering all defects in the scan volume indiscriminately (black curves). In addition, the gently sloping POD curves of the irregular defects also implied that the POD gradually improves with an increase in the defect size. This was opposed to the behavior of the near-spherical defects gaining high detectability once their size approached the decision threshold, which was set as $\sqrt{area} \geq 2$ voxels in this study. The observation held true for all the acquisition parameters investigated in this study and was more pronounced at the 10 μm voxel size and for the 10 mm coupon diameter, as observed in **Figure 31(c)-(f)**. Furthermore, the uncertainties associated with the POD of near-spherical defects were significantly lower than the irregular ones and remained relatively unchanged with an increase in voxel/coupon size (compare the widths of the green and blue shades in **Figure 31**).

The shallower and more uncertain POD curves of LoFs than those of near-spherical defects (including GEPs and KHs) originated from the strong variability of LoFs' shape [157]. On one hand, some LoFs comprised only thin features, which tended to be lost with the deteriorating imaging quality which was the case for the largest undetected defects in all acquisition conditions (see the ones visualized in each panel of **Figure 31(c)-(f))**. As an example, the appearances of one of such LoFs (i.e., the largest undetected defect in the *10 μm-10 mm* scan) in the *3 μm-3 mm* (ground truth), *6 μm-6 mm*, and *10 μm-10 mm* scans, are visualized in **Figure 31(g)** alongside the corresponding gray scale images. It is evident from the figure that, as the resolution reduces, the fine features of this serpentine shaped defect became gradually indistinguishable from noise, such that in the *10 μm-10 mm* scan only a cluster of small entities could be segmented. Since all of them fell below the decision threshold (i.e., 2 voxels), the defect was recorded as undetected.

On the other hand, some LoFs contained at least one bulky region and, despite the loss of thin webbing to reduced scan resolutions, could still be relatively reliably detected (see the smallest detected LoFs visualized in **Figure 31(c)-(f)**). One example of this case (i.e., a defect of a $\sqrt{area}$

equivalent to 50% POD in the *10 μm-10 mm* scan) is illustrated in **Figure 31(h)**, following the format used for **Figure 31(g)**. In contrast, near-spherical defects generally lacked thin features and could be detected as long as the size of the segmented objects is above the decision threshold of 2 voxels (see **Figure 31(i)**, which shows the smallest detected defect in the *10 μm-10 mm* scan). The POD of a near-spherical defect was influenced by both the morphology of the defects and the level of noise within the images. Larger, more spherical defects could be reliably detected, even in the lower-resolution scans. For smaller defects whose shape deviated from a sphere and had $\sqrt{area}$s approaching the decision threshold, the POD was impacted by the image noise more significantly, as the quality of XCT scans degraded.

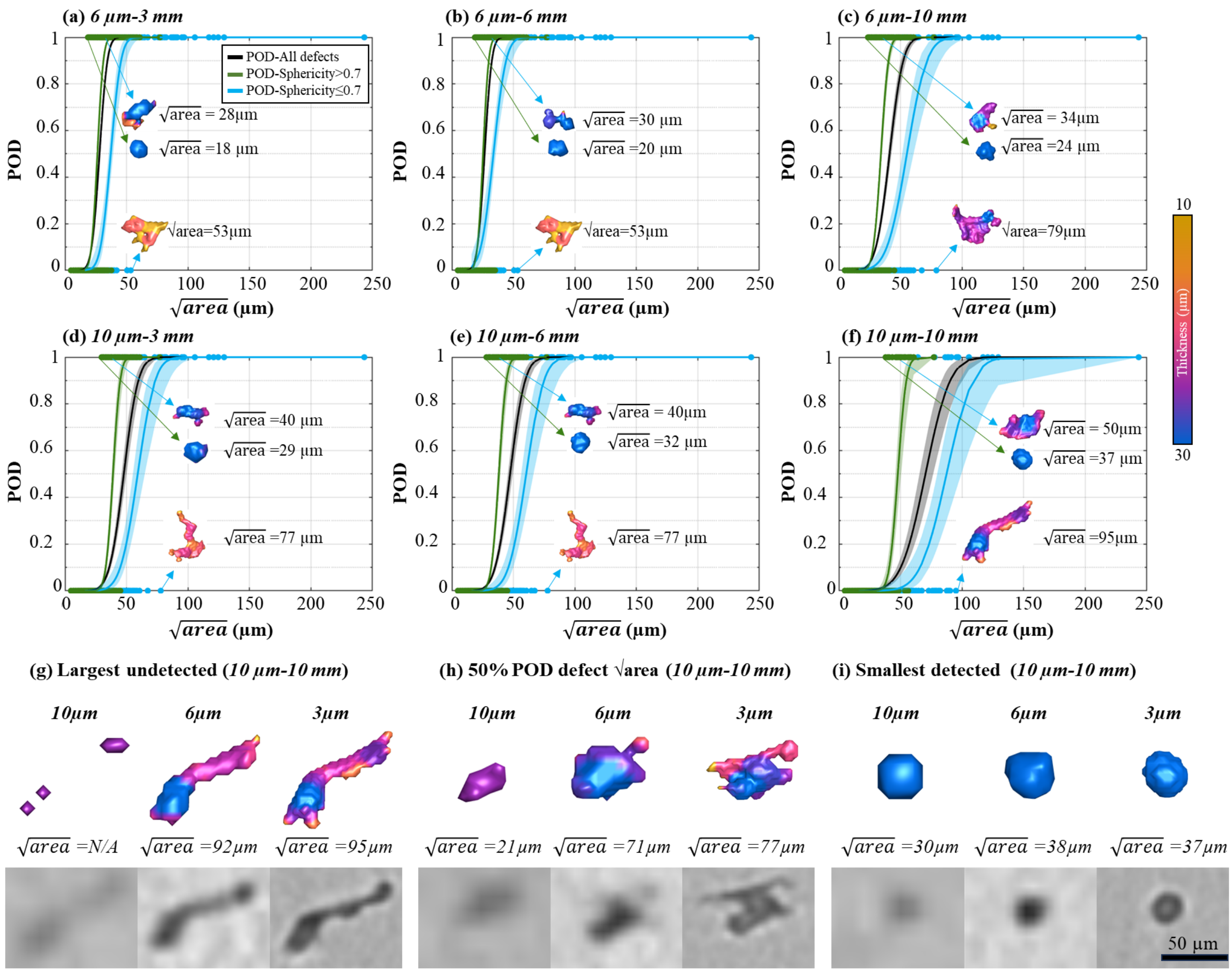

Figure 31. (a)-(f) POD curves for various voxel/coupon size scans and for different defect classes based on their sphericity values, and (g)-(i) visualization of the largest undetected, 50% POD defect $\sqrt{area}$ and smallest detected defects in the *10 μm-10 mm* scan.

4.3.2. Assessing the quality of XCT scans – feature errors

While the quantification of the POD presents valuable information regarding the reliability of the XCT examination in detecting a defect of a given size, it does not account for the errors in the measurements of their features, such as size [146,158]. Depending on the acquisition parameters used for the XCT inspection, the detected features may vary drastically for the same defects, resulting in large errors in the feature measurements [146]. This could be due to several factors such as the loss of information as the voxel size increases and the lower signal-to-noise ratio as the part size increases which may result in fine features not being captured fully [159]. As a result of the lost fine features, defect populations acquired with lower resolutions typically contained smaller and rounder defects when compared to the ground truth, as shown in the sphericity vs. $\sqrt{\text{area}}$ plots presented in **Figures S1 and S2** of the Supplemental Material.

The measured vs. ground truth $\sqrt{area}$ for the various scans performed with different acquisition parameters are plotted in **Figure 32**. Note, again, that the *3 μm-3 mm* scan was used as the ground truth. Here, the measured areas were calculated by summing up the areas of all the entities detected inside the bounding box of the corresponding ground truth defect. The black diagonal line in the figures represents the 1:1 identity. The defects that were not detected by XCT scans, i.e., the missed ones presented in **Figure 31**, correspond to "0" $\sqrt{area}$ and are shown with the red markers on the horizontal axis. The measured sizes appeared to be strongly affected by the voxel size. For instance, the scans with 3 μm voxel (i.e., the same voxel size as the *3 μm-3 mm ground truth scan*) measured the $\sqrt{area}$ with the highest fidelity. As the voxel size increased to 6 μm, the $\sqrt{area}$ was underestimated for most defects. The irregular defects with low sphericity values appeared to be underestimated more significantly than the near-spherical. Interestingly, increasing the voxel size to 10 µm only worsened the underestimation for the irregular defects further and did not significantly affect the sizing errors for the near-spherical ones. Moreover, some influence of the part size on the measured $\sqrt{\text{area}}$ was also observed, especially at the largest coupon sizes of 10 mm where the errors were more pronounced for voxel sizes of 6 and 10 µm.

The appearances of one near-spherical and one irregular defect, the latter's size tends to be consistently underestimated by XCT scans, with all acquisition parameters are visualized in each panel of **Figure 32**, and their appearance in the ground truth scan are provided in upper left of the figure. The near-spherical defect, whose size was measured to be close to the ground truth size and remained relatively unchanged with changes in acquisition parameters, showed a round morphology in all scans. This defect had a local thickness of ~50 µm, lacked any features extending from its spherical core region, and was reliably captured in XCT scans at all resolutions.

In contrast, the LoF consisted of thin webbings (shown in blue in the top left panel of **Figure 32**) extending out of a bulkier region (shown in yellow). In this case, the local thickness of the defect had a significant influence on the detectability of its features in the lower-resolution scans. For instance, in the *3 µm-6 mm* and *3 µm-10 mm* scans, all features of the defect were detected including the thin webbed regions, which resulted in the measured $\sqrt{area}$ being in close agreement with the ground truth. However, as the voxel size increased to 6 µm, some features with low thickness values could not be captured. At the voxel size of 10 µm, a significant portion of the LoF could not be captured, and only the bulky core region was detected resulting in a severe underestimation of the defect size. Moreover, the loss of feature information for the LoF was further exacerbated by an increase in coupon size, and the most severe underestimation was seen for the 10 mm coupon size at both 6 and 10 µm voxel sizes.

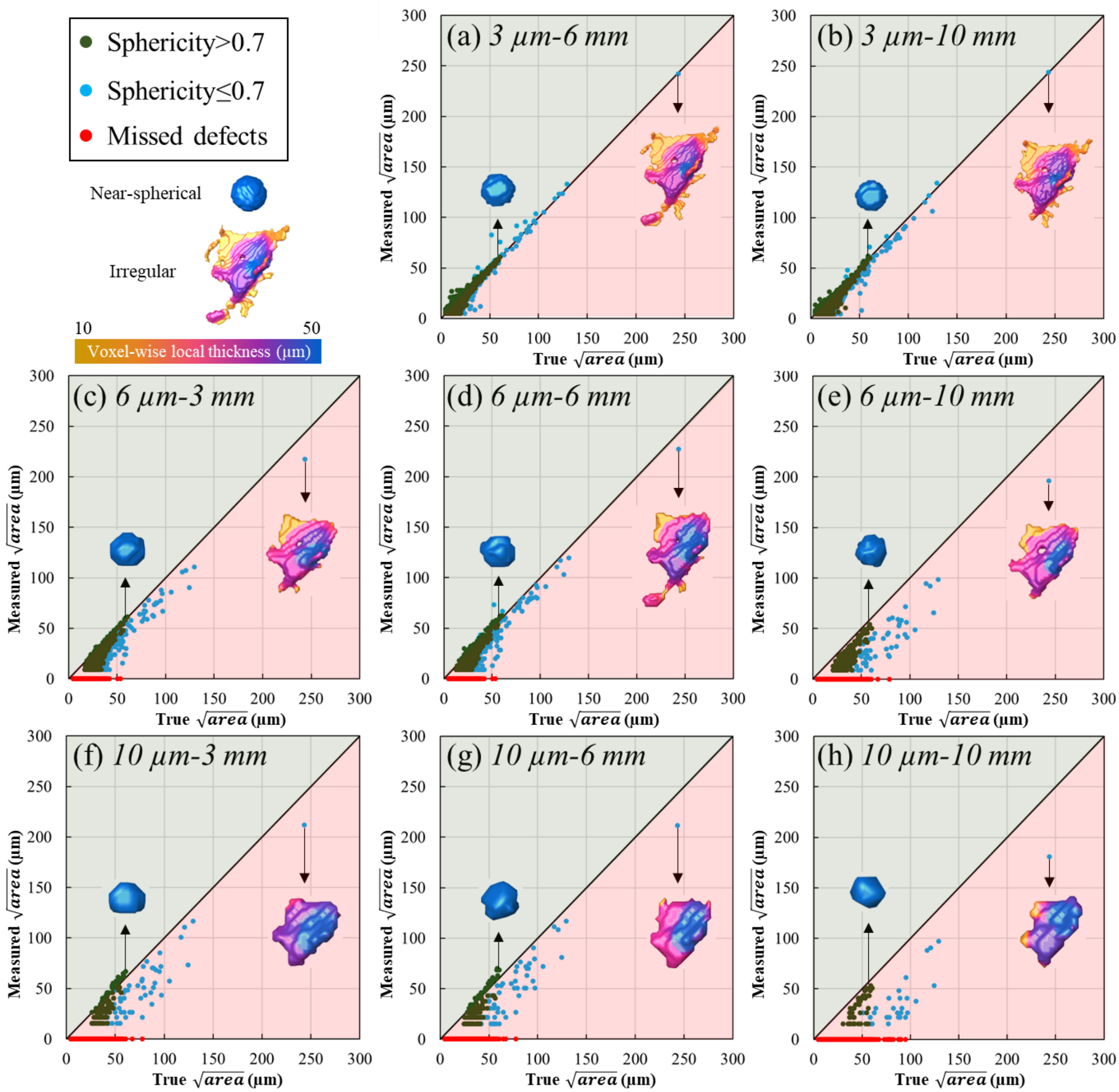

Figure 32. Measured vs. true $\sqrt{area}$ for all matched defects across various voxel/coupon size scans. The true size was obtained from the *3 µm-3 mm* scan.

4.3.3. Reducing feature errors – applying distance criterion

The sizing error in $\sqrt{area}$ was the most significant for the irregular defects (i.e., the LoFs), which stemmed from their fine features being missed due to the resolution limitations. Although the thin webbings could not be detected and the LoFs appeared as a cluster of entities at reduced resolutions, the convex hull constructed around these entities should better represent the $\sqrt{area}$ of the LoF, if the registry of these entities to the LoF defect could be established. Based on this understanding, a procedure, "polygonization approach", was devised to reduce the sizing error of irregular defects. The procedure began with identifying a few (approximately 20) larger and more critical LoFs from the ground truth whose appearance changed to at least two isolated, small entities in the lower-resolution scans. **Figure 33** illustrates the proposed polygonization procedure using one LoF as an example. For each LoF at each resolution (see **Figure 33(a) and (b)**), the largest pairwise, centroidal distance (*d*) among the entities was measured. Then, at each resolution, the greatest d value calculated for the limited number of LoFs (~20) was set as the distance threshold (**Figure 33(c)**). This threshold was used to examine all clusters of small entities detected at that resolution to determine if they belonged to the same large LoFs by blindly applying to the entire dataset for the low-resolution scan (**Figure 33(d)**). With this approach, the recovery of critical defect information from scans on relatively large parts, whose resolution is often less than ideal, may be possible as long as the threshold distances for the volumetric defects in the same material with increasing part size and voxel size is established based on limited ground truth information.

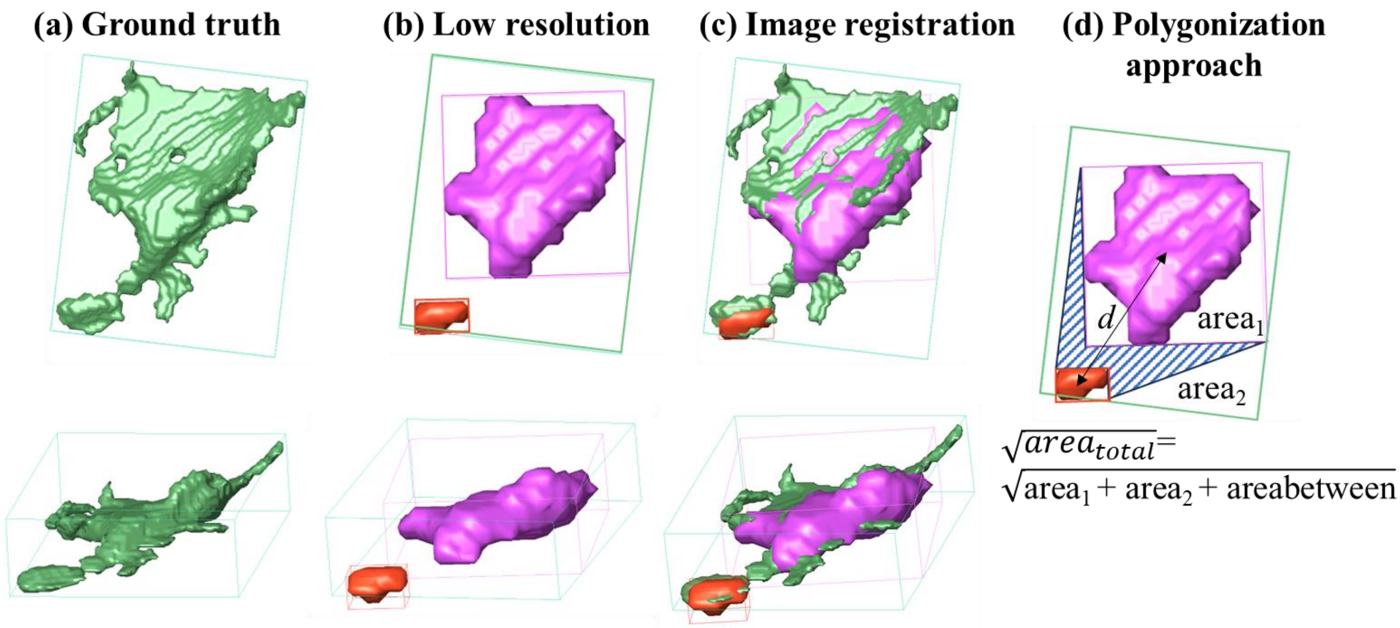

Figure 33. (a) Ground truth defect, (b) corresponding entities detected in the low resolution scans, (c) defect matching between the ground truth and low resolution scan based on the bounding boxes, and (d) polygonization approach considering the area in between the defects.

The measured vs. true $\sqrt{area}$ plots are presented in **Figure 34**, after applying the distance criterion to construct the convex hull using the bounding boxes of the clustered entities and recalculating the $\sqrt{area}$s. In addition, the number of defects with two or more bulky regions (Poly) in the low-resolution scans, which the polygonization approach was able to improve the sizing accuracy for, are reported in the bottom right side of each panel along with the number of defects which only had singular bulky regions (Single), The measured values appeared to significantly improve, especially for the larger defects, despite the size for some defects being overestimated. The overestimation was acceptable as they would lead to a more conservative assessment of the fatigue resistance.

To further understand the effectiveness of the proposed polygonization approach in improving the $\sqrt{area}$ measurements for various irregular defects, three representative LoFs were selected for further examination. The markers for the three defects have been numbered in **Figure**

34 for easy comparison. The 3D renderings of the defects are presented in **Figure 34**, with the ground truth shown in the top left of the figure and the detected morphologies for each acquisition parameter visualized on the measured vs. true $\sqrt{area}$ plots. For Defect 1, which was the largest defect in the dataset and whose size was underestimated in the 6 µm and 10 µm scans (see **Figure 32**), applying the polygonization procedure improved the measured $\sqrt{area}$, resulting in significantly reduced errors (**Figure 34**) and, in some cases, slight overestimation into conservativeness. As the scan resolution decreased with an increase in the voxel size from 3 µm to 6 µm and 10 µm and with an increase in coupon size from 3 mm to 6 mm and 10 mm, Defect 1 "disintegrated" into a cluster of a large and a small entity. Since both could be consistently detected in all acquisition conditions, Defect 1's $\sqrt{area}$ was adequately captured by constructing the convex hull around the bounding boxes of these entities.

In contrast, for Defects 2 and 3, the polygonization procedure was only effective in some of the scans. This included all scans conducted at the 6 µm voxel size and the *10 µm-6 mm* scan for Defect 2, and *6 µm-3 mm, 6 µm-6 mm, 10 µm-3 mm and 10 µm-6 mm scans* for Defect 3. As is evident in the ground truth images in **Figure 34**, Defects 2 and 3 each contains only one bulky region and some thinner webbed features. In certain acquisition conditions of reduced resolution, the webbed features were lost and only the singular bulky region of each defect was detected, which was insufficient for the convex hull to be constructed. Indeed, the acquisition conditions where the procedure showed improvement in the measured $\sqrt{area}$ were the ones that successfully captured multiple entities for each defect. For example, defect 2 saw a large improvement in the measured $\sqrt{areas}$ for most scan parameters and was captured as 3 separate entities in all of 6 µm voxel size scans and in the *10 µm- 6 mm* scans. However, only the bulky region of the defect was detected in the *10 µm- 3mm* and *10 µm-10 mm*. This could be attributed to the *10 µm-3 mm* scan having a higher transmittance than the *10 µm- 6mm* and *10 µm- 10mm* scans which resulted in a lower contrast for defects closer to the specimen surface, which was the case for Defect 2 (see **Figure S4 (f)-(j)** in the Supplemental Material) [160]. In addition, for the larger coupon diameters, the more severe attenuation of photons resulted in a poor signal-to-noise ratio and can explain the graininess and loss of features in the *10 µm-10 mm* XCT images (see **Figure S4 (f)-(j)** in the Supplemental Material).

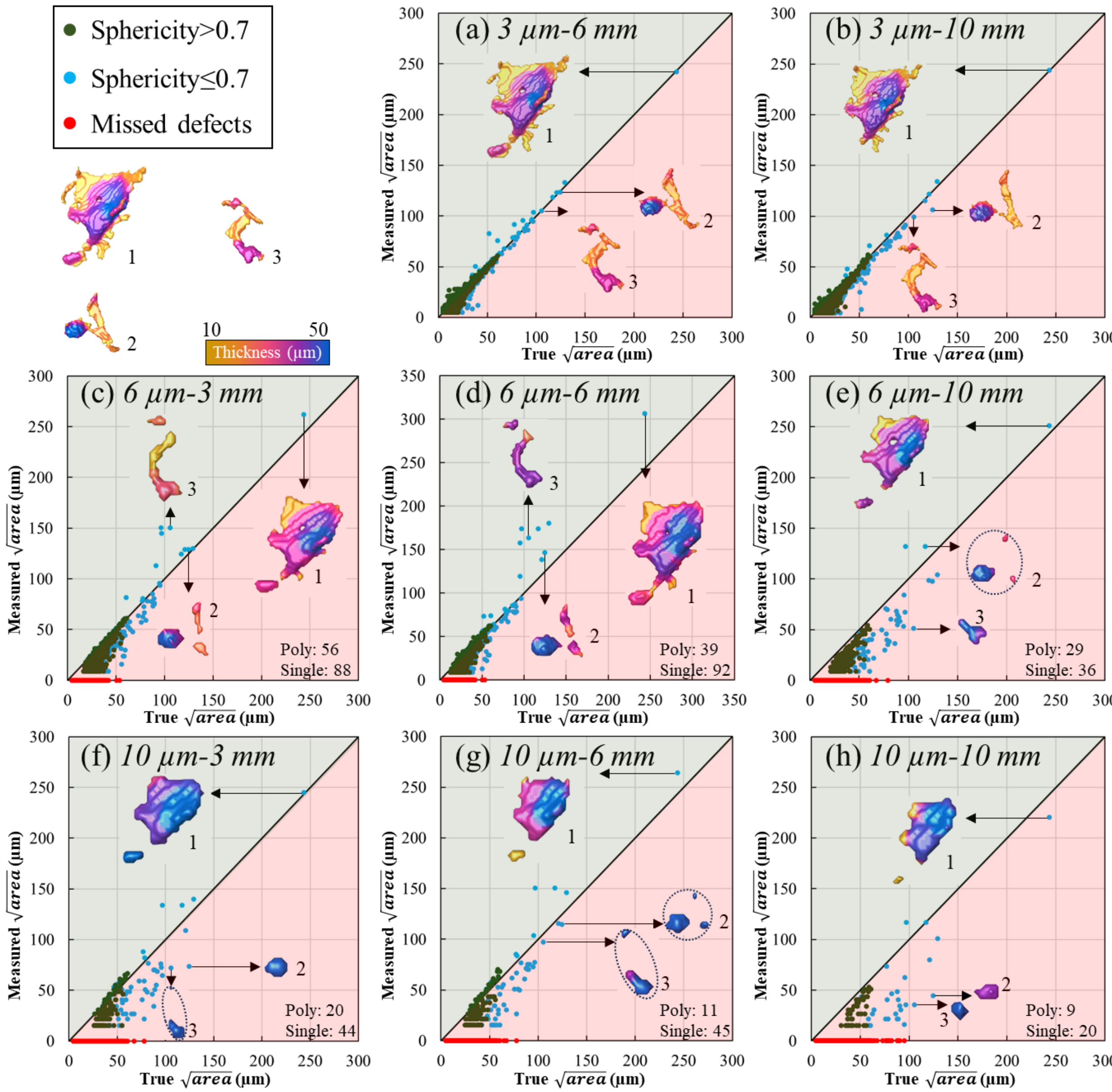

Figure 34. Measured vs. true $\sqrt{\text{area}}$ considering the distances between neighboring defects and applying polygonization procedure for any defects within the distance thresholds. The number of defects with two or more bulky regions (Poly) are also listed along with the number of unmodified defects with singular bulky regions (Single). The true size was obtained from the *3 μm-3 mm* scan.

4.4. Discussion

This work demonstrated that the efficacy of XCT on AM parts and how it can degrade with deteriorating imaging conditions, such as increasing voxel size and/or part thickness, significantly depend on geometries of defects within their population. The efficacy not only manifests in the probability of detecting volumetric defects (see Section 4.3.1) and but also in the accuracy in assessing defect features, such as size (see Section 4.3.2). While its general reducing trend with poorer imaging conditions is unavoidable and somewhat expected, the sensitivity of XCT scan's performance to the defect geometry has not been well known. The latter can negatively impact the outcome of the prevailing industrial practice of NDE based structural integrity assessment on AM parts, which does not emphasize on the effect of defects' shape [89,95,98,161]. Taking damage tolerant fatigue approaches for example, they estimate service life of a part by integrating crack growth laws from the initial crack size to the final crack size at fracture [63,162–164]. They always assume the presence of life limiting flaws within the materials and, for the initial crack size, use the detection limit of the NDE technique on the part/material combination of interest determined from the POD (e.g., defect size corresponding to 90% POD at a confidence level of 95%, see **Figure 31**) even if no defects could be detected [92,165]. If the POD of an XCT system has been measured from an artifact predominantly containing near-spherical defects, such as KHs and GEPs, the calculated detection limit would be an underestimation if the part of interest contains predominantly LoFs. Since fatigue cracks' growth rate are much slower when they are short, such an underestimation in the initial crack size would significantly overestimate the part life, leading to dangerous, severely non-conservativeness in design [166,167].

If defects can be detected, on the other hand, assessing the structural integrity of AM parts via NDE hinges upon whether key attributes of the most detrimental defects can be accurately registered [98,168]. While the accuracy of XCT in capturing the size of the near-spherical defects has been shown adequate and is not strongly impacted by the imaging condition, as long as the defects can be detected, the sizing accuracy of XCT for LoFs deteriorates significantly with reducing imaging quality. Specifically, with only the smaller, bulkier regions captured, the size of the LoFs is underestimated, leading to overestimations of parts' service life by, for example, the damage tolerant fatigue approaches.

Recognizing the characteristics of a LoF often comprising more than one bulkier region which can be more reliably detected by XCT scans of reduced resolution (see **Figure 28** and **Figure 34**), this work demonstrates that its size can be well represented by that of the convex hull constructed around these isolated regions, as long as their registry to the LoF can be established. With a set of threshold distance criteria to establish such registry, the overall sizing accuracy of XCT scans of reduced resolution for volumetric defects, especially the LoFs, has been shown to improve. Note that, given its working principle, this methodology is only effective for defects with a combination of a few bulky regions connected by thin features, e.g., large LoFs, and does not reduce sizing errors for defects with singular bulky features, e.g., KHs, GEPs, and smaller defects, or the ones without any bulkier regions, e.g., very small LoFs. In addition, it is a possibility that the procedure may combine two small spherical defects and consider them as a slightly larger entity if they fall within the distance thresholds, since it is not possible to distinguish between defects with a singular bulky region and a LoF with several bulky region in low resolution grayscale absorption images. Nevertheless, since the sizing error for the near-spherical defects is typically small and the small LoFs are typically not fatigue critical, the proposed approach is still expected to substantially benefit NDE based structural integrity assessment for AM parts despite these exceptions.

The proposed polygonization approach can help improve the compromised resolution of XCT imposed by part size, a challenge faced by many industrial radiographers. Specifically, important information regarding the critical defects' size in a relatively large AM part can be recovered from lower-resolution scans by understanding how defects' geometrical features are lost as scan resolution reduces. With a material sample excised from a similar part, this information and the threshold distance criteria can be obtained by XCT scans performed on the same material volume but at successively reducing coupon and voxel sizes.

Overall, although the results presented in this work, such as the POD curves and sizing error data, can potentially vary with material and acquisition setup, which affects the X-ray's attenuation and the resulting signal-to-noise ratio, the conclusions drawn should remain qualitatively valid for other AM materials/conditions. Specifically, process-induced volumetric defects such as KHs, GEPs, and LoFs are inherently present and characteristic of many families of AM metallic materials. Therefore, the importance in the consideration of the shape of volumetric defects within the industrial practice of NDE for AM parts highlighted in this work and proposed approach to improve the defects' sizing accuracy is expected to be applicable to many combinations of materials, fabrication techniques, and XCT imaging conditions.

In summary, this work investigated the influence of XCT acquisition parameters on the POD and feature errors with differentiating defect's geometry. Based on the results, the following conclusions were drawn:

- The POD for volumetric defects was significantly influenced by the shape of the defect. While near-spherical pores could be detected reliably across various XCT scanning conditions investigated in this study, the variability in the shape of LoFs resulted in a greater degree of uncertainty in their detection with worsening imaging quality.
- XCT accuracy in capturing defect features significantly deteriorated at reduced scan resolutions for LoFs due to a loss of information. This was attributed to the complex morphologies of LoFs which consisted of multiple bulky and webbed regions, with the latter having the most information loss associated with them. In contrast, the feature errors

were relatively smaller for small LoFs, GEPs and KHs, which consisted of single bulky regions which could be adequately captured across various XCT scan resolutions.

- It is possible to recover some information from low resolution XCT scans for large critical LoFs with two or more bulky regions. By using a distance-based criterion to interpolate in between the bulky regions, the defect geometry could be reconstructed, allowing for enhanced sizing accuracy.

5. Fatigue assessment of laser powder bed fused aluminum alloys via non-destructive examination

5.1. Introduction

Additively manufactured (AM) parts are inherently susceptible to manufacturing flaws, including volumetric defects [143,169]. These defects can degrade the fatigue resistance by acting as stress concentrators, inducing localized plasticity damage and causing accelerated fatigue crack initiation [24,135,157,170]. Lack-of-fusions (LoF), gas-entrapped pores (GEPs), and keyholes (KHs) are among the commonly observed AM induced defects [71,171–173]. The variations in defect types, morphologies, and their spatial distributions, stemming from the unique thermal histories experienced by each part, further complicates matters and introduces uncertainty in the fatigue behavior of AM materials [23,95,109]. In this regard, the accurate characterization of volumetric defect features, especially the fatigue critical ones, through non-destructive evaluation (NDE) techniques such as X-ray computed tomography (XCT) are highly desirable as they can help in understanding defect-fatigue relationships for AM materials [143].

The structural integrity of AM parts can be assessed using damage tolerant concepts from fracture mechanics if their fatigue behavior is defect-sensitive and the defect content is known [5,116,132,162]. Some of the current approaches make use of defect information obtained from NDE, treating volumetric defects as cracks whose growth from initial size to fracture-critical size determines the fatigue life [174,175]. The largest detected volumetric defect is typically taken as the critical defect; however, this may not always be accurate. It is understood that the XCT acquisition parameters and the part geometry, which govern the resolution of an XCT scan, can have a significant influence on the probability of detection (POD) and the resultant defect sizing errors [146]. Furthermore, the detectability of volumetric defect features, including the ones used in defect-sensitive modelling, can be affected by the defect type, size, shape and location in the part at any given XCT scan resolution [134,175].

The fine physical features of volumetric defects are often challenging to resolve in limited-resolution XCT scans, which can result in detection failures and errors in their size measurements [142,145,160]. While near-spherical GEPs and KHs, which consist of singular bulky regions, can be relatively reliably detected with reasonable accuracy in the sizing of their features, the loss of information with degrading scan quality is significant in LoFs with thin webbed features [134]. This results in a LoF being detected as multiple smaller entities, separated by a distance equaling the width of the undetected webbings in limited resolution scans. Consequently, the underestimation of the critical defect sizes due to lost information can result in significant overestimation of the fatigue lives of service components when incorporated into defect-sensitive fatigue models. Such non-conservativeness in fatigue life predictions can have severe ramifications in safety critical systems [108,176,177].

One possible solution to address this, as proposed in the authors' previous works, is by interpolating the areas between the bulky regions to represent the undetected webbed regions [134]. To do so, the entities (bulky regions) which should be considered as part of the same defect must first be registered to the defect using a distance-based criterion. The distance can be established by identifying the largest pairwise distances between entities belonging to the same defect and comparing a few critical defects in low resolution scans with their high resolution "ground truth" counterparts. The largest measured distance, from the limited calibration dataset, can then be uniformly applied to all entities in the low resolution scan to determine if they belong to the same defects. While the method requires a small "ground truth" dataset for calibration, once established, the distance criterion can be used for correcting all defect sizes at that given resolution.

The criterion can also be extended to distinguish between internal and surface defects i.e., if the defects are within a threshold distance from the surface, they can be classified as surface defects. In this way, the true size of a large LoF can be estimated by constructing an enveloping polygon of the bounding boxes of the involved entities. The method's relative simplicity, requiring only the cartesian coordinates of the entities' bounding boxes, offers an efficient alternative to more computationally demanding image processing techniques, for determining the effective defect area for fatigue life assessments [134,175,178–180].

This study evaluates the effectiveness of XCT based examinations in assessing the fatigue lives of laser powder bed fused (L-PBF) aluminum (Al) alloys. In the present work, the fatigue data from the authors' previous study was leveraged for the XCT based fatigue assessments (Chapter 3). L-PBF AlSi10Mg and Scalmalloy specimens were XCT scanned prior to fatigue testing to reveal the defect morphologies and their distributions. The critical defects were identified through post-mortem fracture surface analysis and correlated with their representations in the XCT scans. To address the loss of information for certain defect types due to resolution constraints of XCT, a distance-based criterion was implemented to reconstruct the defect geometry for a better representation of the defect sizes. To examine the effects of defect representation, the critical defect information from XCT, before and after applying the distance criterion, is integrated into damage-tolerant fatigue models. This allows assessment of the distance criterion's efficacy in improving the fatigue life estimations for L-PBF Al alloys.

5.2. Material and methods

AlSi10Mg and Scalmalloy bars were fabricated on a Renishaw RenAM500Q laser powder bed fusion system, as part of the author's previous study (Chapter 3). The energy inputs were varied from baseline process parameters to simulate underheated and overheated conditions and intentionally induce different types of AM volumetric defects i.e., LoFs and KHs in addition to the

GEPs, in different sets of specimens [101,102]. For AlSi10Mg, the manufacturer recommended process parameters were used as the baseline: power = 350 W, scan speed = 1800 mm/s, hatch distance = 90 μm and layer thickness = 30 μm. Underheated conditions were simulated by increasing the scan speed by 10% while keeping all other parameters constant. The overheated condition involved increasing the laser power by 20% and decreasing the scan speed by 20% relative to the baseline. For Scalmalloy, the recommended process parameters were not available; instead, the parameters were adopted from literature for the baseline: power = 350 W, scan speed = 1100 mm/s, hatch distance = 90 μm and layer thickness = 30 μm [30,181]. The underheated condition was achieved by increasing the laser power and scan speed by 5% and 10%, respectively. The overheated condition involved an increase of laser power by 5% and a reduction in scan speed by 10% from the baseline (Chapter 3). In addition, different part orientations were examined by fabricating vertical, diagonal and horizontal bars to alter the projection planes of the defects, which had been shown to affect the fatigue criticality of LoFs according to various studies [63,97,108,182]. The following designations were assigned to the specimens to represent the process parameters used during fabrication and the part orientation: underheated vertical (UV), underheated diagonal (UD), underheated horizontal (UH), baseline vertical (BV) and overheated vertical (OV). Post fabrication, the AlSi10Mg specimens were stress relieved at 285°C for 2 hrs and the Scalmalloy specimens at 325°C for 4 hrs. All stress relieved specimens were machined into the fatigue specimen geometry consisting of a gauge diameter of 3 mm and a gauge length of 3 mm. The machined gauge sections of the fatigue specimens were polished using reducing grits of sandpaper to remove any machining grooves and to achieve a smooth surface with $R_a \leq 0.2$ μm. More details of the fabrication, post-processing and testing procedures can be found in Chapter 3.

Within the scope of this work, nineteen AlSi10Mg and fifteen Scalmalloy fatigue specimens were examined via XCT for the NDE-based fatigue assessments. The XCT scans were performed using a Zeiss Xradia 620 Versa system. Prior to scanning, the specimens were carefully marked to register their orientation, which was later used to match the XCT data with the critical defects identified from the fracture surface analysis. More details of the defect registration procedures are illustrated in **Figure 35**. The scans for both materials were performed using a voltage of 60 kV, power of 6.5 W, and a voxel size of 5.3 µm. An objective lens of 0.4X was used, and the transmittance was kept between 30-50% for all scans. After scanning, all XCT projections were reconstructed using the Zeiss Reconstructor software. The reconstructed image stacks were segmented by Otsu thresholding and the binarized images visually compared against the grayscale images to ensure the defect features were adequately captured [183]. Any objects with sizes below 2 voxels were discarded from the analysis to minimize noise. The geometrical and positional properties for the defects were extracted using Dragonfly including the volume, surface area, and bounding box coordinates. A summary of the number of specimens XCT scanned for each condition as part of this study is presented in **Table 7**.

Table 7. The quantities of specimens XCT scanned for each condition as part of this study.

Condition	AlSi10Mg Qty	Scalmalloy Qty
UH	1	3
UD	4	2
UV	7	4
BV	4	3
OV	3	3
Total	19	15

Uniaxial fatigue testing was conducted for all XCT scanned specimens at $R_\sigma = 0.1$ [43]. AlSi10Mg specimens were tested at maximum stresses ranging from 100 to 160 MPa, while the Scalmalloy specimens were tested at maximum stresses ranging from 200 to 300 MPa. The tests were concluded upon fracture and the fracture surfaces were carefully preserved for analysis. Fractography was performed using a Zeiss CrossBeam 550 scanning electron microscope (SEM) to image the fatigue critical defects. Using the markers placed on the specimens, the critical defect information from SEM analysis could be referenced back to the XCT data for defect matching between the two techniques. An illustration of defect registration in fractography and XCT analysis using the reference markers on the specimens is presented in **Figure 35**(a)-(d). In addition, a schematic of the distance-criterion and polygonization approach used in this study to correct for the defect sizes in limited-resolution scans by using the bounding box coordinates extracted from XCT is presented in **Figure 35**(e)-(f).

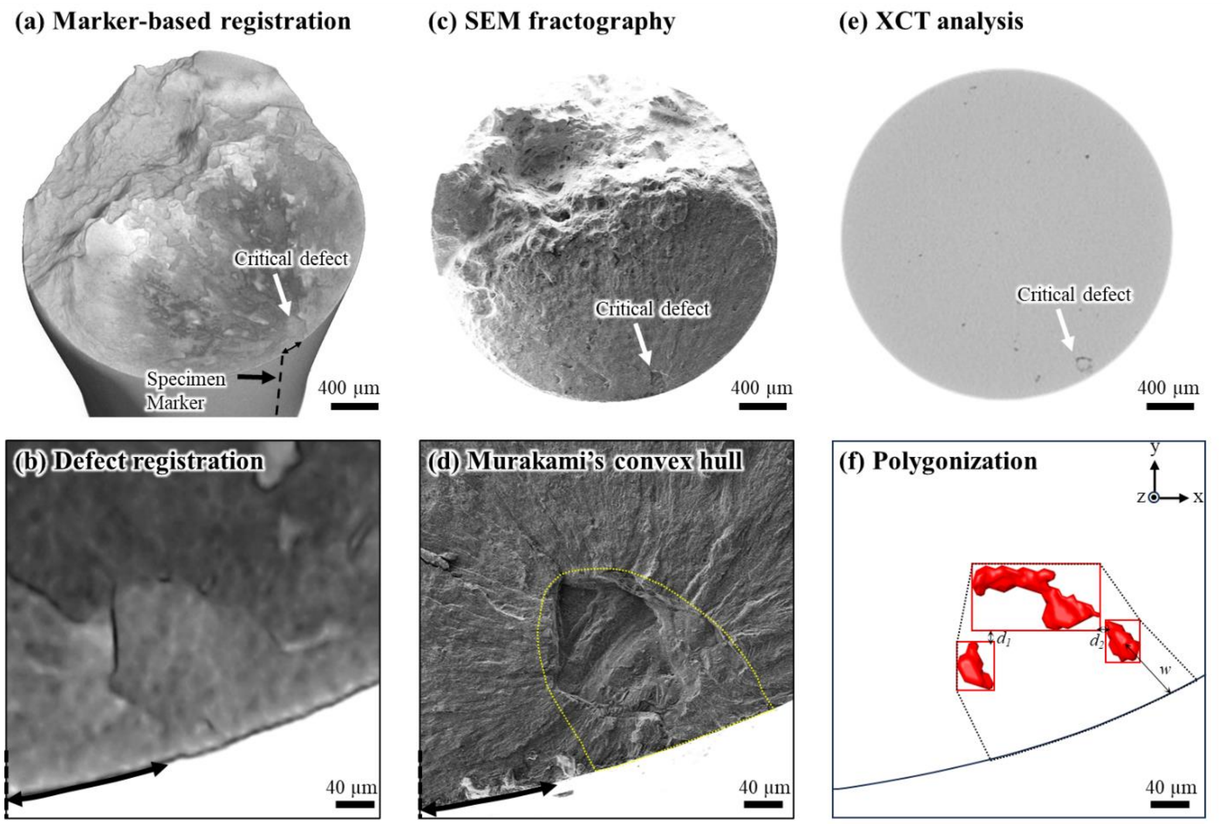

Figure 35. (a)-(b) Identification of critical defects on the fracture surfaces relative to the specimen marker, (c)-(d) SEM fractography and Murakami's convex hull and (e)-(f) distance criterion and polygonization to correct for the defect sizes in limited-resolution XCT data, where d is the distance between the bounding boxes of neighboring entities and w is the distance to the surface.

5.3. Results and discussion

5.3.1. Porosity analysis

The XCT analysis of a select few specimens from various conditions is presented in **Figure 36**. The color bar represents the size of the defects in terms of their projected $\sqrt{area}$ onto the loading plane, i.e., the plane perpendicular to the loading direction. The largest detected defects are also visualized for each specimen in the figure. The OV condition was able to induce near-spherical KHs throughout the bulk of the AlSi10Mg specimens, such as the largest defect shown in **Figure 36**(a) which had a $\sqrt{area}$ = 107 µm. In contrast, the BV, UV, UD and UH specimens mostly contained irregular shaped LoFs, as observed in their largest defects in **Figure 36**(b)-(e).

Numerous large LoFs, which can potentially be fatigue critical, were noted in the BV condition despite the manufacturer recommended parameters being used to fabricate these specimens. While lowering the energy input from the recommended parameters did not result in an increase in the defect size, it increased the defect population in the specimens, with a higher number of large LoFs (i.e., $\sqrt{area}$> 100 μm) being observed in the UV condition. In addition, the directionality of the defects was apparent as the part orientation changed for the UD and UH specimens. The LoFs, which form due to improper bonding between layers, were observed to be oriented perpendicular to the build direction (BD) (indicated using the arrow in **Figure 36**) [184].

For Scalmalloy, the OV condition showed a significant number of large KHs, with the overall porosity being measured as 0.031%. As the energy input was decreased in the BV and UV conditions, no significant differences were observed in the overall porosity. This was likely due to the smaller adjustments made in the process parameters for Scalmalloy, given its narrower processing window for achieving near fully dense parts [104,106]. However, the defect types notably changed between the different conditions. The BV and UV conditions contained irregular shaped LoFs, which were randomly distributed throughout the specimens. Furthermore, the diagonally and horizontally oriented specimens had smaller projected defect sizes, with the largest defects having $\sqrt{area}$ of 91 and 99 μm respectively. In contrast, the vertically oriented specimens exhibited significantly larger $\sqrt{area}$, computed as 179, 137 and 147 μm for the UV, BV and OV conditions, respectively. This was primarily due to large LoFs in the specimens having their longest axes coincide with the projection planes.

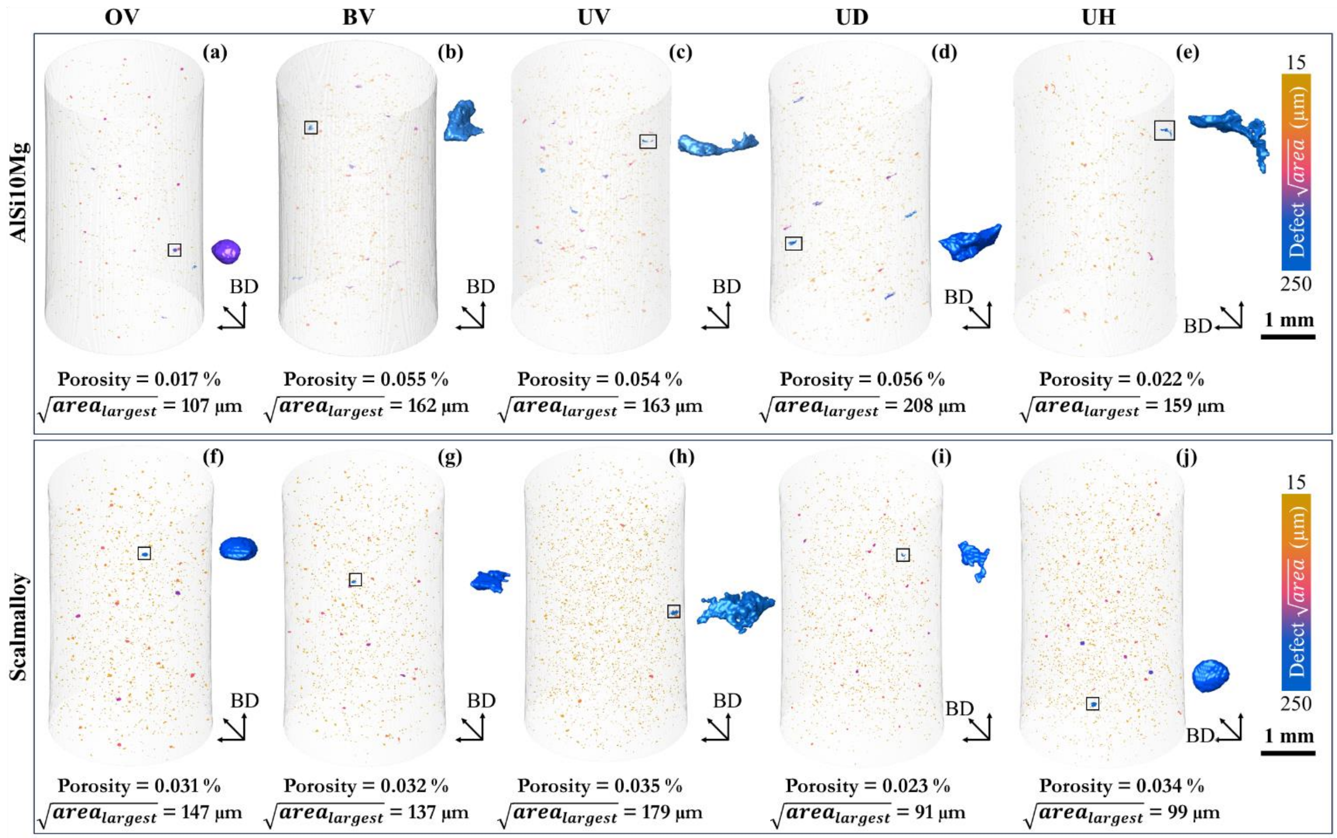

Figure 36. Visualization of volumetric defects detected via XCT of selected specimens in various conditions for (a)-(e) AlSi10Mg and (f)-(j) Scalmalloy. The porosity fraction is reported along with the projected $\sqrt{area}$ of the largest detected defects without applying any corrections.

5.3.2. Identification of critical defects in XCT scans

After XCT scanning, fatigue testing was conducted under uniaxial tension-tension loading at a stress ratio of 0.1. More details of the fatigue testing and results can be found in Chapter 3. All fracture surfaces were analyzed by scanning electron microscopy (SEM) to obtain the "ground truth" graphical information, in two-dimension of the critical defect. This ground truth information was used for identifying the critical defects in the XCT scans by considering their morphological features and location relative to the markers on the specimens (see **Figure 35**(a)-(d)) [185]. Some representative fatigue fracture surfaces are presented in **Figure 37**, showing the critical defects observed at the fracture origins alongside their appearance in the XCT scans performed prior to fatigue testing.

In all AlSi10Mg specimens, crack initiation occurred from either near-surface or surface connected volumetric defects. It should be noted that Murakami's $\sqrt{area}$ parameter was used to measure the size of the defects from the fracture surfaces in the SEM analysis using the projected area of the defect [92]. If the defects were near surface (with $\sqrt{area}$>distance to the free surface), the ligament between the defect and surface was considered in the area computation by connecting the defect to the surface (see **Figure 35** (d)). In most cases, the crack initiating defects in AlSi10Mg were LoFs, such as the ones seen in **Figure 37**(a)-(e). While the entirety of some LoFs could be captured in XCT scans (see **Figure 37**(a)), in other cases, the critical LoFs appeared to dissociate into multiple smaller entities (see **Figure 37**(b)-(e)). This was attributed to the coarser bulky regions of the LoFs being easier to resolve in XCT compared to the fine webbed regions which could not be detected reliably [151,152]. In these instances, the largest detected entity at the corresponding location was typically treated as the critical defect by the existing, prevailing practices in the absence of ground truth fracture surface information [186,187].

In contrast, the critical defects in Scalmalloy specimens exhibited much simpler morphologies consisting of singular bulky regions, with webbed features seldom observed. This resulted in the detected defect morphologies from XCT scans to resemble those obtained from the fracture surface analysis. Although XCT reliably detected these defects, some of them appeared to be separated from the surface despite fractography revealing them as being surface-connected. This apparent gap should be considered for fatigue criticality assessments as noted by Murakami [92]. The loss of information in the webbed regions for LoFs necessitated corrections to XCT data of both materials for improving sizing estimations for fatigue life assessments. The distance criterion, as proposed in the authors' previous work, along with Murakami's surface interaction, was implemented. The distance was calibrated in the author's previous study for a few acquisition parameters of lower resolution using a set of high resolution data treated as ground truth [134]. For the scan parameters utilized in this study, any neighboring entities within a threshold distance, d, of 60 μm were combined by constructing a polygon using their bounding box coordinates (see **Figure 35**(f)). In addition, if the $\sqrt{area}$ of the entities was larger than their distance to the surface, w, the polygon was connected to the surface and considered as a surface defect [92,134]. If the $\sqrt{area}$ of the defect was smaller than its distance to the surface, it was treated as an internal defect. Using the distance criterion, the areas between the bulky entities and the surface (if classified as surface defects) could be accounted for and the defect geometry could be reconstructed through polygonization procedure considering a larger, representative stressed area under cyclic loading [188]. It is important to note that while high-resolution XCT data was used to determine the distance thresholds in this study, limited 2D fracture surface information may also serve as the "ground truth" to establish the distance criterion from the critical defects, when high resolution XCT datasets are unavailable.

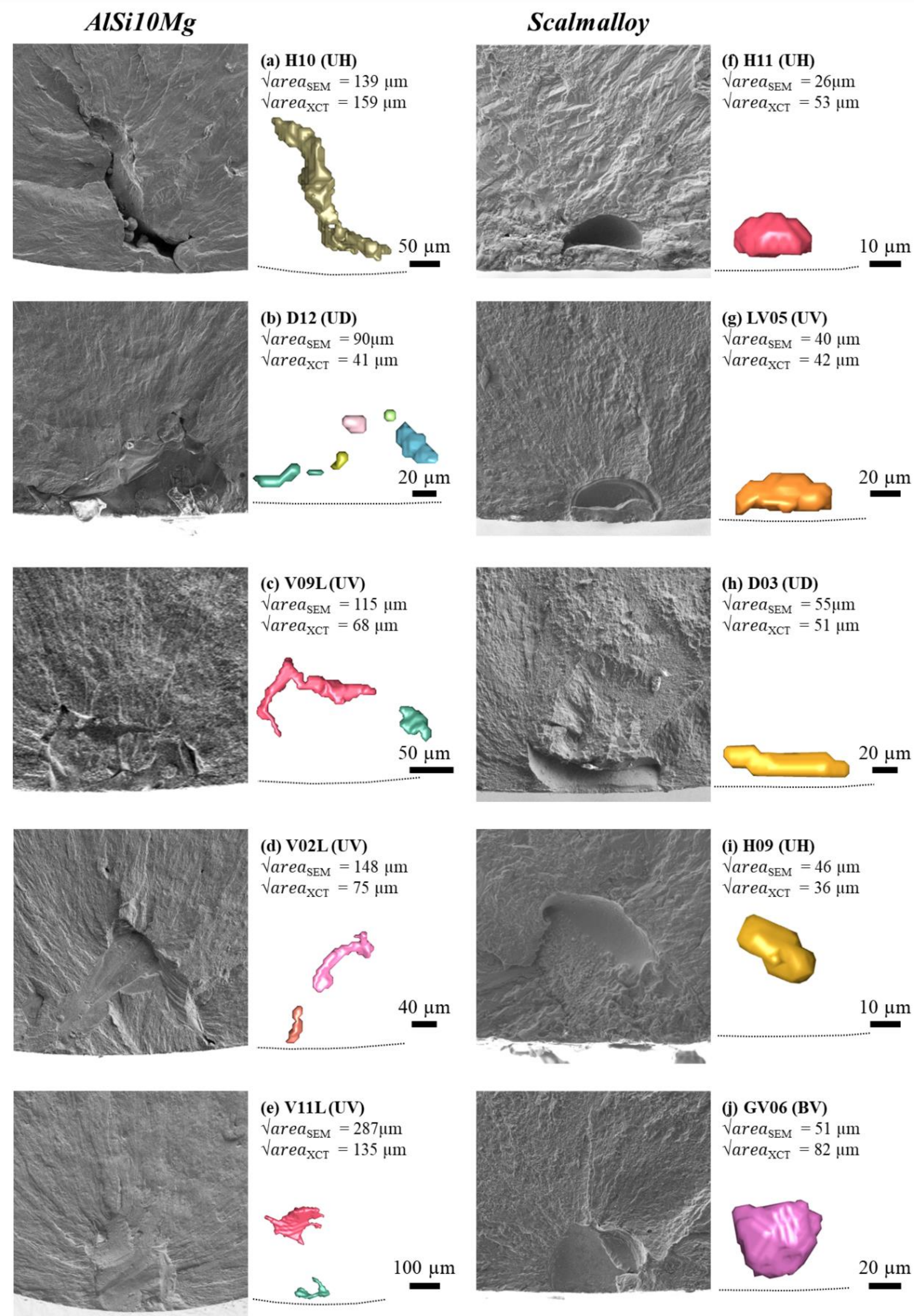

Figure 37. SEM images of the critical defects at the fracture origins and their appearance in XCT scans conducted prior to fatigue testing for (a)-(e) AlSi10Mg and (f)-(j) Scalmalloy specimens.

5.3.3. Quantification of critical defect size

The XCT vs. SEM $\sqrt{area}$ for all fatigue critical defects are presented in **Figure 38**. The $\sqrt{area}$ of the entity detected in the XCT scans corresponding to the critical defect, referred to as "Critical" from here on, vs. their SEM $\sqrt{area}$ are presented in **Figure 38**(a) and (c) for AlSi10Mg and Scalmalloy, respectively. Here, if there are multiple entities detected for a defect, the $\sqrt{area}$ of only the largest one is calculated for the figure. In addition, the defects visualized in **Figure 37** are marked with arrows in **Figure 38**(a) to understand the implications of the loss in information. Considering the defect information from SEM analysis as the ground truth, the largest errors were observed in the XCT measurements of LoF defects with two or more bulky features connected by thin webbed regions (see orange datapoints in **Figure 38**(a)). In contrast, the errors were less severe for defects consisting of a singular bulky region, shown by the black hollow markers for both AlSi10Mg and Scalmalloy in **Figure 38**(a) and (c).

The $\sqrt{area}$ of the critical defects after applying the distance criterion and polygonization approach, referred to as "Polygonization Critical" from here onwards, are plotted against the SEM $\sqrt{area}$ in **Figure 38**(b) and (d) for AlSi10Mg and Scalmalloy, respectively. There was a significant improvement observed in the sizing estimates of the webbed/bulky LoFs (orange markers in **Figure 38**(b)), which shifted closer to the 1:1 identity line. Furthermore, applying the polygonization approach resulted in the $\sqrt{area}$ of a significant number of singular bulky defects (black hollow markers) to shift above the identity line. In fact, 85% of the specimens had critical defect sizes that were slightly overestimated, which can be attributed to the polygonization approach being an approximation based on the bounding boxes of the neighboring defects/entities and their relative distance to the surface, as shown in **Figure 35**(f). In comparison, the SEM $\sqrt{area}$ measured from the fracture surfaces were calculated by constructing a convex hull tracing the contours of the defects (**Figure 35**(d)), which resulted in a smaller $\sqrt{area}$ compared to the XCT $\sqrt{area}$, which was approximated based on the bounding boxes of the detected individuals (**Figure 35**(f)) [182,189]. Nonetheless, the polygonization method provided a simplistic and practical approach to better estimate the defect sizes in XCT data.

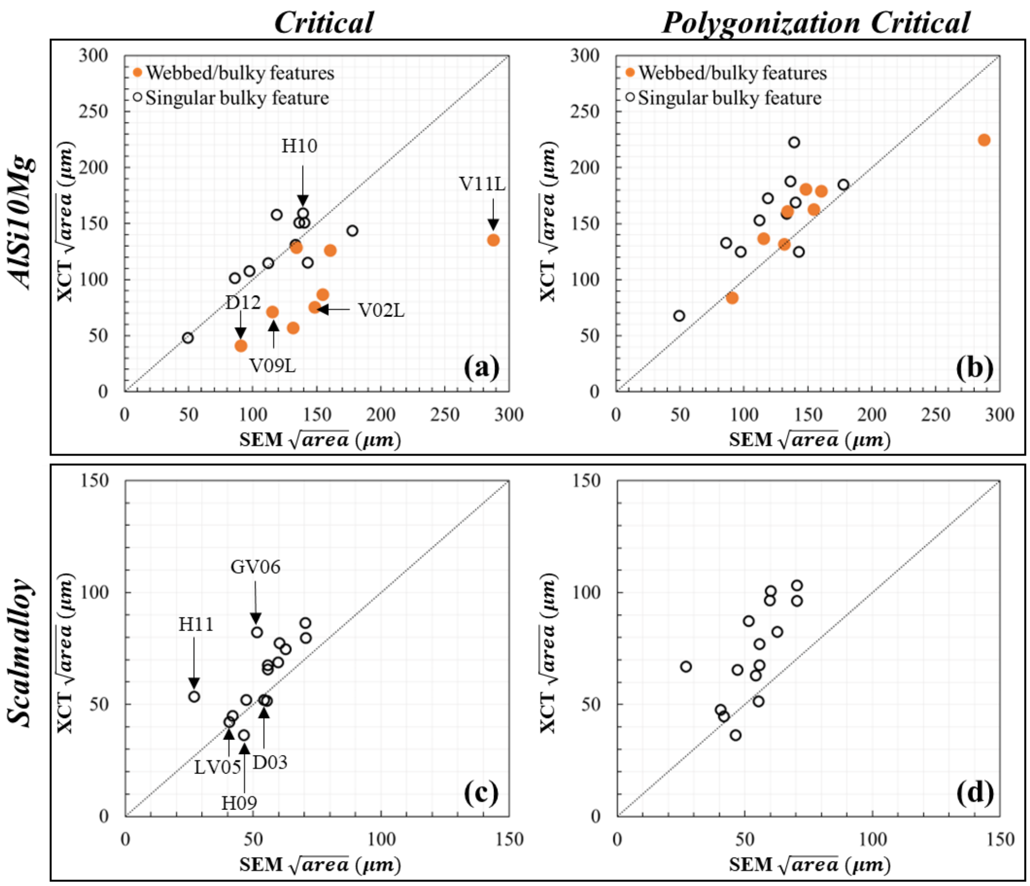

Figure 38. Measured projected $\sqrt{area}$ from XCT before and after applying polygonization correction vs. ground truth $\sqrt{area}$ from SEM analysis of fracture surfaces for (a)-(b) AlSi10Mg and (c)-(d) Scalmalloy.

Since the actual critical defects would not be known in NDE based fatigue assessments, fatigue life predictions were made for the known critical defects before and after applying the polygonization procedure (Critical and Polygonization Critical), as well as for the largest surface defect in the specimen as detected by XCT after applying polygonization, referred to as "Polygonization Largest" from hereon. The Polygonization Critical and the Polygonization

Largest defects are visualized for AlSi10Mg and Scalmalloy specimens in **Figure 39**. It should be noted that the color code represents the $\sqrt{area}$ of the defects.

While the Polygonization Largest defect was correctly predicted to be fatigue critical in some cases for AlSi10Mg (see **Figure 39**(a) and (e)), some differences between the largest and actual critical defects were noticed for other specimens. This is attributed to the location of defects relative to the neighboring defects/surface and the number of bulky regions detected in the XCT scans which can introduce some variability in the size measurements depending on the distance criterion [190,191]. For example, the Polygonization Critical defect in **Figure 39**(b) comprised a complex shaped, surface-connected bulky region and a small globular entity, for which the polygonization procedure yielded a $\sqrt{area}$ value of 161 μm. For this defect, there was little ambiguity in the size since most of the defect morphology was retained within the larger entity. In contrast, the Polygonization Largest defect for this specimen consisted of 3 smaller sub-surface bulky regions with large spacings between them and the surface. However, since these entities were within the threshold distances from each other and from the surface, they were registered as a surface defect with $\sqrt{area}$ = 190 μm.

The Polygonization Largest defects were not always accurately predicted to be critical for the selected Scalmalloy specimens presented in **Figure 39**(f)-(j). However, in all cases, the Polygonization Largest $\sqrt{area}$ were in close agreement with the Polygonization Critical $\sqrt{area}$. Since the critical defects in the Scalmalloy dataset were smaller in comparison to AlSi10Mg and only consisted of a singular bulky region, with no webbed features, they were reliably captured in the XCT scans. This was also seen in the XCT vs. SEM $\sqrt{area}$ analysis presented earlier in **Figure 38**, where the errors were significantly less pronounced for the Scalmalloy defects compared to the complex shaped defects found in AlSi10Mg. Thus, the discrepancies between Polygonization

Critical and Polygonization Largest defects can be ascribed to shape-related defect features not considered in this analysis, which may also influence the defect criticality. Nonetheless, $\sqrt{area}$ remained a strong indicator of criticality. Despite the specimen-to-specimen variability in defect populations, all crack initiating defects for both AlSi10Mg and Scalmalloy were within the top 10 most critical defects among thousands of defects detected by XCT as ranked by their $\sqrt{area}$ after applying the polygonization approach.

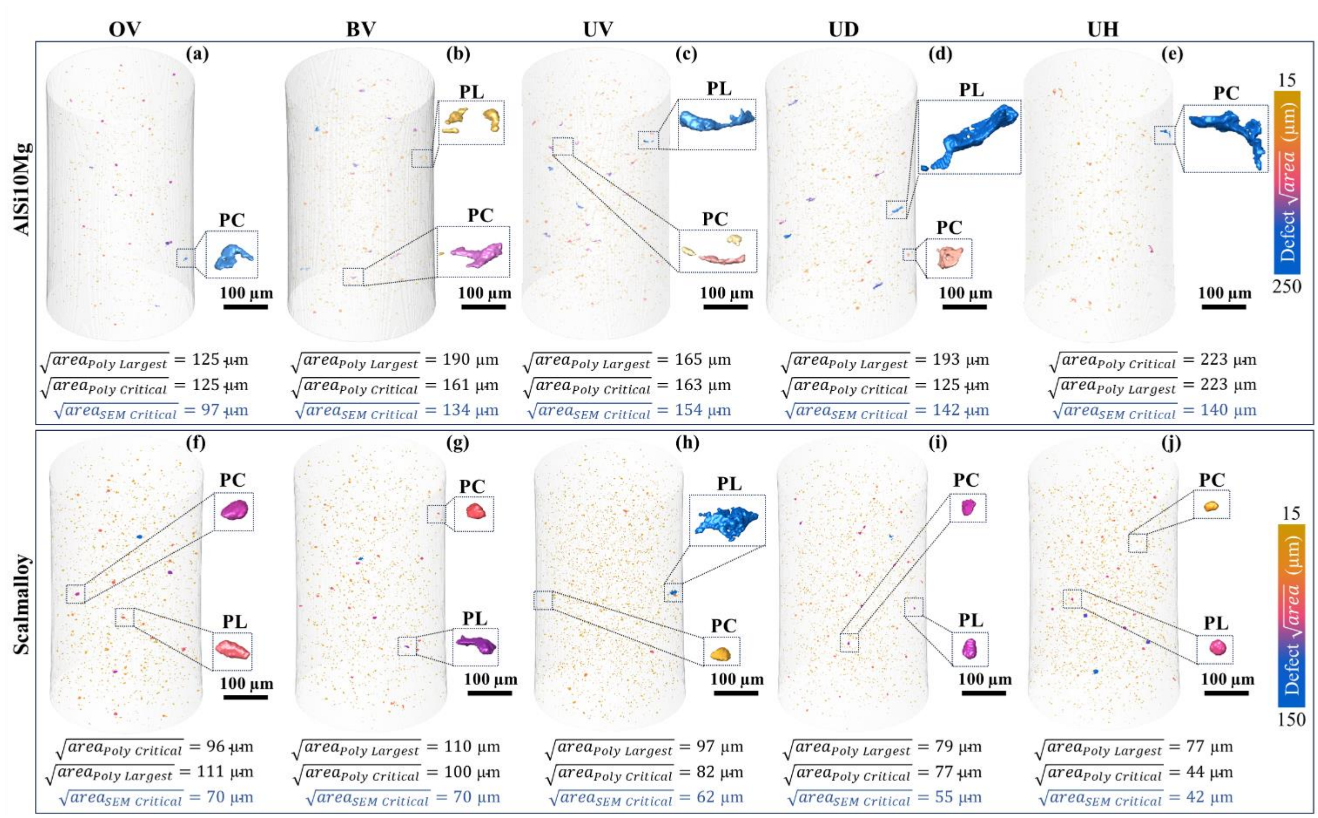

Figure 39. Visualization of the Polygonization Critical (PC) and Polygonization Largest (PL) defects in XCT scans of (a)-(e) AlSi10Mg and (f)-(j) Scalmalloy specimens. The $\sqrt{area}$ for the PC, PL, and the corresponding SEM Critical defects (reported in blue text) are also listed.

5.3.4. Fatigue life estimations

Using the critical defect information obtained from the XCT scans, the fatigue lives of AlSi10Mg and Scalmalloy were assessed; and the outcomes of such assessment without and with corrections by the polygonization approach were compared. The fatigue lives of L-PBF AlSi10Mg and Scalmalloy can be sufficiently described using crack growth-based Shiozawa model according to the author's previous work (Chapter 3). The Shiozawa equation, which focuses solely on crack growth behavior, was used to estimate the fatigue lives for both alloys, which is defined as [129,192]:

$$N_f = \sqrt{area} \cdot \left(\frac{\Delta\sigma \cdot Y \cdot \sqrt{\pi \cdot \sqrt{area}}}{K_f'}\right)^{-\frac{1}{d'}} \qquad (5.1)$$

where N_f is the number of cycles to failure, $\Delta\sigma$ is the stress range, Y is the stress intensity geometric factor, and K_f' and d' are the Shiozawa fitting parameters. The parameters were obtained by fitting power curves to the fatigue data generated in the author's previous study for AlSi10Mg and Scalmalloy. It should be noted that the data for specimens which underwent XCT scanning as part of this study were excluded from the fitting procedures. In addition, any data exceeding $\frac{N_f}{\sqrt{area}}$ of 10^{10} cycles/m   were not included because they correspond to data in the fatigue limit region that cannot be described by Shiozawa's model.

The predicted fatigue lives obtained using the Shiozawa model based on the XCT scans are plotted against the experimental lives by considering different measures of the $\sqrt{area}$ parameter in **Figure 40**. The measures included the Critical $\sqrt{area}$, the Polygonization Critical $\sqrt{area}$ considering all corresponding entities after applying the polygonization approach for size calculation only, and the Polygonization Largest $\sqrt{area}$ considering the largest surface defect after applying the polygonization procedure. The fatigue life assessment using the Critical $\sqrt{area}$ of AlSi10Mg resulted in specimens with webbed/bulky critical defect features to fall outside scatter bands of 3, as seen in **Figure 40**(a). These defects also had the largest errors in their XCT $\sqrt{area}$ measurements as seen in **Figure 38**. After applying the corrections and using Polygonization Critical $\sqrt{area}$, all datapoints fell within a scatter band of ±3 or, if outside, were on the conservative side of the predictions. Moreover, using the Polygonization Largest size resulted in further conservativeness in the predictions, with all data again falling within scatter band of ±3 or below the lower bounds.

Since the critical defect sizes for Scalmalloy had small errors due to them mostly consisting of singular bulky regions, 93% of the predictions made using the Critical $\sqrt{area}$ provided fatigue lives within a scatter band of 3. Incorporating Polygonization Critical $\sqrt{area}$ yielded more conservative estimations, with 73% of the predictions lying below the 1:1 identity line. Finally, using the Polygonization Largest $\sqrt{area}$ in the Shiozawa model appeared to further shift the datapoints slightly towards conservative side of experimental lives.

In summary, the use of the Polygonization Critical and Polygonization Largest $\sqrt{area}$ as inputs to the Shiozawa model provided acceptable predictions for fatigue lives of L-PBF AlSi10Mg and Scalmalloy. By leveraging XCT-based critical defect information and refining defect size estimates through the polygonization approach, predictions were brought within acceptable scatter, mostly on the conservative side. This highlighted the importance of integrating corrected $\sqrt{area}$ in crack growth-based models to enhance the accuracy and reliability of fatigue life assessments in AM Al alloys.

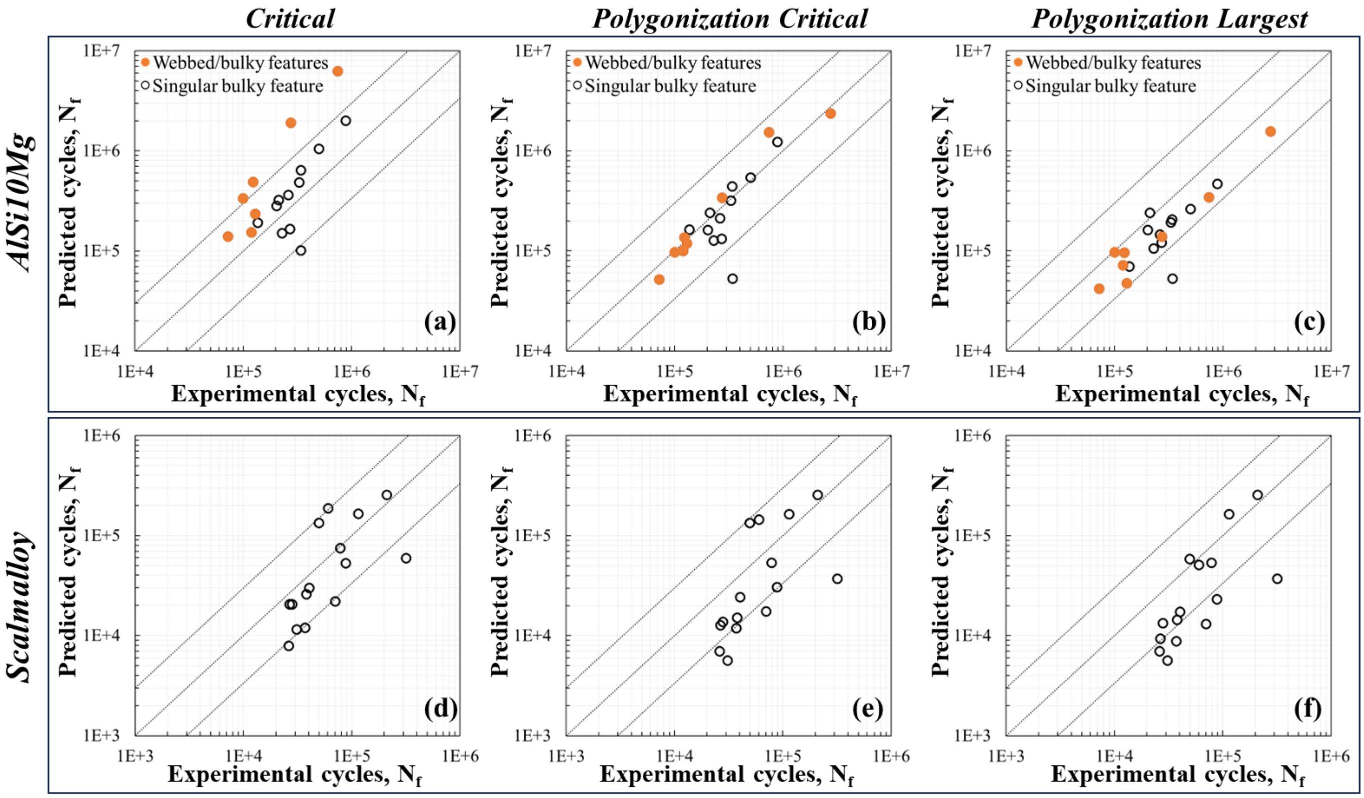

Figure 40. Shiozawa fatigue life predictions based on the XCT scans incorporating the Critical, Polygonization Critical, and the Polygonization Largest $\sqrt{area}$ for (a)-(c) AlSi10Mg and (d)-(f) Scalmalloy.

5.4. Conclusions

In this study, the effectiveness of XCT based examinations in assessing the fatigue lives of L-PBF aluminum alloys was investigated. AlSi10Mg and Scalmalloy specimens with varying defect populations were examined by XCT and their fatigue data analyzed. Post-fracture surface analysis in conjunction with the XCT scans enabled the identification of critical defect size measures, including the Critical, Polygonization Critical and Polygonization Largest $\sqrt{area}$, which were used to establish fatigue life correlations. The following conclusions can be drawn from the results:

1. There is an inherent loss of information in XCT data for large fatigue critical LoFs compared to bulky shaped defects, particularly in their thinner webbed regions. This

results in the LoFs being detected as multiple entities with reduced $\sqrt{area}$s than what is observed on the fatigue fracture surfaces.

2. Approaches that only utilize the largest detected entities from XCT scans in damage-tolerant models result in non-conservative fatigue life estimations. This is due to the loss of critical information for large LoFs with complex morphologies.

3. The limitations in XCT data can be remediated by applying a distance criterion. This allows for the defect geometry to be reconstructed for LoFs to more closely reflect the defect sizes measured from the fracture surfaces. By incorporating corrected XCT data, accurate, moderately conservative NDE-based fatigue life assessments can be achieved for L-PBF aluminum alloys.

6. Summary and potential future work

The overall goal of this dissertation was to investigate the influence of volumetric defects on the fatigue properties of AM Al alloys. This chapter provides a summary of the four studies presented in the preceding chapters (Chapters 2 to 5), highlighting how they contribute to the research goal and address the objectives of this dissertation.

In Chapter 2, the structure-property relationships for L-PBF AlSi10Mg were investigated. Various solutionizing and aging heat treatments were performed to alter the microstructures and examine their effects on the mechanical properties. While the heat-treatments appeared to strongly affect the tensile properties, the strain-life and stress-life fatigue behavior for the various conditions contained considerable overlap. Fracture surface analysis revealed that tensile failure originated from bulky Si particles debonding from the α-Al matrix. The size of these particles varied with heat treatment, influencing the resultant tensile properties since they served as strengthening precipitates and void nucleation sites. However, fatigue cracks were always observed to initiate from surface volumetric defects in all heat-treated conditions. The size of the critical volumetric defects was strongly correlated to the fatigue lives regardless of the microstructural differences. The findings of this study signified the defect-sensitive nature of Al alloys, underscoring the need to examine critical defect features to describe the fatigue behavior.

In Chapter 3, the fatigue-defect criticality relationships were investigated for AlSi10Mg and Scalmalloy, two Al alloys with different microstructures, and thus, defect-sensitivities. By altering the process parameters and part orientation during fabrication, volumetric defects of varying characteristics were induced at reasonable populations for a systematic examination of their influence on the fatigue behavior. It was found that while there is significant scatter in the stress-life data for AlSi10Mg, incorporating the critical defect sizes in fatigue-notch factor based approaches provide reasonable fatigue life estimations. However, the bimodal grain structure of

Scalmalloy introduced uncertainty in the crack initiating feature measurements and influenced the fatigue behavior in the threshold regime, resulting in poor life predictions. It was noted that despite these differences, the crack-growth rates of both alloys were similar. Fatigue design curves obtained using crack-growth based Shiozawa model along with the fatigue limit from the El-Haddad model, could sufficiently describe the fatigue behavior for both L-PBF Al alloys.

While Chapters 2 and 3 underscored the importance of accurately characterizing the defect features and their distribution to understand the fatigue behavior in defect-sensitive L-PBF Al alloys, Chapter 4 evaluated the effectiveness of XCT scans obtained at varying resolutions for non-destructive identification and characterization of critical defects. Various XCT scan parameters were examined at different combinations of voxel size and coupon geometry. The selection of voxel and coupon sizes were made considering the practical constraints with large format industrial use XCT scans which can suffer from a tradeoff between resolution and scanned volume. By treating the highest resolution scan as the "ground truth", the POD of defects was quantified for the different scan parameters in terms of the defect size. It was found that the defect type plays an important role in determining the POD, and large LoFs are more susceptible to loss of information and sizing inaccuracies compared to spherical defects. A framework was proposed for recovering critical defect information from low resolution XCT scans. The relative simplicity of the correction procedure, which used a distance criterion for reconstruction of defects by polygonization, enabled rapid characterization of low-resolution XCT data with high throughput.

In Chapter 5, the fatigue data from Chapter 3 was leveraged for evaluating the effectiveness of XCT based examinations in fatigue life assessments of AM parts. Specimens were XCT scanned prior to fatigue testing and the critical defects were identified within the scans by correlating with the post-mortem fracture surface information. The XCT representations of the critical defects were prone to significant loss of information, which resulted in severe underestimation of their sizes and in some cases, detection failures. The $\sqrt{area}$ measured from XCT was incorporated in crack-growth based models which resulted in non-conservative fatigue life predictions. To recover critical defect information from the limited resolution XCT scans, the defect reconstruction algorithm developed in Chapter 4 was implemented, which allowed for accurate and moderately conservative fatigue life assessments.

The three main objectives of this dissertation have been accomplished through the four research projects presented. The first objective aimed to identify the critical features influencing the fatigue properties of AM Al alloys. Under this objective, it was hypothesized that the fatigue behavior becomes more sensitive to the presence of defects as the ultimate tensile strength increases. It was shown that while the fatigue behavior may be influenced by microstructures to some extent, large volumetric defects remain the dominant factor governing the fatigue lives. Instead, the microstructure played a pivotal role in near-threshold fatigue behavior, when comparing Al alloys with varying microstructural characteristics and corresponding defect sensitivities. While the fatigue behavior could be sufficiently described by considering the size and location of the defects in fine-grained AlSi10Mg, examination of the Scalmalloy specimens revealed that in bimodal grain structures, crack initiation is dictated by complex interactions between the microstructure and defects. Due to this, the uncertainty in determining the crack initiation features resulted in fatigue life predictions to be non-conservative. However, it was noted that the crack growth behavior was similar for both alloys and the fatigue design curves generated using the unified approach of combing crack-growth based and fatigue limit threshold equations allowed for the fatigue behavior to be reasonably described.

The second objective was to assess the impact of XCT acquisitions parameters on the probability of detection of critical AM defects. This was achieved by determining the POD of defects by considering various scan parameters commonly understood to be important including x-ray tube voltage, source-to-sample-to-detector distances, voxel size and coupon geometry. It was hypothesized that the POD of a spherical defect of a given size is higher than for an irregular defect, which was verified by the one-to-one comparisons of defects in limited resolution scans against a higher resolution ground truth scan. Moreover, the sizing accuracy of irregular shaped defects was found to deteriorate more significantly with worsening imaging conditions than for spherical defects. By studying the characteristics of the defects detected in low resolution, the proposed distance criterion-based polygonization correction was shown to be effective in improving the sizing estimations for irregular defects.

The third objective was to evaluate the effectiveness of NDE in assessing the fatigue lives of AM Al alloys. It was hypothesized that the fatigue criticality of defects could not be adequately defined in low resolution XCT data due to significant errors in measuring the critical features. By performing XCT scans and fatigue testing on AlSi10Mg and Scalmalloy specimens, the fatigue critical defects were identified from the fracture surfaces and correlated with their representations in the XCT scans. The methodology developed under objective two for correcting the defect sizes in limited-resolution XCT scans was implemented, enabling more accurate and conservative size estimations. Fatigue life predictions based on uncorrected defect sizes failed to capture defect criticality, resulting in severe underestimation. In contrast, predictions based on corrected defect sizes successfully reflected defect criticality in some cases and yielded accurate, conservative fatigue life estimates for all specimens, ultimately disproving the initial hypothesis.

Overall, the findings of this study can enhance our understanding of critical volumetric defect features and their influence on the fatigue lives of AM Al alloys. The micro-/defect structure property correlations established in this study can accelerate the qualification and certification of parts in fatigue critical applications, supporting the broader adoption of AM technologies across various industries. The methods developed for improving the current practices in non-destructive evaluation of AM parts can significantly reduce the time and costs associated with traditional destructive examination approaches. Furthermore, the framework developed in this dissertation for NDE based fatigue life estimations of Al alloys enables accurate assessments of the fatigue behavior using limited-resolution XCT, including those from large format XCT scans. This potentially facilitates high-throughput, non-destructive qualification of functional AM parts in large-scale production environments.

This work provided the foundation to better understand the micro-/defect structure-property relationships in AM Al alloys via destructive and non-destructive methods. As a natural progression, future studies can focus on specific aspects of the concepts explored in this dissertation. For example, while the present work demonstrated that critical defects can be identified and the fatigue behavior can be described using the size and location of volumetric defects, XCT data can be leveraged to extract additional critical defect features in 3D. These features can provide a more comprehensive understanding of the fatigue crack initiation mechanisms by exploring their correlation to the fatigue properties of AM parts. Furthermore, although the polygonization method proposed in this study is a simple approximation of the ground truth, other advanced segmentation methods can be studied to extract critical defect information from low-resolution XCT data. The knowledge from such future studies can be used to improve defect characterization accuracy, enhance fatigue life predictions and inform qualification criteria for AM components.

7. Supplemental Materials

Table S1. Heat treatment procedures applied to the L-PBF AlSi10Mg specimens.

Solution Treatment (T4)/ Stress Relieving (SR)			**Natural Aging (NA)**		**Artificial Aging (T6/T7)**			**Designation**	**Mechanical Testing**
Temp (°C)	Time (hr)	Cooling	Temp (°C)	Time (hr)	Temp (°C)	Time (hr)	Cooling		
300	2	Air	Room	96	None			*SR-300-NA*	*Tensile/Fatigue*
425	24	Water	Room	96	None			*T4-425-NA*	*Tensile/Fatigue*
425	24	Water	Room	96	165	7	Air	*T6-425-165*	*None*
425	24	Water	Room	96	165	16	Air	*T7-425-165*	*Tensile*
475	24	Water	Room	96	None			*T4-475-NA*	*Tensile*
475	24	Water	Room	96	165	7	Air	*T6-475-165*	*None*
475	24	Water	Room	96	165	16	Air	*T7-475-165*	*Tensile/Fatigue*
525	24	Water	Room	96	None			*T4-525-NA*	*Tensile/Fatigue*
525	24	Water	Room	96	165	7	Air	*T6-525-165*	*None*
525	24	Water	Room	96	165	16	Air	*T7-525-165*	*Tensile*

The sphericity vs. equivalent sphere diameter and sphericity vs. $\sqrt{\text{area}}$ plots for the ground truth dataset are presented in **Figures S1(a)-(b)**. The larger defects in the specimen had lower sphericity values and were LoF defects, compared to smaller keyhole and entrapped gas pores which had sphericity values closer to 1. In addition, a single feature may not be adequate to distinguish between the various types of defects. This was evident in the equivalent sphere diameter vs. $\sqrt{\text{area}}$ plot in **Figure S1(c)**, where there were several larger defects which had similar equivalent sphere diameters but very different $\sqrt{\text{area}}$ values, which was ascribed to their dissimilar morphologies

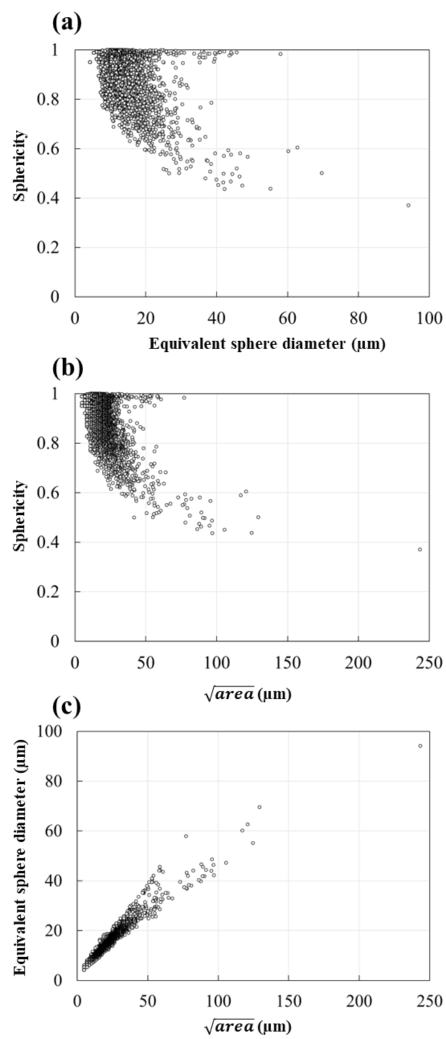

Figure S1. (a) Sphericity vs. equivalent sphere diameter, (b) sphericity vs. $\sqrt{area}$ and (c) equivalent sphere diameter vs. $\sqrt{area}$ for the *3 µm-3 mm* ground truth XCT data

The sphericity vs. $\sqrt{\text{area}}$ plots for the *3 μm-3 mm*, *6 μm-3 mm* and *10 μm-3 mm* scans are presented in **Figure S2**. The plots revealed that the acquisition parameters used for the XCT scans have a notable impact on the detected features. In the ground truth dataset in **Figure S2(a)**, the larger defects exhibit lower sphericity values, while the smaller defects display more spherical morphologies. When the voxel size was increased to 6 μm, both size and sphericity measurements were affected, with the defect distribution shifting upwards and leftwards, implying the sizes for the same defects were measured to be smaller with higher sphericities compared to the ground truth dataset, as seen in **Figure S2(b)**. Further increasing the voxel size to 10 μm amplified these discrepancies, as seen in **Figure S2(c),** resulting in even smaller measured sizes and higher sphericities for the same defects.

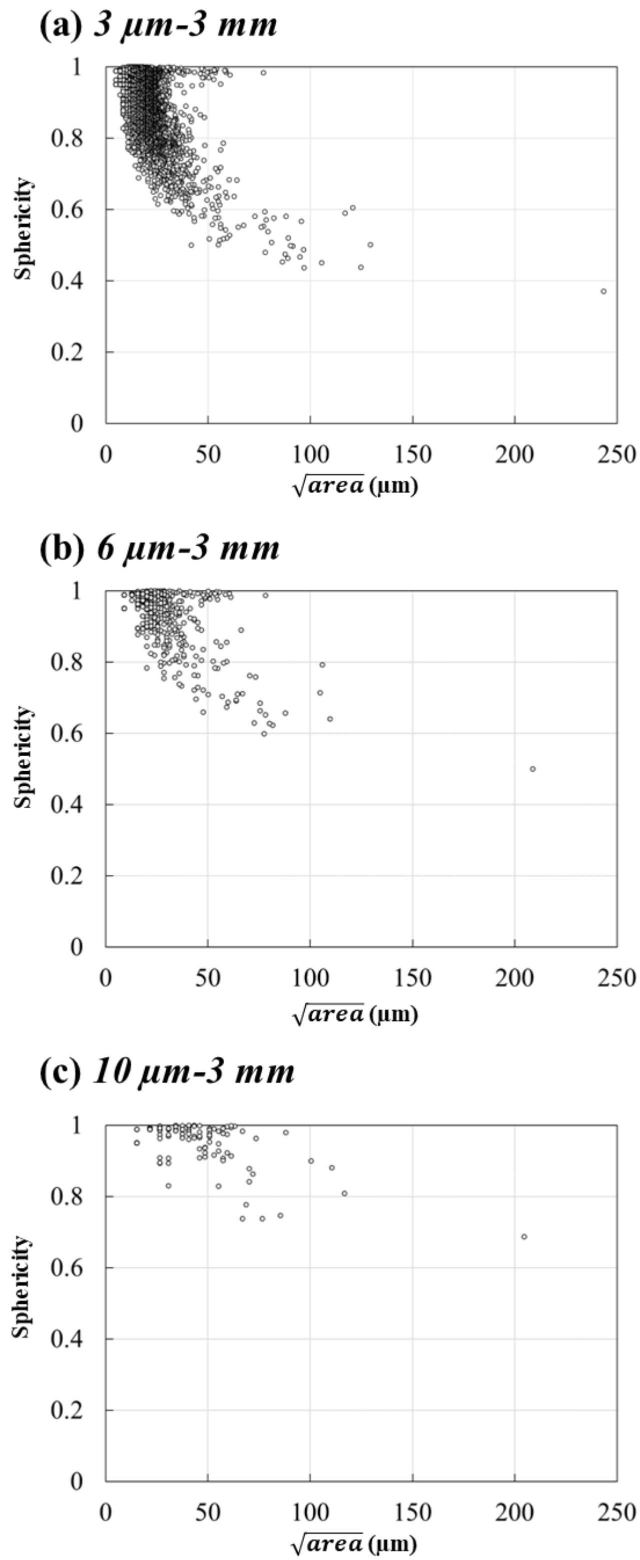

Figure S2. Sphericity vs. $\sqrt{area}$ for the (a) *3 µm-3 mm* (ground truth), (b) *6 µm-3 mm* and (c) *10 µm-3 mm* scans.

The 50% POD, 90% POD at a confidence level of 95%, as well as the largest undetected and smallest detected defect sizes for all scan parameters investigated in this study are reported in **Table S2**. The table includes these values for when considering all defects indiscriminately, as well as for the defects classified as LoF (consisting of defects with sphericity≤0.7) and near-spherical (sphericity>0.7). .

Table S2. The defect sizes for 50% POD (a_{50}), 90% POD at a confidence level of 95% ($a_{90/95}$), the largest undetected defect (a_{LU}) and the smallest detected defect (a_{SD}).

Scan parameter	Defect type	a_{50} (µm)	$a_{90/95}$ (µm)	a_{LU} (µm)	a_{SD} (µm)
6 µm-3 mm	All	26	33	53	20
	LoF	33	48	53	28
	Near-spherical	25	30	35	20
10 µm-3 mm	All	47	62	77	29
	LoF	59	82	77	40
	Near-spherical	38	47	44	29
6 µm-6 mm	All	28	35	53	18
	LoF	37	49	53	30
	Near-spherical	26	31	37	18
10 µm-6 mm	All	47	62	77	32
	LoF	60	84	77	40
	Near-spherical	38	46	44	32
6 µm-10 mm	All	41	54	79	24
	LoF	55	81	79	34
	Near-spherical	34	41	44	24
10 µm-10 mm	All	70	98	95	37
	LoF	87	129	95	50

	Near-spherical	47	58	56	37

The hit/miss data for the POD analysis using a decision threshold of $\sqrt{\text{area}} \geq 2$ and $\sqrt{\text{area}} \geq 3$ voxels are presented in **Figure S3**. While increasing the noise threshold, i.e., from $\sqrt{\text{area}} \geq 2$ to $\sqrt{\text{area}} \geq 3$, seemed to have shifted the curves rightwards for all voxel/specimen sizes, the overall trend remained consistent regardless of the threshold applied.

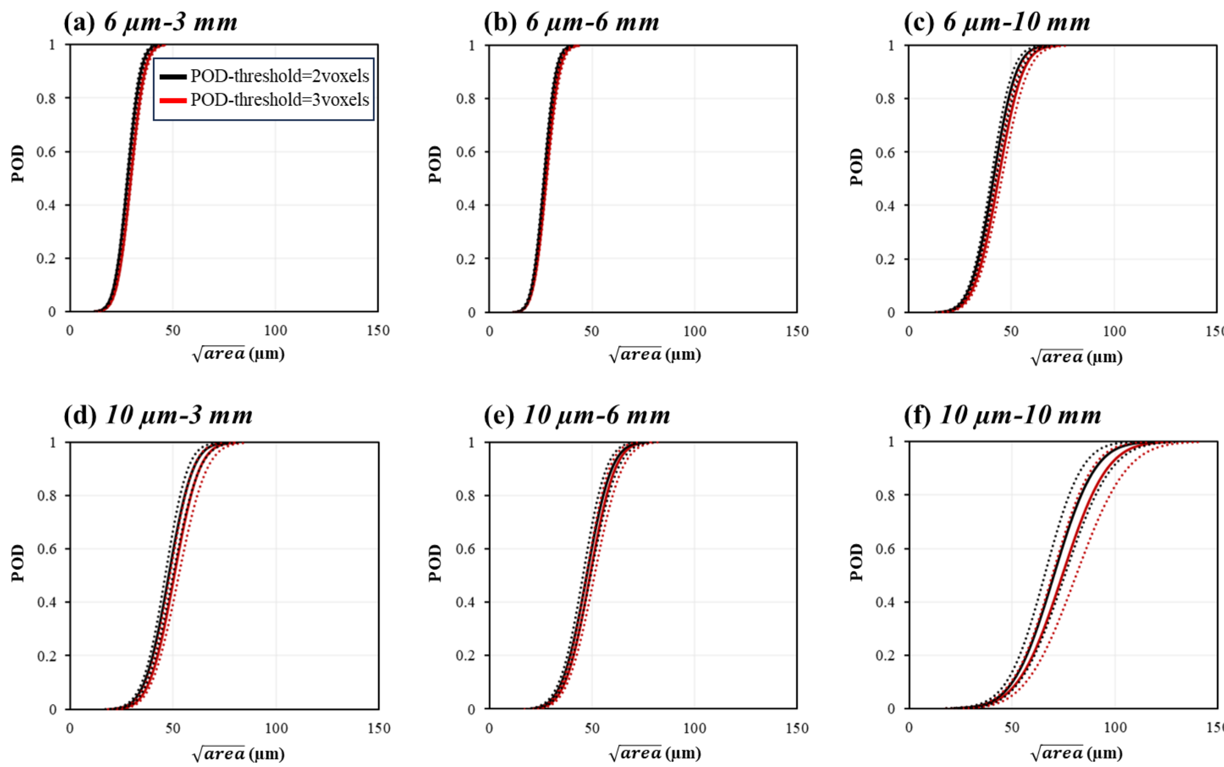

Figure S3. Comparison of POD curves using a noise threshold of 2 and 3 voxels. The dashed lines represent the confidence bands for each set of POD curves.

The XCT raw data and the reconstruction of defects 1,2 and 3 from **Figure 34** in Chapter 4 is presented in **Figure S4**. A decrease in resolution resulted in only the bulkier regions of these defects to be detected. The pairwise distances between the bulky defect segments belonging to the same defect as informed by the ground truth, are also shown in the figures.

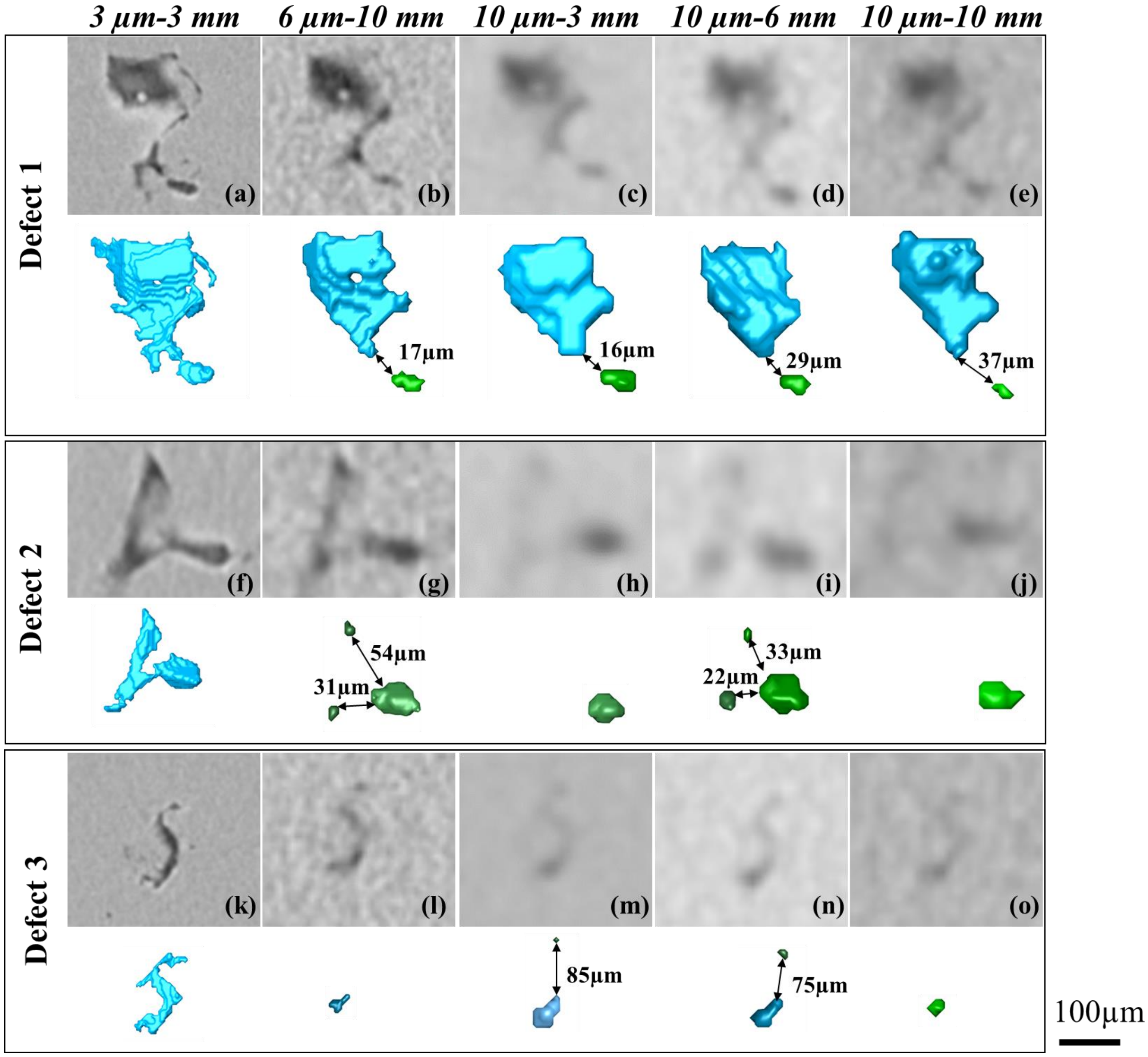

Figure S4. XCT slice images and 3D reconstruction of defects (a)-(e) 1, (f)-(j) 2 and (k)-(o)3. The distances shown are the minimum Euclidean distances between the detected cluster of entities belonging to the corresponding defect, as informed by the ground truth data.

8. References

[1] Gradl P, Tinker DC, Park A, Mireles OR, Garcia M, Wilkerson R, et al. Robust Metal Additive Manufacturing Process Selection and Development for Aerospace Components. Journal of Materials Engineering and Performance 2022 31:8 2022;31:6013–44. https://doi.org/10.1007/S11665-022-06850-0.

[2] Blakey-Milner B, Gradl P, Snedden G, Brooks M, Pitot J, Lopez E, et al. Metal additive manufacturing in aerospace: A review. Mater Des 2021;209:110008. https://doi.org/10.1016/j.matdes.2021.110008.

[3] Manfredi D, Bidulský R. Laser powder bed fusion of aluminum alloys. Acta Metallurgica Slovaca 2017;23:276–82. https://doi.org/10.12776/ams.v23i3.988.

[4] Mukherjee T, Elmer JW, Wei HL, Lienert TJ, Zhang W, Kou S, et al. Control of grain structure, phases, and defects in additive manufacturing of high-performance metallic components. Prog Mater Sci 2023;138:101153. https://doi.org/10.1016/J.PMATSCI.2023.101153.

[5] Torries B, Imandoust A, Beretta S, Shao S, Shamsaei N. Overview on Microstructure- and Defect-Sensitive Fatigue Modeling of Additively Manufactured Materials. Jom 2018;70:1853–62. https://doi.org/10.1007/s11837-018-2987-9.

[6] Mostafaei A, Zhao C, He Y, Reza Ghiaasiaan S, Shi B, Shao S, et al. Defects and anomalies in powder bed fusion metal additive manufacturing. Curr Opin Solid State Mater Sci 2022;26:100974. https://doi.org/10.1016/j.cossms.2021.100974.

[7] Murakami Y. Material defects as the basis of fatigue design. Int J Fatigue 2012;41:2–10. https://doi.org/10.1016/J.IJFATIGUE.2011.12.001.

[8] Ralph I. Stephens, Ali Fatemi, Robert R. Stephens HOF. Metal Fatigue in Engineering, 2nd Edition. Wiley; 2000.

[9] Li SS, Yue X, Li QY, Peng HL, Dong BX, Liu TS, et al. Development and applications of aluminum alloys for aerospace industry. Journal of Materials Research and Technology 2023;27:944–83. https://doi.org/10.1016/J.JMRT.2023.09.274.

[10] Aversa A, Marchese G, Saboori A, Bassini E, Manfredi D, Biamino S, et al. New aluminum alloys specifically designed for laser powder bed fusion: A review. Materials 2019;12. https://doi.org/10.3390/ma12071007.

[11] Nezhadfar PD, Thompson S, Saharan A, Phan N, Shamsaei N. Structural integrity of additively manufactured aluminum alloys: Effects of build orientation on microstructure, porosity, and fatigue behavior. Addit Manuf 2021;47:102292. https://doi.org/10.1016/j.addma.2021.102292.

[12] Ferro P, Fabrizi A, Berto F, Savio G, Meneghello R, Rosso S. Defects as a root cause of fatigue weakening of additively manufactured AlSi10Mg components. Theoretical and Applied Fracture Mechanics 2020;108:102611. https://doi.org/10.1016/J.TAFMEC.2020.102611.

[13] NASA. MSFC-SPEC-3717 - Specification for Control and Qualification of Laser Powder Bed Fusion Metallurgical Processes 2017:58. https://doi.org/MSFC-SPEC-3717.

[14] Cunningham R, Narra SP, Ozturk T, Beuth J, Rollett AD. Evaluating the Effect of Processing Parameters on Porosity in Electron Beam Melted Ti-6Al-4V via Synchrotron X-ray Microtomography. JOM 2016;68:765–71. https://doi.org/10.1007/s11837-015-1802-0.

[15] Mishurova T, Evsevleev S, Piault P, King A, Henry L, Bruno G. Understanding the hot isostatic pressing effectiveness of laser powder bed fusion Ti-6Al-4V by in-situ X-ray

imaging and diffraction experiments. Scientific Reports 2023 13:1 2023;13:1–11. https://doi.org/10.1038/s41598-023-45258-1.
[16] Li B, Shen Y, Hu W. Casting defects induced fatigue damage in aircraft frames of ZL205A aluminum alloy – A failure analysis. Mater Des 2011;32:2570–82. https://doi.org/10.1016/J.MATDES.2011.01.039.
[17] Wang QG, Apelian D, Lados DA. Fatigue behavior of A356-T6 aluminum cast alloys. Part I. Effect of casting defects. Journal of Light Metals 2001;1:73–84. https://doi.org/10.1016/S1471-5317(00)00008-0.
[18] Couper MJ, Neeson AE, Griffiths JR. CASTING DEFECTS AND THE FATIGUE BEHAVIOUR OF AN ALUMINIUM CASTING ALLOY. Fatigue Fract Eng Mater Struct 1990;13:213–27. https://doi.org/10.1111/J.1460-2695.1990.TB00594.X.
[19] Baig S, Ghiaasiaan R, Shao S, Shamsaei N. Tensile and fatigue behaviors of additively manufactured AlSi10Mg: Effect of solutionizing and aging heat treatments. Fatigue Fract Eng Mater Struct 2023;46:2662–80. https://doi.org/10.1111/FFE.14024.
[20] Rendigs KH. Aluminium Structures Used in Aerospace - Status and Prospects-. Materials Science Forum 1997;242:11–24. https://doi.org/10.4028/www.scientific.net/MSF.242.11.
[21] Zhang J, Song B, Wei Q, Bourell D, Shi Y. A review of selective laser melting of aluminum alloys: Processing, microstructure, property and developing trends. J Mater Sci Technol 2019;35:270–84. https://doi.org/10.1016/j.jmst.2018.09.004.
[22] Prathyusha ALR, Raghu Babu G. A review on additive manufacturing and topology optimization process for weight reduction studies in various industrial applications. Mater Today Proc 2022;62:109–17. https://doi.org/10.1016/j.matpr.2022.02.604.
[23] Yadollahi A, Shamsaei N. Additive manufacturing of fatigue resistant materials: Challenges and opportunities. Int J Fatigue 2017;98:14–31. https://doi.org/10.1016/j.ijfatigue.2017.01.001.
[24] Shamsaei N, Yadollahi A, Bian L, Thompson SM. An overview of Direct Laser Deposition for additive manufacturing; Part II: Mechanical behavior, process parameter optimization and control. Addit Manuf 2015;8:12–35. https://doi.org/10.1016/j.addma.2015.07.002.
[25] Mann V, Krokhin A, Alabin A, Zmanovskiy S, Konkevich V, Redkin I. Evolution of Aluminum Alloys Structure at Production Phases of 3D Products by Methods of Additive Technologies, 2017, p. 49–59. https://doi.org/10.1007/978-3-319-51493-2_6.
[26] Li J, Li Y, Wang Z, Li C, Yuan H, Hao Y. Effect of Microstructural Evolution on Mechanical Properties and Fracture Modes of AlSi10Mg Blocks Fabricated by Selective Laser Melting after Stress Relief Annealing. Adv Eng Mater 2022;24. https://doi.org/10.1002/adem.202200585.
[27] Garmendia X, Chalker S, Bilton M, Sutcliffe CJ, Chalker PR. Microstructure and mechanical properties of Cu-modified AlSi10Mg fabricated by Laser-Powder Bed Fusion. Materialia (Oxf) 2020;9:100590. https://doi.org/10.1016/j.mtla.2020.100590.
[28] Torries B, Sterling AJ, Shamsaei N, Thompson SM, Daniewicz SR. Utilization of a Microstructure Sensitive Fatigue Model for Additively Manufactured Ti-6Al-4V. Rapid Prototyping 2016;22:817–25.
[29] Hwang WJ, Bang GB, Choa SH. Effect of a Stress Relief Heat Treatment of AlSi7Mg and AlSi10Mg Alloys on Mechanical and Electrical Properties According to Silicon Precipitation. Metals and Materials International 2022. https://doi.org/10.1007/s12540-022-01304-7.

[30] Muhammad M, Nezhadfar PD, Thompson S, Saharan A, Phan N, Shamsaei N. A comparative investigation on the microstructure and mechanical properties of additively manufactured aluminum alloys. Int J Fatigue 2021;146:106165. https://doi.org/10.1016/j.ijfatigue.2021.106165.
[31] Romano S, Brückner-Foit A, Brandão A, Gumpinger J, Ghidini T, Beretta S. Fatigue properties of AlSi10Mg obtained by additive manufacturing: Defect-based modelling and prediction of fatigue strength. Eng Fract Mech 2018;187:165–89. https://doi.org/10.1016/j.engfracmech.2017.11.002.
[32] Brandl E, Heckenberger U, Holzinger V, Buchbinder D. Additive manufactured AlSi10Mg samples using Selective Laser Melting (SLM): Microstructure, high cycle fatigue, and fracture behavior. Mater Des 2012;34:159–69. https://doi.org/10.1016/j.matdes.2011.07.067.
[33] Uzan NE, Shneck R, Yeheskel O, Frage N. Fatigue of AlSi10Mg specimens fabricated by additive manufacturing selective laser melting (AM-SLM). Materials Science and Engineering: A 2017;704:229–37. https://doi.org/https://doi.org/10.1016/j.msea.2017.08.027.
[34] Domfang Ngnekou JN, Nadot Y, Henaff G, Nicolai J, Kan WH, Cairney JM, et al. Fatigue properties of AlSi10Mg produced by Additive Layer Manufacturing. Int J Fatigue 2019;119:160–72. https://doi.org/10.1016/j.ijfatigue.2018.09.029.
[35] Raja A, Cheethirala SR, Gupta P, Vasa NJ, Jayaganthan R. A review on the fatigue behaviour of AlSi10Mg alloy fabricated using laser powder bed fusion technique. Journal of Materials Research and Technology 2022;17:1013–29. https://doi.org/10.1016/j.jmrt.2022.01.028.
[36] Zhang C, Zhu H, Liao H, Cheng Y, Hu Z, Zeng X. Effect of heat treatments on fatigue property of selective laser melting AlSi10Mg. Int J Fatigue 2018;116:513–22. https://doi.org/10.1016/j.ijfatigue.2018.07.016.
[37] Carpenter Additive. Carpenter Additive n.d.
[38] ASTM E8. ASTM E8/E8M standard test methods for tension testing of metallic materials 1. Annual Book of ASTM Standards 4 2010:1–27. https://doi.org/10.1520/E0008.
[39] ASTM International. E606/E606M - 19e1: Standard Test Method for Strain-Controlled Fatigue Testing 2019. https://doi.org/10.1520/E0606_E0606M-19E01.
[40] Baig S, Ghiaasiaan SR, Shamsaei N. Effect of Heat Treatment on the Microstructure and Mechanical Properties of LB-PBF AlSi10Mg and Scalmalloy. Light Metals 2021 n.d.;4:119.
[41] ASTM. E3-11 Standard Guide for Preparation of Metallographic Specimens 1. ASTM Copyright 2011. https://doi.org/10.1520/E0003-11.2.
[42] Zaefferer S, Elhami N-N. Theory and application of electron channelling contrast imaging under controlled diffraction conditions. Acta Mater 2014;75:20–50. https://doi.org/10.1016/j.actamat.2014.04.018.
[43] ASTM. Standard Practice for Conducting Force Controlled Constant Amplitude Axial Fatigue Tests of Metallic Materials. Test 2002;03:4–8. https://doi.org/10.1520/E0466-21.2.
[44] Liu S, Shin YC. Additive manufacturing of Ti6Al4V alloy: A review. Mater Des 2019;164:107552.
[45] Qin H, Dong Q, Fallah V, Daymond MR. Rapid Solidification and Non-equilibrium Phase Constitution in Laser Powder Bed Fusion (LPBF) of AlSi10Mg Alloy: Analysis of Nano-

precipitates, Eutectic Phases, and Hardness Evolution. Metallurgical and Materials Transactions A 2020;51:448–66. https://doi.org/10.1007/s11661-019-05505-5.
[46] Takata N, Kodaira H, Sekizawa K, Suzuki A, Kobashi M. Change in microstructure of selectively laser melted AlSi10Mg alloy with heat treatments. Materials Science and Engineering A 2017;704:218–28. https://doi.org/10.1016/j.msea.2017.08.029.
[47] Bagherifard S, Beretta N, Monti S, Riccio M, Bandini M, Guagliano M. On the fatigue strength enhancement of additive manufactured AlSi10Mg parts by mechanical and thermal post-processing. Mater Des 2018;145:28–41. https://doi.org/10.1016/j.matdes.2018.02.055.
[48] Maamoun AH, Elbestawi M, Dosbaeva GK, Veldhuis SC. Thermal post-processing of AlSi10Mg parts produced by Selective Laser Melting using recycled powder. Addit Manuf 2018;21:234–47. https://doi.org/10.1016/j.addma.2018.03.014.
[49] Li W, Li S, Liu J, Zhang A, Zhou Y, Wei Q, et al. Effect of heat treatment on AlSi10Mg alloy fabricated by selective laser melting: Microstructure evolution, mechanical properties and fracture mechanism. Materials Science and Engineering A 2016;663:116–25. https://doi.org/10.1016/j.msea.2016.03.088.
[50] Porter DA, Easterling KE. Phase Transformations in Metals and Alloys. 1992. https://doi.org/10.1007/978-1-4899-3051-4.
[51] Zhou L, Mehta A, Schulz E, McWilliams B, Cho K, Sohn Y. Microstructure, precipitates and hardness of selectively laser melted AlSi10Mg alloy before and after heat treatment. Mater Charact 2018;143:5–17. https://doi.org/10.1016/j.matchar.2018.04.022.
[52] International A. ASTM E2627: Standard Practice for Determining Average Grain Size Using Electron Backscatter Diffraction (EBSD) in Fully Recrystallized Polycrystalline Materials n.d.
[53] Thijs L, Kempen K, Kruth JP, Van Humbeeck J. Fine-structured aluminium products with controllable texture by selective laser melting of pre-alloyed AlSi10Mg powder. Acta Mater 2013;61:1809–19. https://doi.org/10.1016/j.actamat.2012.11.052.
[54] Kimura T, Nakamoto T. Microstructures and mechanical properties of A356 (AlSi7Mg0.3) aluminum alloy fabricated by selective laser melting. Mater Des 2016;89:1294–301. https://doi.org/10.1016/j.matdes.2015.10.065.
[55] Aboulkhair NT, Maskery I, Tuck C, Ashcroft I, Everitt NM. The microstructure and mechanical properties of selectively laser melted AlSi10Mg: The effect of a conventional T6-like heat treatment. Materials Science and Engineering A 2016;667:139–46. https://doi.org/10.1016/j.msea.2016.04.092.
[56] Yadollahi A, Shamsaei N, Thompson SM, Seely DW. Effects of process time interval and heat treatment on the mechanical and microstructural properties of direct laser deposited 316L stainless steel. Materials Science and Engineering A 2015;644:171–83. https://doi.org/10.1016/j.msea.2015.07.056.
[57] Prashanth KG, Scudino S, Klauss HJ, Surreddi KB, Löber L, Wang Z, et al. Microstructure and mechanical properties of Al–12Si produced by selective laser melting: Effect of heat treatment. Materials Science and Engineering: A 2014;590:153–60. https://doi.org/10.1016/j.msea.2013.10.023.
[58] Ma P, Prashanth K, Scudino S, Jia Y, Wang H, Zou C, et al. Influence of Annealing on Mechanical Properties of Al-20Si Processed by Selective Laser Melting. Metals (Basel) 2014;4:28–36. https://doi.org/10.3390/met4010028.

[59] Liu Z, Cheng N, Zheng Q, Wu J, Han Q, Huang Z, et al. Processing and tensile properties of A356 composites containing in situ small-sized Al3Ti particulates. Materials Science and Engineering: A 2018;710:392–9. https://doi.org/10.1016/j.msea.2017.11.005.

[60] Uddin SZ, Murr LE, Terrazas CA, Morton P, Roberson DA, Wicker RB. Processing and characterization of crack-free aluminum 6061 using high-temperature heating in laser powder bed fusion additive manufacturing. Addit Manuf 2018;22:405–15. https://doi.org/10.1016/j.addma.2018.05.047.

[61] ASM International. ASM Handbook Volume 2: Properties and Selection: Nonferrous Alloys and Special-Purpose Materials. ASM International; 1990.

[62] Ghiaasiaan R, Shankar S. Structure-property models in Al-Zn-Mg-Cu alloys: A critical experimental assessment of shape castings. Materials Science and Engineering: A 2018;733:235–45.

[63] Murakami Y, Endo M. Effects of defects, inclusions and inhomogeneities on fatigue strength. Int J Fatigue 1994;16:163–82. https://doi.org/10.1016/0142-1123(94)90001-9.

[64] Wu J, Wang XQ, Wang W, Attallah MM, Loretto MH. Microstructure and strength of selectively laser melted AlSi10Mg. Acta Mater 2016;117:311–20. https://doi.org/10.1016/j.actamat.2016.07.012.

[65] Fousová M, Dvorský D, Michalcová A, Vojtěch D. Changes in the microstructure and mechanical properties of additively manufactured AlSi10Mg alloy after exposure to elevated temperatures. Mater Charact 2018;137:119–26. https://doi.org/10.1016/j.matchar.2018.01.028.

[66] Larráyoz Izcara X, Guirao Blank A, Pyczak F, Staron P, Schumann S, Huber N. Characterization and modeling of the influence of artificial aging on the microstructural evolution of age-hardenable AlSi10Mg(Cu) aluminum alloys. Materials Science and Engineering A 2014;610:46–53. https://doi.org/10.1016/j.msea.2014.04.031.

[67] Hadadzadeh A, Amirkhiz BS, Mohammadi M. Contribution of Mg2Si precipitates to the strength of direct metal laser sintered AlSi10Mg. Materials Science and Engineering A 2019;739:295–300. https://doi.org/10.1016/j.msea.2018.10.055.

[68] Ahn SY, Moon J, Choi YT, Kim ES, Jeong SG, Park JM, et al. A precipitation-hardened AlSi10Mg alloy fabricated using selective laser melting. Materials Science and Engineering A 2022;844:143164. https://doi.org/10.1016/j.msea.2022.143164.

[69] Ian Polmear. Light Alloys: From Traditional Alloys to Nanocrystals, Fourth Edition. Fourth Edi. Butterworth-Heinemann is an imprint of Elsevier; 2006.

[70] Ghiaasiaan R, Shankar S. Microstructure, Intermetallic Phases, and Fractography of the Cast Al-5.8Zn-2.2Mg-2.5Cu Alloy by Controlled Diffusion Solidification. Metall Mater Trans A Phys Metall Mater Sci 2020;51:4711–26. https://doi.org/10.1007/s11661-020-05885-z.

[71] Poudel A, Yasin MS, Ye J, Liu J, Vinel A, Shao S, et al. Feature-based volumetric defect classification in metal additive manufacturing. Nat Commun 2022;13:1–12. https://doi.org/10.1038/s41467-022-34122-x.

[72] Iturrioz A, Gil E, Petite MM, Garciandia F, Mancisidor AM, San Sebastian M. Selective laser melting of AlSi10Mg alloy: influence of heat treatment condition on mechanical properties and microstructure. Welding in the World 2018;62:885–92. https://doi.org/10.1007/s40194-018-0592-8.

[73] Cai C, Geng H, Cui Q, Wang S, Zhang Z. Low cycle fatigue behavior of AlSi10Mg(Cu) alloy at high temperature. Mater Charact 2018;145:594–605. https://doi.org/10.1016/j.matchar.2018.09.023.

[74] Bao J, Wu Z, Wu S, Withers PJ, Li F, Ahmed S, et al. Hot dwell-fatigue behaviour of additively manufactured AlSi10Mg alloy: Relaxation, cyclic softening and fracture mechanisms. Int J Fatigue 2021;151:106408. https://doi.org/10.1016/j.ijfatigue.2021.106408.

[75] Dodaran MS, Muhammad M, Shamsaei N, Shao S. Synergistic effect of microstructure and defects on the initiation of fatigue cracks in additively manufactured Inconel 718. Int J Fatigue 2022;162:107002. https://doi.org/10.1016/j.ijfatigue.2022.107002.

[76] du Plessis A, Beretta S. Killer notches: The effect of as-built surface roughness on fatigue failure in AlSi10Mg produced by laser powder bed fusion. Addit Manuf 2020;35:101424. https://doi.org/10.1016/j.addma.2020.101424.

[77] Beretta S, Gargourimotlagh M, Foletti S, du Plessis A, Riccio M. Fatigue strength assessment of “as built” AlSi10Mg manufactured by SLM with different build orientations. Int J Fatigue 2020;139:105737. https://doi.org/10.1016/j.ijfatigue.2020.105737.

[78] Li A, Baig S, Liu J, Shao S, Shamsaei N. Defect criticality analysis on fatigue life of L-PBF 17-4 PH stainless steel via machine learning. Int J Fatigue 2022;163:107018. https://doi.org/10.1016/j.ijfatigue.2022.107018.

[79] Starke EA, Staley JT. Application of modern aluminium alloys to aircraft. Fundamentals of Aluminium Metallurgy: Production, Processing and Applications 2011:747–83. https://doi.org/10.1533/9780857090256.3.747.

[80] Yadollahi A, Shamsaei N. Additive manufacturing of fatigue resistant materials: Challenges and opportunities. Int J Fatigue 2017;98:14–31. https://doi.org/10.1016/j.ijfatigue.2017.01.001.

[81] Read N, Wang W, Essa K, Attallah MM. Selective laser melting of AlSi10Mg alloy: Process optimisation and mechanical properties development. Mater Des 2015. https://doi.org/10.1016/j.matdes.2014.09.044.

[82] Gite RE, Wakchaure VD. A review on process parameters, microstructure and mechanical properties of additively manufactured AlSi10Mg alloy. Mater Today Proc 2023;72:966–86. https://doi.org/10.1016/J.MATPR.2022.09.100.

[83] Siyambaş Y, Turgut Y. Experimental investigation and optimization of the effects of manufacturing parameters on geometric tolerances in additive manufacturing of AlSi10Mg alloy. International Journal of Advanced Manufacturing Technology 2024;134:415–29. https://doi.org/10.1007/S00170-024-14128-Z/TABLES/6.

[84] Begoc S, Montredon F, Pommatau G, Leger G, Gas M. Additive manufacturing of Scalmalloy ® satellite parts. 8Th European Conference for Aeronautics and Space Sciences (Eucass) 2019:1–15. https://doi.org/10.13009/EUCASS2019-677.

[85] Baig S, Ghiaasiaan SR, Shamsaei N. Effect of Heat Treatment on the Microstructure and Mechanical Properties of LB-PBF AlSi10Mg and Scalmalloy. Light Metals 2021 n.d.;4:119.

[86] Brandão AD, Gumpinger J, Gschweitl M, Seyfert C, Hofbauer P, Ghidini T. Fatigue Properties of Additively Manufactured AlSi10Mg-Surface Treatment Effect. Procedia Structural Integrity 2017;7:58–66. https://doi.org/10.1016/j.prostr.2017.11.061.

[87] Wu J, Wang XQ, Wang W, Attallah MM, Loretto MH. Microstructure and strength of selectively laser melted AlSi10Mg. Acta Mater 2016;117:311–20. https://doi.org/10.1016/j.actamat.2016.07.012.
[88] Brandl E, Heckenberger U, Holzinger V, Buchbinder D. Additive manufactured AlSi10Mg samples using Selective Laser Melting (SLM): Microstructure, high cycle fatigue, and fracture behavior. Mater Des 2012;34:159–69. https://doi.org/10.1016/j.matdes.2011.07.067.
[89] Romano S, Brückner-Foit A, Brandão A, Gumpinger J, Ghidini T, Beretta S. Fatigue properties of AlSi10Mg obtained by additive manufacturing: Defect-based modelling and prediction of fatigue strength. Eng Fract Mech 2018;187:165–89. https://doi.org/10.1016/j.engfracmech.2017.11.002.
[90] Domfang Ngnekou JN, Nadot Y, Henaff G, Nicolai J, Kan WH, Cairney JM, et al. Fatigue properties of AlSi10Mg produced by Additive Layer Manufacturing. Int J Fatigue 2019;119:160–72. https://doi.org/10.1016/J.IJFATIGUE.2018.09.029.
[91] Turnbull A, De Los Rios ER. THE EFFECT OF GRAIN SIZE ON FATIGUE CRACK GROWTH IN AN ALUMINIUM MAGNESIUM ALLOY. Fatigue Fract Eng Mater Struct 1995;18:1355–66. https://doi.org/10.1111/J.1460-2695.1995.TB00861.X.
[92] Murakami Y. Metal Fatigue: Effects of Small Defects and Nonmetallic Inclusions. vol. 47. Elsevier; 2002. https://doi.org/10.1515/ijmr-1962-530203.
[93] Chan KS. Roles of microstructure in fatigue crack initiation. Int J Fatigue 2010;32:1428–47. https://doi.org/10.1016/J.IJFATIGUE.2009.10.005.
[94] Gray GT, Williams JC, Thompson AW. Roughness-Induced Crack Closure: An Explanation for Microstructurally Sensitive Fatigue Crack Growth. Metallurgical Transactions A 1983;14:421–33. https://doi.org/10.1007/BF02644220/METRICS.
[95] Macallister N, Becker TH. Fatigue life estimation of additively manufactured Ti-6Al-4V: Sensitivity, scatter and defect description in Damage-tolerant models. Acta Mater 2022;237:118189. https://doi.org/10.1016/J.ACTAMAT.2022.118189.
[96] Beretta S, Romano S. A comparison of fatigue strength sensitivity to defects for materials manufactured by AM or traditional processes. Int J Fatigue 2017. https://doi.org/10.1016/j.ijfatigue.2016.06.020.
[97] Yadollahi Aref, Shamsaei N, Thompson SM, Elwany A, Bian L. Effects of building orientation and heat treatment on fatigue behavior of selective laser melted 17-4 PH stainless steel. Int J Fatigue 2017;94:218–35. https://doi.org/10.1016/j.ijfatigue.2016.03.014.
[98] Peng X, Wu S, Qian W, Bao J, Hu Y, Zhan Z, et al. The potency of defects on fatigue of additively manufactured metals. Int J Mech Sci 2022;221:107185. https://doi.org/10.1016/J.IJMECSCI.2022.107185.
[99] Romano S, Beretta S, Brandão A, Gumpinger J, Ghidini T. HCF resistance of AlSi10Mg produced by SLM in relation to the presence of defects. Procedia Structural Integrity 2017;7:101–8. https://doi.org/10.1016/j.prostr.2017.11.066.
[100] Wu Z, Wu S, Gao X, Lin Y, Xue Y, Withers PJ. The role of internal defects on anisotropic tensile failure of L-PBF AlSi10Mg alloys. Scientific Reports 2023 13:1 2023;13:1–8. https://doi.org/10.1038/s41598-023-39948-z.
[101] Martin AA, Calta NP, Khairallah SA, Wang J, Depond PJ, Fong AY, et al. Dynamics of pore formation during laser powder bed fusion additive manufacturing. Nature Communications 2019 10:1 2019;10:1–10. https://doi.org/10.1038/s41467-019-10009-2.

[102] Du C, Zhao Y, Jiang J, Wang Q, Wang H, Li N, et al. Pore defects in Laser Powder Bed Fusion: Formation mechanism, control method, and perspectives. J Alloys Compd 2023;944:169215. https://doi.org/10.1016/J.JALLCOM.2023.169215.

[103] ASTM. ASTM F3301-Standard for Additive Manufacturing – Post Processing Methods – Standard Specification for Thermal Post-Processing Metal Parts Made Via Powder Bed Fusion. ASTM Standards 2018:3. https://doi.org/10.1520/F3301-18A.2.

[104] Schimbäck D, Mair P, Kaserer L, Perfler L, Palm F, Leichtfried G, et al. An improved process scan strategy to obtain high-performance fatigue properties for Scalmalloy®. Mater Des 2022;224:111410. https://doi.org/10.1016/J.MATDES.2022.111410.

[105] Awd M, Tenkamp J, Hirtler M, Siddique S, Bambach M, Walther F. Comparison of microstructure and mechanical properties of Scalmalloy® produced by selective laser melting and laser metal deposition. Materials 2017;11. https://doi.org/10.3390/ma11010017.

[106] Schimbäck D, Kaserer L, Mair P, Palm F, Leichtfried G, Pogatscher S, et al. Deformation and fatigue behaviour of additively manufactured Scalmalloy® with bimodal microstructure. Int J Fatigue 2023;172:107592. https://doi.org/10.1016/J.IJFATIGUE.2023.107592.

[107] Beretta S. More than 25 years of extreme value statistics for defects: Fundamentals, historical developments, recent applications. Int J Fatigue 2021;151:106407. https://doi.org/10.1016/J.IJFATIGUE.2021.106407.

[108] Beretta S, Murakami Y. Statistical analysis of defects for fatigue strength prediction and quality control of materials. Fatigue Fract Eng Mater Struct 1998;21:1049–65. https://doi.org/10.1046/J.1460-2695.1998.00104.X.

[109] Murakami Y, Takagi T, Wada K, Matsunaga H. Essential structure of S-N curve: Prediction of fatigue life and fatigue limit of defective materials and nature of scatter. Int J Fatigue 2021;146:106138. https://doi.org/10.1016/J.IJFATIGUE.2020.106138.

[110] Beretta S, Patriarca L, Gargourimotlagh M, Hardaker A, Brackett D, Salimian M, et al. A benchmark activity on the fatigue life assessment of AlSi10Mg components manufactured by L-PBF. Mater Des 2022;218:110713. https://doi.org/10.1016/J.MATDES.2022.110713.

[111] Perghem D, Rusnati | Lorenzo, Luca Patriarca |, Uriati F, Beretta S. Comparison of Fatigue Life and Strength Models for Defective Materials: Application to Scalmalloy in Different Surface Conditions. Fatigue Fract Eng Mater Struct 2025. https://doi.org/10.1111/FFE.14638.

[112] Beretta S, Romano S. A comparison of fatigue strength sensitivity to defects for materials manufactured by AM or traditional processes. Int J Fatigue 2017;94:178–91. https://doi.org/10.1016/J.IJFATIGUE.2016.06.020.

[113] Benedetti M, Fontanari V, Bandini M, Zanini F, Carmignato S. Low-and high-cycle fatigue resistance of Ti-6Al-4V ELI additively manufactured via selective laser melting: Mean stress and defect sensitivity. Int J Fatigue 2018;107:96–109.

[114] Meyers MA, Chawla KK. Mechanical Behavior of Materials. 2nd ed. Cambridge University Press; 2008. https://doi.org/10.1017/CBO9780511810947.

[115] Dowling NE. Mechanical Behavior of Materials: Engineering Methods for Deformation, Fracture, and Fatigue. vol. 11. Fourth Edi. Pearson; 2013.

[116] Shao S, Poudel A, Shamsaei N. A linear elastic finite element approach to fatigue life estimation for defect laden materials. Eng Fract Mech 2023;285:109298. https://doi.org/10.1016/J.ENGFRACMECH.2023.109298.

[117] Miller KJ. THE TWO THRESHOLDS OF FATIGUE BEHAVIOUR. Fatigue Fract Eng Mater Struct 1993;16:931–9. https://doi.org/10.1111/J.1460-2695.1993.TB00129.X.
[118] Lei Z, Hong Y, Xie J, Sun C, Zhao A. Effects of inclusion size and location on very-high-cycle fatigue behavior for high strength steels. Materials Science and Engineering: A 2012;558:234–41. https://doi.org/10.1016/J.MSEA.2012.07.118.
[119] Sheridan L. A modified El-Haddad model for versatile defect tolerant design. Int J Fatigue 2021;145:106062. https://doi.org/10.1016/J.IJFATIGUE.2020.106062.
[120] Sausto F, Carrion PE, Shamsaei N, Beretta S. Fatigue failure mechanisms for AlSi10Mg manufactured by L-PBF under axial and torsional loads: The role of defects and residual stresses. Int J Fatigue 2022;162:106903. https://doi.org/10.1016/J.IJFATIGUE.2022.106903.
[121] Hrabe N, Gnäupel-Herold T, Quinn T. Fatigue properties of a titanium alloy (Ti–6Al–4V) fabricated via electron beam melting (EBM): Effects of internal defects and residual stress. Int J Fatigue 2017;94:202–10. https://doi.org/10.1016/J.IJFATIGUE.2016.04.022.
[122] Chernyshova P, Guraya T, Singamneni S, Zhu T, Chen ZW. Fatigue Crack Growth Behavior of Al-4.5Mg-0.6Sc-0.3Zr Alloy Processed by Laser Powder Bed Fusion. J Mater Eng Perform 2021;30:6743–51. https://doi.org/10.1007/S11665-021-05989-6/FIGURES/12.
[123] Bulloch JH. Fatigue threshold in steels—Mean stress and microstructure influences. International Journal of Pressure Vessels and Piping 1994;58:103–27. https://doi.org/10.1016/0308-0161(94)90013-2.
[124] Ritchie RO. Influence of microstructure on near-threshold fatigue-crack propagation in ultra-high strength steel. Metal Science 1977;11:368–81. https://doi.org/10.1179/MSC.1977.11.8-9.368.
[125] Sachs NW. Understanding the surface features of fatigue fractures: How they describe the failure cause and the failure history. Journal of Failure Analysis and Prevention 2005;5:11–5. https://doi.org/10.1361/15477020522924/METRICS.
[126] Venning L, Hogg SC, Sinclair I, Reed PAS. Fatigue crack growth and closure in fine-grained aluminium alloys. Materials Science and Engineering: A 2006;428:247–55. https://doi.org/10.1016/J.MSEA.2006.05.020.
[127] Vasudeven AK, Sadananda K, Louat N. A review of crack closure, fatigue crack threshold and related phenomena. Materials Science and Engineering: A 1994;188:1–22. https://doi.org/10.1016/0921-5093(94)90351-4.
[128] Furuya Y, Hirukawa H, Takeuchi E. Gigacycle fatigue in high strength steels. Sci Technol Adv Mater 2019;20:643. https://doi.org/10.1080/14686996.2019.1610904.
[129] Shiozawa K, Lu L. Internal Fatigue Failure Mechanism of High Strength Steels in Gigacycle Regime. Key Eng Mater 2008;378–379:65–80. https://doi.org/10.4028/WWW.SCIENTIFIC.NET/KEM.378-379.65.
[130] Shiozawa K, Murai M, Shimatani Y, Yoshimoto T. Transition of fatigue failure mode of Ni–Cr–Mo low-alloy steel in very high cycle regime. Int J Fatigue 2010;32:541–50. https://doi.org/10.1016/J.IJFATIGUE.2009.06.011.
[131] Jones R, Singh Raman RK, McMillan AJ. Crack growth: Does microstructure play a role? Eng Fract Mech 2018;187:190–210. https://doi.org/10.1016/J.ENGFRACMECH.2017.11.023.
[132] Tenkamp J, Stern F, Walther F. Uniform fatigue damage tolerance assessment for additively manufactured and cast Al-Si alloys: An elastic-plastic fracture mechanical approach.

Additive Manufacturing Letters 2022;3:100054. https://doi.org/10.1016/J.ADDLET.2022.100054.
[133] Minerva G, Awd M, Koch A, Walther F, Beretta S. Transferability of anomaly data to fatigue properties of PBF-LB AlSi10Mg parts with different volumes. Int J Fatigue 2025;195:108852. https://doi.org/10.1016/J.IJFATIGUE.2025.108852.
[134] Baig S, Jam A, Beretta S, Shao S, Shamsaei N. Non-destructive detection of critical defects in additive manufacturing. Scientific Reports 2025 15:1 2025;15:1–12. https://doi.org/10.1038/s41598-025-91608-6.
[135] Sanaei N, Fatemi A, Phan N. Defect characteristics and analysis of their variability in metal L-PBF additive manufacturing. Mater Des 2019;182:108091. https://doi.org/10.1016/J.MATDES.2019.108091.
[136] Ahmed F, Ali U, Sarker D, Marzbanrad E, Choi K, Mahmoodkhani Y, et al. Study of Powder Recycling and its Effect on Printed Parts During Laser Powder-Bed Fusion of 17-4 PH Stainless Steel. J Mater Process Technol 2019:127177. https://doi.org/10.1016/j.jmatprotec.2019.116522.
[137] Fatemi A, Molaei R, Simsiriwong J, Sanaei N, Pegues J, Torries B, et al. Fatigue behaviour of additive manufactured materials: An overview of some recent experimental studies on Ti-6Al-4V considering various processing and loading direction effects. Fatigue Fract Eng Mater Struct 2019;42:991–1009. https://doi.org/10.1111/FFE.13000.
[138] Stephens RI, Fatemi A, Stephens RR, Fuchs HO. Metal fatigue in engineering. John Wiley & Sons; 2000.
[139] Liu W, Chen C, Shuai S, Zhao R, Liu L, Wang X, et al. Study of pore defect and mechanical properties in selective laser melted Ti6Al4V alloy based on X-ray computed tomography. Materials Science and Engineering: A 2020;797:139981. https://doi.org/10.1016/J.MSEA.2020.139981.
[140] Zhang K, Chen Y, Marussi S, Fan X, Fitzpatrick M, Bhagavath S, et al. Pore evolution mechanisms during directed energy deposition additive manufacturing. Nature Communications 2024 15:1 2024;15:1–14. https://doi.org/10.1038/s41467-024-45913-9.
[141] Sheridan L, Scott-Emuakpor OE, George T, Gockel JE. Relating porosity to fatigue failure in additively manufactured alloy 718. Materials Science and Engineering: A 2018;727:170–6. https://doi.org/10.1016/j.msea.2018.04.075.
[142] Withers PJ. X-ray nanotomography. Materials Today 2007;10:26–34. https://doi.org/10.1016/S1369-7021(07)70305-X.
[143] du Plessis A, Yadroitsava I, Yadroitsev I. Effects of defects on mechanical properties in metal additive manufacturing: A review focusing on X-ray tomography insights. Mater Des 2020;187:108385. https://doi.org/10.1016/J.MATDES.2019.108385.
[144] Thompson A, Senin N, Maskery I, Leach R. Effects of magnification and sampling resolution in X-ray computed tomography for the measurement of additively manufactured metal surfaces. Precis Eng 2018;53:54–64. https://doi.org/10.1016/J.PRECISIONENG.2018.02.014.
[145] du Plessis A, Tshibalanganda M, le Roux SG. Not all scans are equal: X-ray tomography image quality evaluation. Mater Today Commun 2020;22:100792. https://doi.org/10.1016/J.MTCOMM.2019.100792.
[146] Kim FH, Pintar AL, Moylan SP, Garboczi EJ. The influence of X-Ray computed tomography acquisition parameters on image quality and probability of detection of additive

manufacturing defects. Journal of Manufacturing Science and Engineering, Transactions of the ASME 2019;141. https://doi.org/10.1115/1.4044515/958429.

[147] Kastner J, Harrer B, Requena G, Brunke O. A comparative study of high resolution cone beam X-ray tomography and synchrotron tomography applied to Fe- and Al-alloys. NDT & E International 2010;43:599–605. https://doi.org/10.1016/J.NDTEINT.2010.06.004.

[148] Cunningham R, Zhao C, Parab N, Kantzos C, Pauza J, Fezzaa K, et al. Keyhole threshold and morphology in laser melting revealed by ultrahigh-speed x-ray imaging. Science (1979) 2019;363:849–52. https://doi.org/10.1126/SCIENCE.AAV4687/SUPPL_FILE/AAV4687S9.MOV.

[149] Department of Defense. MIL-HDBK-1823A: Nondestructive evaluation system reliability assessment. vol. 16. 2009. https://doi.org/10.1117/1.3659228.

[150] ASTM. E2862-Standard Practice for Probability of Detection Analysis for Hit / Miss Data 2012;i:1–6. https://doi.org/10.1520/E2862-18.2.

[151] ASTM. E3023-Standard Practice for Probability of Detection Analysis for â Versus a Data 2012:1–6. https://doi.org/10.1520/E3023-21.2.

[152] Yosifov M, Reiter M, Heupl S, Gusenbauer C, Fröhler B, Fernández- Gutiérrez R, et al. Probability of detection applied to X-ray inspection using numerical simulations. Nondestructive Testing and Evaluation 2022;37:536–51. https://doi.org/10.1080/10589759.2022.2071892.

[153] Kim FH, Pintar A, Obaton AF, Fox J, Tarr J, Donmez A. Merging experiments and computer simulations in X-ray Computed Tomography probability of detection analysis of additive manufacturing flaws. NDT & E International 2021;119:102416. https://doi.org/10.1016/J.NDTEINT.2021.102416.

[154] Hu YN, Wu SC, Withers PJ, Zhang J, Bao HYX, Fu YN, et al. The effect of manufacturing defects on the fatigue life of selective laser melted Ti-6Al-4V structures. Mater Des 2020;192:108708. https://doi.org/10.1016/J.MATDES.2020.108708.

[155] Gordon J V., Narra SP, Cunningham RW, Liu H, Chen H, Suter RM, et al. Defect structure process maps for laser powder bed fusion additive manufacturing. Addit Manuf 2020;36:101552. https://doi.org/10.1016/J.ADDMA.2020.101552.

[156] Kasperovich G, Haubrich J, Gussone J, Requena G. Correlation between porosity and processing parameters in TiAl6V4 produced by selective laser melting. Mater Des 2016;105:160–70. https://doi.org/10.1016/j.matdes.2016.05.070.

[157] Brennan MC, Keist JS, Palmer TA. Defects in Metal Additive Manufacturing Processes. Journal of Materials Engineering and Performance 2021 30:7 2021;30:4808–18. https://doi.org/10.1007/S11665-021-05919-6.

[158] Sundar V, Snow Z, Keist J, Jones G, Reed R, Reutzel E. Flaw Identification in Additively Manufactured Parts Using X-ray Computed Tomography and Destructive Serial Sectioning. J Mater Eng Perform 2021;30:4958–64. https://doi.org/10.1007/S11665-021-05567-W/FIGURES/5.

[159] Kerckhofs G, Pyka G, Moesen M, Van Bael S, Schrooten J, Wevers M. High-Resolution Microfocus X-Ray Computed Tomography for 3D Surface Roughness Measurements of Additive Manufactured Porous Materials. Adv Eng Mater 2013;15:153–8. https://doi.org/10.1002/ADEM.201200156.

[160] Rodríguez-Sánchez Á, Thompson A, Körner L, Brierley N, Leach R. Review of the influence of noise in X-ray computed tomography measurement uncertainty. Precis Eng 2020;66:382–91. https://doi.org/10.1016/J.PRECISIONENG.2020.08.004.

[161] Akgun E, Zhang X, Lowe T, Zhang Y, Doré M. Fatigue of laser powder-bed fusion additive manufactured Ti-6Al-4V in presence of process-induced porosity defects. Eng Fract Mech 2022;259:108140. https://doi.org/10.1016/J.ENGFRACMECH.2021.108140.
[162] Zerbst U, Bruno G, Buffière JY, Wegener T, Niendorf T, Wu T, et al. Damage tolerant design of additively manufactured metallic components subjected to cyclic loading: State of the art and challenges. Prog Mater Sci 2021;121:100786. https://doi.org/10.1016/J.PMATSCI.2021.100786.
[163] Seifi M, Gorelik M, Waller J, Hrabe N, Shamsaei N, Daniewicz S, et al. Progress towards metal additive manufacturing standardization to support qualification and certification. Jom 2017;69:439–55.
[164] Niu X, Zhu SP, He JC, Liao D, Correia JAFO, Berto F, et al. Defect tolerant fatigue assessment of AM materials: Size effect and probabilistic prospects. Int J Fatigue 2022;160:106884. https://doi.org/10.1016/J.IJFATIGUE.2022.106884.
[165] NASA. NASA-STD-6030 ADDITIVE MANUFACTURING REQUIREMENTS FOR SPACEFLIGHT SYSTEMS 2021.
[166] Rhein RK, Shi Q, Tekalur SA, Jones JW, Carroll JW. Short-Crack Growth Behavior in Additively Manufactured AlSi10Mg Alloy. J Mater Eng Perform 2021;30:5392–8. https://doi.org/10.1007/S11665-021-05820-2/FIGURES/7.
[167] Di Giovanni MT, de Menezes JTO, Bolelli G, Cerri E, Castrodeza EM. Fatigue crack growth behavior of a selective laser melted AlSi10Mg. Eng Fract Mech 2019;217:106564. https://doi.org/10.1016/j.engfracmech.2019.106564.
[168] Gorelik M. Additive manufacturing in the context of structural integrity. Int J Fatigue 2017;94:168–77. https://doi.org/10.1016/J.IJFATIGUE.2016.07.005.
[169] Pegues JW, Shao S, Shamsaei N, Sanaei N, Fatemi A, Warner DH, et al. Fatigue of additive manufactured Ti-6Al-4V, Part I: The effects of powder feedstock, manufacturing, and post-process conditions on the resulting microstructure and defects. Int J Fatigue 2020;132:105358.
[170] Molaei R, Fatemi A, Sanaei N, Pegues J, Shamsaei N, Shao S, et al. Fatigue of additive manufactured Ti-6Al-4V, Part II: The relationship between microstructure, material cyclic properties, and component performance. Int J Fatigue 2020;132:105363.
[171] Huang Y, Fleming TG, Clark SJ, Marussi S, Fezzaa K, Thiyagalingam J, et al. Keyhole fluctuation and pore formation mechanisms during laser powder bed fusion additive manufacturing. Nature Communications 2022 13:1 2022;13:1–11. https://doi.org/10.1038/s41467-022-28694-x.
[172] Beygi Nasrabadi H, Klotz UE, Tiberto D, Vafaeenezhad H, Mishurova T, Skrotzki B. Effect of keyhole and lack-of-fusion pores on the anisotropic microstructure and mechanical properties of PBF-LB/M-produced CuCrZr alloy. Progress in Additive Manufacturing 2025:1–15. https://doi.org/10.1007/S40964-025-00972-2/FIGURES/7.
[173] Guo L, Liu H, Wang H, Wei Q, Xiao Y, Tang Z, et al. Identifying the keyhole stability and pore formation mechanisms in laser powder bed fusion additive manufacturing. J Mater Process Technol 2023;321:118153. https://doi.org/10.1016/J.JMATPROTEC.2023.118153.
[174] Parab ND, Xiong L, Guo Q, Guo Z, Kirk C, Nie Y, et al. Investigation of dynamic fracture behavior of additively manufactured Al-10Si-Mg using high-speed synchrotron X-ray imaging. Addit Manuf 2019;30. https://doi.org/10.1016/j.addma.2019.100878.

[175] Sun S, Miller JD, Choi YR, Turk S, Donnelly D, Liu Q. Detectability by X-ray micro computed tomography of fatigue initiating void defects in laser powder-bed additively manufactured Ti-6Al-4V coupons. Addit Manuf 2024;81:103986. https://doi.org/10.1016/J.ADDMA.2024.103986.
[176] Tang M, Pistorius PC. Fatigue life prediction for AlSi10Mg components produced by selective laser melting. Int J Fatigue 2019;125:479–90. https://doi.org/10.1016/j.ijfatigue.2019.04.015.
[177] Russell R, Wells D, Waller J, Poorganji B, Ott E, Nakagawa T, et al. Qualification and certification of metal additive manufactured hardware for aerospace applications. Additive Manufacturing for the Aerospace Industry 2019:33–66. https://doi.org/10.1016/B978-0-12-814062-8.00003-0.
[178] Wong VWH, Ferguson M, Law KH, Lee YTT, Witherell P. Segmentation of Additive Manufacturing Defects Using U-Net. J Comput Inf Sci Eng 2022;22. https://doi.org/10.1115/1.4053078/1128855.
[179] Rathore JS, King A, Le Bourdais F, Garandet J-P. In-depth analysis of CT resolution impact on porosity evaluation in laser powder bed fusion additive manufacturing. Tomography of Materials and Structures 2025;8:100065. https://doi.org/10.1016/J.TMATER.2025.100065.
[180] Khod S, Goswami M, Dvivedi A. Additive manufacturing processes protocol prediction by Artificial Intelligence using X-ray Computed Tomography data. Progress in Additive Manufacturing 2025:1–19. https://doi.org/10.1007/S40964-025-01000-Z/FIGURES/21.
[181] Jia Q, Rometsch P, Kürnsteiner P, Chao Q, Huang A, Weyland M, et al. Selective laser melting of a high strength Al[sbnd]Mn[sbnd]Sc alloy: Alloy design and strengthening mechanisms. Acta Mater 2019;171:108–18. https://doi.org/10.1016/j.actamat.2019.04.014.
[182] Masuo H, Tanaka Y, Morokoshi S, Yagura H, Uchida T, Yamamoto Y, et al. Influence of defects, surface roughness and HIP on the fatigue strength of Ti-6Al-4V manufactured by additive manufacturing. Int J Fatigue 2018;117:163–79. https://doi.org/10.1016/j.ijfatigue.2018.07.020.
[183] Otsu N. Threshold selection method from gray-level histograms. IEEE Trans Syst Man Cybern 1979;SMC-9:62–6. https://doi.org/10.1109/TSMC.1979.4310076.
[184] Tang M, Pistorius PC, Beuth JL. Prediction of lack-of-fusion porosity for powder bed fusion. Addit Manuf 2017;14:39–48. https://doi.org/https://doi.org/10.1016/j.addma.2016.12.001.
[185] Nicoletto G, Anzelotti G, Konečná R. X-ray computed tomography vs. metallography for pore sizing and fatigue of cast Al-alloys. Procedia Eng 2010;2:547–54. https://doi.org/10.1016/J.PROENG.2010.03.059.
[186] Nafar Dastgerdi J, Jaberi O, Remes H, Lehto P, Hosseini Toudeshky H, Kuva J. Fatigue damage process of additively manufactured 316 L steel using X-ray computed tomography imaging. Addit Manuf 2023;70:103559. https://doi.org/10.1016/J.ADDMA.2023.103559.
[187] Shirani M, Härkegrd G. Damage tolerant design of cast components based on defects detected by 3D X-ray computed tomography. Int J Fatigue 2012;41:188–98. https://doi.org/10.1016/J.IJFATIGUE.2011.09.011.
[188] Tammas-Williams S, Withers PJ, Todd I, Prangnell PB. The Influence of Porosity on Fatigue Crack Initiation in Additively Manufactured Titanium Components. Scientific Reports 2017 7:1 2017;7:1–13. https://doi.org/10.1038/s41598-017-06504-5.

[189] Oberreiter M, Horvath M, Stoschka M, Fladischer S. Effect of Surface Finishing State on Fatigue Strength of Cast Aluminium and Steel Alloys. Materials 2023, Vol 16, Page 4755 2023;16:4755. https://doi.org/10.3390/MA16134755.
[190] Tang D, He X, Wu B, Dang L, Xin H, Li Y. A fatigue life prediction approach for porosity defect-induced failures in directed energy deposited Ti-6Al-4V considering crack growth environment. Int J Fatigue 2024;184:108272. https://doi.org/10.1016/J.IJFATIGUE.2024.108272.
[191] Rotella A, Nadot Y, Piellard M, Augustin R, Fleuriot M. Influence of defect morphology and position on the fatigue limit of cast Al alloy: 3D characterization by X-ray microtomography of natural and artificial defects. Materials Science and Engineering: A 2020;785:139347. https://doi.org/10.1016/J.MSEA.2020.139347.
[192] Shiozawa K, Lu L, Ishihara S. S–N curve characteristics and subsurface crack initiation behaviour in ultra-long life fatigue of a high carbon-chromium bearing steel. Fatigue Fract Eng Mater Struct 2001;24:781–90. https://doi.org/10.1046/J.1460-2695.2001.00459.X.